

¹ SEARCH FOR $t\bar{t}Z' \rightarrow t\bar{t}t\bar{t}$ PRODUCTION IN THE MULTILEPTON FINAL STATE IN
² pp COLLISIONS AT $\sqrt{s} = 13$ TEV WITH THE ATLAS DETECTOR

³ By

⁴ Hieu Le

⁵ A DISSERTATION

⁶ Submitted to
⁷ Michigan State University
⁸ in partial fulfillment of the requirements
⁹ for the degree of

¹⁰ Physics — Doctor of Philosophy

¹¹ 2025

ABSTRACT

This dissertation presents a search for a beyond-the-Standard-Model (BSM) top-philic heavy vector resonance based on a simplified top-philic color-singlet $Z'(\rightarrow t\bar{t})$ produced in association with a top-quark pair ($t\bar{t}Z'$), probing a Z' mass range from 1 TeV to 3 TeV. The analysis targets the same-sign dilepton and multilepton final states of four-top-quark ($t\bar{t}t\bar{t}$) events and is highly motivated by the recent observation of excess in Standard Model (SM) $t\bar{t}t\bar{t}$ production; the targeted search channels are sensitive to the $t\bar{t}Z'$ signal due to the distinctive $t\bar{t}t\bar{t}$ signal signature with high jet multiplicity and the suppression of common SM background processes. The search is performed using the full Run 2 data set collected by the ATLAS detector at the Large Hadron Collider between 2015 and 2018, corresponding to an integrated luminosity of 140 fb^{-1} of proton-proton collisions at a center-of-mass energy of $\sqrt{s} = 13 \text{ TeV}$. Data-driven techniques for $t\bar{t}W$ and charge misidentification background estimation are incorporated to improve background modeling at high jet multiplicity. No statistically significant deviation from SM predictions is observed. Observed exclusion limits at 95% confidence level are set on the production cross section of $pp \rightarrow t\bar{t}Z'$ multiplied by the branching ratio of $Z' \rightarrow t\bar{t}$ and range from 7.9 fb to 9.4 fb depending on the Z' mass.

ACKNOWLEDGMENTS

- ²⁹ Advisor: Reinhard Schwienhorst
- ³⁰ Postdoc: Binbin Dong
- ³¹ Committee
- ³² MSU group
- ³³ ATLAS analysis group
- ³⁴ Friend: Daniel, Grayson, Bella, Eric, Jordan
- ³⁵ Other friends: Jasper, Adam, Brittany
- ³⁶ Parents
- ³⁷ Spouse: Allen Sechrist
- ³⁸ ATLAS in general & funding agencies

PREFACE

40 This is my preface. remarks remarks remarks

TABLE OF CONTENTS

41	List of Tables	vii
42	List of Figures	ix
43	KEY TO ABBREVIATIONS	xi
44	Chapter 1. Introduction	1
45	Chapter 2. Theoretical Overview	5
46	2.1 The Standard Model	5
47	2.1.1 Elementary particles	5
48	2.1.2 Mathematical formalism	9
49	2.1.2.1 Quantum chromodynamics	10
50	2.1.2.2 Electroweak theory	11
51	2.1.2.3 Higgs mechanism	14
52	2.2 Beyond the Standard Model: $t\bar{t}Z' \rightarrow t\bar{t}t\bar{t}$	17
53	2.2.1 Top-philic vector resonance	17
54	2.2.2 Production channels	19
55	2.2.3 Decay modes	20
56	Chapter 3. LHC & ATLAS Experiment	21
57	3.1 The Large Hadron Collider	21
58	3.1.1 Overview	21
59	3.1.2 LHC operations	23
60	3.1.3 Physics at the LHC	24
61	3.2 The ATLAS detector	24
62	3.2.1 Inner detector	27
63	3.2.2 Calorimeter systems	28
64	3.2.3 Muon spectrometer	30
65	3.2.4 Trigger & data acquisition	32
66	Chapter 4. Particle Reconstruction & Identification	33
67	4.1 Primary reconstruction	33
68	4.1.1 Tracks	33
69	4.1.2 Vertices	34
70	4.1.3 Topological clusters	35
71	4.2 Jets	36
72	4.2.1 Jet reconstruction	37
73	4.2.2 Flavor tagging	38
74	4.3 Leptons	42
75	4.3.1 Electrons	42
76	4.3.2 Muons	45

77	4.4	Missing transverse momentum	47
78	4.5	Overlap removal	48
79	4.6	Object definition	49
80	Chapter 5. Data & Simulated Samples	50
81	5.1	Data samples	50
82	5.2	Monte Carlo samples	50
83	5.2.1	$t\bar{t}Z'$ signal samples	51
84	5.2.2	Background samples	53
85	Chapter 6. Analysis Strategy	55
86	6.1	Event selection	55
87	6.1.1	Event categorization	56
88	6.2	Analysis regions	57
89	6.2.1	Signal regions	59
90	6.2.2	Control regions	61
91	6.3	Background estimation	63
92	6.3.1	Template fitting for fake/non-prompt estimation	64
93	6.3.2	Charge misidentification data-driven estimation	64
94	6.3.3	$t\bar{t}W$ background data-driven estimation	67
95	Chapter 7. Systematic Uncertainties	69
96	7.1	Experimental uncertainties	69
97	7.1.1	Luminosity & pile-up reweighting	69
98	7.1.2	Leptons	69
99	7.1.3	Jets	71
100	7.1.4	Missing transverse energy	73
101	7.2	Modeling uncertainties	74
102	7.2.1	Signal and irreducible background uncertainties	74
103	7.2.2	Reducible background uncertainties	76
104	Chapter 8. Results	78
105	8.1	Statistical interpretation	78
106	8.1.1	Profile likelihood fit	78
107	8.1.2	Exclusion limit	81
108	8.2	Fit results	82
109	Chapter 9. Summary	88
110	References	89

List of Tables

111	Table 4.1: Overlap removal process for this analysis, applied sequentially from top to bottom.	48
114	Table 4.2: Summary of object selection criteria used in this analysis. ℓ_0 refers to the leading lepton in the event.	49
116	Table 5.1: Summary of all HLT triggers used in this analysis. Events are required to pass at least one trigger.	51
118	Table 5.2: Summary of all Monte-Carlo samples used in this analysis. V refers to an EW ($W^\pm/Z/\gamma^*$) or Higgs boson. Matrix element (ME) order refers to the order in QCD of the perturbative calculation. Tune refers to the underlying-event tune of the parton shower (PS) generator.	52
122	Table 6.1: Definitions of signal, control and validation regions (VR) used in this analysis. N_{jets} and N_b refers to the number of jets and number of b -tagged jets respectively. ℓ_1 refers to the leading lepton, ℓ_2 refers to the subleading lepton and so on. H_T refers to the p_T scalar sum of all leptons and jets in the event. $m_{\ell\ell}$ refers to the dilepton invariant mass, which must not coincide with the Z -boson mass range of 81-101 GeV for SS2L+3L events.	58
128	Table 6.2: Definitions of SR sub-regions. Events are sorted into different sub-regions based on the number of b -tagged jets and leptons present.	59
130	Table 6.3: List of possible assigned values for DFCAA.	62
131	Table 7.1: Summary of the experimental systematic uncertainties considered in this analysis.	70
133	Table 8.1: Normalization factors for backgrounds with dedicated CRs, obtained from a simultaneous fit in all CRs and SR under the background-only hypothesis. The nominal pre-fit value is 1 for all NFs and 0 for the scaling factors a_0 and a_1 . Uncertainties shown include both statistical and systematic uncertainties.	84

¹⁵⁰ List of Figures

¹⁵¹ Figure 2.1: Particles within the SM and their properties.	6
¹⁵² Figure 2.2: Feynman diagram for $t\bar{t}$ production and subsequent decay processes. Top quark decays into a W -boson and b -quarks, and W -boson can decay to a $q\bar{q}$ or a $\ell\nu_\ell$ pair.	¹⁵⁴ 8
¹⁵⁵ Figure 2.3: Illustration of a common representation of the Higgs potential. Before SSB, the ground state $\phi(0)$ is located at A which is symmetric with respect to the potential. A perturbation to this state fixes the ground state energy $ \phi(0) ^2$ to a particular value at B, "spontaneously" breaking the symmetry and degeneracy in $ \phi(0) ^2$	¹⁵⁹ 15
¹⁶⁰ Figure 2.4: Feynman diagrams for tree level Z' production in association with (a) $t\bar{t}$, (b) tj (light quark) and (c) tW , decaying to final states containing (a) $t\bar{t}t\bar{t}$ or (b)(c) $t\bar{t}t$	¹⁶² 19
¹⁶³ Figure 2.5: Branching ratios for $t\bar{t}t\bar{t}$ decay. The same-sign dilepton and multilepton channels together forms the SSML channel.	¹⁶⁴ 20
¹⁶⁵ Figure 3.1: The full CERN accelerator complex as of 2022.	22
¹⁶⁶ Figure 3.2: Current and future timeline of LHC operations as of 2025 with corresponding center-of-mass energies and projected integrated luminosities. .	¹⁶⁷ 23
¹⁶⁸ Figure 3.3: Summary of predicted and measured cross-section for SM processes at the LHC at different center-of-mass energies	¹⁶⁹ 25
¹⁷⁰ Figure 3.4: A cross section slice of the ATLAS detector showing different subsystems along with visualization of different types of particles traveling through the detector	¹⁷² 26
¹⁷³ Figure 3.5: Cutaway illustration of the inner detector along with its subsystems. . .	¹⁷³ 27

174	Figure 3.6: Cutaway illustration of the calorimeter system including the EM, hadronic 175 and LAr forward calorimeters	29
176	Figure 4.1: Stages of topo-cluster formation corresponding to each threshold. In (a), 177 proto-clusters are seeded from cells with adequate signal significance $\zeta_{\text{cell}}^{\text{EM}}$. 178 The clusters are further merged and split in (b) according to a predefined 179 cluster growth threshold. The process stops in (c) when all sufficiently 180 significant signal hits have been matched to a cluster.	36
181	Figure 4.2: Jet energy scale calibration sequence for EM-scale jets.	38
182	Figure 4.3: Overview of the GN2 architecture. The number of jet and track features 183 are represented by n_{jf} and n_{tf} respectively. The global jet representation 184 and track embeddings output by the Transformer encoder are used as 185 inputs for three task-specific networks.	40
186	Figure 4.4: The c -, light- and τ -jet rejection rate as a function of b -tagging efficiency 187 for GN2 and DL1d using (a) jets in the $t\bar{t}$ sample, and (b) jets in the Z' 188 sample. The performance ratios of GN2 to DL1d are shown in the bottom 189 panels.	41
190	Figure 6.1: Post-fit background composition in each analysis region and sub-region. 191 The fit was performed using ideal pseudo-datasets (Asimov data) in the SR.	57
192	Figure 6.2: Pre-fit kinematic distributions and event compositions for several observ- 193 ables in the inclusive SR. The shaded band represents the uncertainty in 194 the total distribution. The first and last bins of each distribution contains 195 underflow and overflow events respectively.	60
196	Figure 6.3: Charge flip rate calculated for SR and CR $t\bar{t}W$ in bins of $ \eta $ and p_{T}	66
197	Figure 7.1: Combined QmisID uncertainty rate for SR in bins of $ \eta $ and p_{T}	77
198	Figure 8.1: Observed (solid line) and expected (dotted line) upper limits as a function 199 of the Z' mass at 95% CL on the cross-section of $pp \rightarrow t\bar{t}Z'$ production 200 times the $Z' \rightarrow t\bar{t}$ branching ratio. The region above the observed limit is 201 excluded. The solid blue line represents the theoretical signal cross-section 202 with $c_t = 1$ at LO in QCD. The green and yellow bands represent the 203 68% ($\pm\sigma$) and 95% ($\pm 2\sigma$) confidence intervals respectively.	84
204	Figure 8.2: Comparison between data and post-fit prediction for the discriminant ob- 205 servable in each non-prompt and $t\bar{t}W$ background CR. The fit is per- 206 formed simultaneously in all CRs and SR under the background-only 207 hypothesis. The lower panel shows the ratio between data and post-fit 208 predictions. The shaded band represents the total uncertainty on the fit.	85

KEY TO ABBREVIATIONS

210

Physical & Mathematical Quantities

211 χ^2 chi-squared212 d_0 transverse impact parameter213 ΔR angular distance214 \sqrt{s} center-of-mass energy215 η pseudorapidity216 E_T transverse energy217 E_T^{miss} missing transverse energy218 Γ decay width219 γ_5 chirality projection operator220 γ_μ Dirac matrices221 H_0 null hypothesis222 H_T scalar sum of transverse momenta p_T of all objects in an event223 \mathcal{L} Lagrangian224 $\mathcal{L}(\theta)$ likelihood function225 L instantaneous luminosity226 $m_{\ell\ell}$ dilepton invariant mass227 μ signal strength228 μ_F factorization scale229 μ_R renormalization scale230 N_{jets} number of jets/jet multiplicity231 $\mathcal{O}(n)$ on the order of n 232 \mathcal{P} Poisson probability233 p_T transverse momentum

- ²³⁴ Q electric charge
²³⁵ q_μ profile likelihood ratio
²³⁶ σ standard deviation
²³⁷ $\sigma[b]$ cross-section
²³⁸ z_0 longitudinal impact parameter

Particles & Processes

- ²³⁹
- ²⁴⁰ γ^* virtual photon
²⁴¹ gg gluon-gluon fusion
²⁴² pp proton-proton
²⁴³ PbPb lead-lead
²⁴⁴ q quark
²⁴⁵ $q\bar{q}$ quark-antiquark pair
²⁴⁶ $t\bar{t}$ top/anti-top quark pair
²⁴⁷ $t\bar{t}X$ top pair in association with another particle
²⁴⁸ $t\bar{t}t\bar{t}$ four-top-quark
²⁴⁹ V massive vector bosons (W^\pm, Z)
²⁵⁰ H Higgs in association with a vector boson

Acronyms

- ²⁵¹
- ²⁵² **1LOS** one lepton, or two leptons of opposite charges
²⁵³ **2HDM** two-Higgs doublet model
²⁵⁴ **AF3** AtlFast3 fast simulation
²⁵⁵ **ALICE** A Large Ion Collider Experiment
²⁵⁶ **ATLAS** A Toroidal LHC ApparatuS
²⁵⁷ **AWAKE** Advanced WAKEfield Experiment
²⁵⁸ **BDT** boosted decision tree
²⁵⁹ **BR** branching ratio

- ²⁶⁰ **BSM** Beyond the Standard Model
- ²⁶¹ **CB** combined muon
- ²⁶² **CERN** European Organization for Nuclear Research
- ²⁶³ **CKM** Cabibbo-Kobayashi-Maskawa matrix
- ²⁶⁴ **CL** confidence level
- ²⁶⁵ **CMS** Compact Muon Solenoid
- ²⁶⁶ **CP** charge-parity symmetry
- ²⁶⁷ **CR** control region
- ²⁶⁸ **CSC** Cathode Strip Chambers
- ²⁶⁹ **CTP** Central Trigger Processor
- ²⁷⁰ **ECIDS** Electron Charge ID Selector
- ²⁷¹ **EFT** effective field theory
- ²⁷² **EM** electromagnetic
- ²⁷³ **EW** electroweak
- ²⁷⁴ **FASER** ForwArd Search ExpeRiment
- ²⁷⁵ **FCal** forward calorimeter
- ²⁷⁶ **FS** full detector simulation
- ²⁷⁷ **GNN** graph neural network
- ²⁷⁸ **GRL** Good Run List
- ²⁷⁹ **GSC** Global Sequential Calibration
- ²⁸⁰ **GSF** Gaussian-sum filter
- ²⁸¹ **GUT** Grand Unified Theory
- ²⁸² **HEC** hadronic endcap calorimeter
- ²⁸³ **HF** heavy-flavor
- ²⁸⁴ **HL-LHC** High-Luminosity Large Hadron Collider
- ²⁸⁵ **HLT** High-Level Trigger
- ²⁸⁶ **ID** Inner Detector

- ²⁸⁷ **IP** interaction point
- ²⁸⁸ **JER** jet energy resolution
- ²⁸⁹ **JES** jet energy scale
- ²⁹⁰ **JVT** Jet Vertex Tagger
- ²⁹¹ **KATRIN** Karlsruhe Tritium Neutrino Experiment
- ²⁹² **L1** Level 1
- ²⁹³ **LAr** liquid argon
- ²⁹⁴ **LF** light-flavor
- ²⁹⁵ **LH** likelihood
- ²⁹⁶ **LHC** Large Hadron Collider
- ²⁹⁷ **LHCb** Large Hadron Collider beauty
- ²⁹⁸ **LINAC** linear accelerator
- ²⁹⁹ **LLH** log-likelihood
- ³⁰⁰ **LO** leading order
- ³⁰¹ **MC** Monte Carlo simulation
- ³⁰² **ME** matrix element
- ³⁰³ **ML** multilepton
- ³⁰⁴ **MS** Muon Spectrometer
- ³⁰⁵ **MDT** Monitored Drift Tubes
- ³⁰⁶ **MET** missing transverse energy
- ³⁰⁷ **NF** normalization factor
- ³⁰⁸ **NNJvt** Neural Network-based Jet Vertex Tagger
- ³⁰⁹ **NLO** next-to-leading order
- ³¹⁰ **NNLO** next-to-next-to-leading order
- ³¹¹ **NP** nuisance parameter
- ³¹² **OP** operating point (also working point)
- ³¹³ **OS** opposite-sign

- ³¹⁴ **PCBT** pseudo-continuous b -tagging
- ³¹⁵ **PDF** parton distribution function
- ³¹⁶ **POI** parameter of interest
- ³¹⁷ **PS** parton shower
- ³¹⁸ **PV** primary vertex
- ³¹⁹ **QCD** quantum chromodynamics
- ³²⁰ **QED** quantum electrodynamics
- ³²¹ **QFT** quantum field theory
- ³²² **QmisID** charge mis-identification
- ³²³ **RPC** Resistive Plate Chamber
- ³²⁴ **SCT** Semiconductor Tracker
- ³²⁵ **SF** scale factor
- ³²⁶ **SM** Standard Model
- ³²⁷ **SR** signal region
- ³²⁸ **SS** same-sign
- ³²⁹ **SSB** spontaneous symmetry breaking
- ³³⁰ **SS2L** same-sign dilepton
- ³³¹ **SSML** same-sign dilepton, or more than two leptons of any charges
- ³³² **TDAQ** Trigger and Data Acquisition
- ³³³ **TGC** Thin-Gap Chamber
- ³³⁴ **TRT** Transition Radiation Tracker
- ³³⁵ **VEV** vacuum expectation value
- ³³⁶ **VR** validation region
- ³³⁷ **UE** underlying-event

³³⁸ Chapter 1. Introduction

³³⁹ The 20th century ushered in a revolutionary period for mankind's understanding of the
³⁴⁰ fundamental nature of matter and the forces that govern our universe with the development
³⁴¹ of special relativity and quantum mechanics, which redefined our understanding of space,
³⁴² time, energy and matter at the furthest extremes of scale from the vast reaches of the cosmos
³⁴³ to the tiniest constituents of matter. Building on these principles, Quantum Electrodynamics
³⁴⁴ (QED) [1–3] was developed as the first successful quantum field theory (QFT) describing
³⁴⁵ electromagnetism. The discovery of beta decay [4] and its paradoxical behaviors within the
³⁴⁶ framework of QED prompted the prediction of neutrinos and development of the theory of
³⁴⁷ weak interaction.

³⁴⁸ At around the same time, a spectrum of strongly interacting particles was discovered
³⁴⁹ [5] as particle accelerators probed deeper into atomic nuclei, leading to the formation of
³⁵⁰ the quark model in the 1960s and with it a hypothesized new binding force, the strong
³⁵¹ force. However, the QFT framework remained incapable of describing the weak and strong
³⁵² interactions until advancements in gauge theory and the quantization of non-Abelian gauge
³⁵³ via QFT resulted in the formation of Yang-Mills theory [6, 7]. This sparked a renaissance
³⁵⁴ in modern physics with the unification of electromagnetism and weak force in 1967 under
³⁵⁵ the framework of electroweak (EW) [8] theory, as well as the development of Quantum
³⁵⁶ Chromodynamics (QCD) [9, 10] to describe the strong force binding quarks.

³⁵⁷ At this point, the prediction of massless bosons within EW formalism remained a contra-
³⁵⁸ diction to the predicted massive W^\pm and Z bosons that mediate the weak force. This was
³⁵⁹ resolved by the introduction of EW spontaneous symmetry breaking and the Higgs mech-
³⁶⁰ anism in 1964 [11–13], which explained the generation of masses for both the EW bosons

361 and fermions. Together, these developments culminated in the Standard Model of parti-
362 cle physics SM [14], a comprehensive theory that described the electromagnetic, weak, and
363 strong interactions, classified all known fundamental particles and predicted mathematically
364 consistent but not yet observed particles. Following its inception, particles predicted by the
365 Standard Model were gradually observed experimentally, starting with the gluon in 1979
366 [15], then the W^\pm and Z bosons [16, 17], and finally the top quark in 1995 [18, 19]. The
367 final missing piece was confirmed as the Higgs boson was observed in 2012 independently
368 by the ATLAS [20] and CMS [21] detectors at the Large Hadron Collider, completing the
369 Standard Model after a 40-year search and cementing it as the most successful framework
370 so far describing fundamental constituents of matter and their governing forces.

371 Despite its successes, the Standard Model remains incomplete. Key unanswered questions
372 include the nature of dark matter [22], which makes up about 27% of the universes energy
373 content but has no explanation within the Standard Model; the origin of neutrino masses and
374 their oscillations [23]; the observed matter-antimatter asymmetry in the universe; possible
375 unification of the EW and strong interaction into a Grand Unified Theory (GUT); and the
376 hierarchy problem describing the large discrepancy in scales between forces and the apparent
377 lightness of the Higgs boson compared to values predicted from quantum corrections.

378 After the discovery of the Higgs boson, efforts have been underway to construct new
379 hypotheses and models in search of beyond the Standard Model (BSM) physics via different
380 avenues, one of which being direct searches at colliders for new resonances or particles not
381 predicted by the SM. In particular, the top quark possesses large mass and strong coupling to
382 the Higgs boson [24] which gives it a special role in many proposed BSM models as a possible
383 connection with strong coupling to new particles and heavy resonances. In addition, the
384 top quark has a clean decay signature with well-understood final states and is produced in

abundance at the LHC from pp collisions in the form of top pairs $t\bar{t}$ [25, 26]. This dissertation presents a search for the production of a heavy resonance that couples preferentially to top quark (top-philic) in association with a top pair ($t\bar{t}$) in the final state with either two leptons of the same electric charge or at least three leptons (SSML). The search is performed in proton-proton collisions at $\sqrt{s} = 13$ TeV with the ATLAS detector [27] via the four-top ($t\bar{t}t\bar{t}$) production channel.

A similar search for top-philic heavy resonances was performed using a $t\bar{t}t\bar{t}$ final state containing either one lepton or two opposite-sign leptons (1LOS) [28] with a much larger branching ratio of 56% and larger irreducible background of SM processes. Despite the small cross-section within the SM, the $t\bar{t}t\bar{t}$ SSML final state provides heightened sensitivity to BSM physics and higher signal-to-background ratio than inclusive resonance searches (e.g. in dijet or dilepton final states) due to the distinctive signal signature and suppression of large SM background processes present in $t\bar{t}$ -associated production i.e. diboson (VV), $t\bar{t}$ production with an additional boson ($t\bar{t}V/ttH+jets$) or with additional light leptons from heavy-flavor decays ($t\bar{t} + HF$). The cross-section for $t\bar{t}t\bar{t}$ production can be enhanced by many proposed BSM models including supersymmetric gluino pair-production [29, 30], scalar gluon pair-production [31, 32], top-quark-compositeness models [33, 34], effective field theory (EFT) operators [26, 35–38] and two-Higgs-doublet models (2HDM) [39–43]. Searching within this channel is particularly motivated by the recent observed excess in the measurement of four-top production in the SSML final state at the LHC by the ATLAS detector [44] with a measured cross-section of 24^{+7}_{-6} fb, almost double the SM prediction of $13.4^{+1.0}_{-1.8}$ fb.

A simplified color-singlet vector boson model [45] is employed for the search to minimize parameter dependency on model choice. Data-driven background estimation methods are implemented for $t\bar{t}W$ - one of the dominant irreducible backgrounds in the analysis - and

409 the charge misidentification background to rectify mismodeling related to jet multiplicity
410 in simulated background that were not covered in the previous 1LOS search [28]. These
411 methods are employed similarly to that in previous SM $t\bar{t}t\bar{t}$ analyses [44, 46].

412 This dissertation is organized as follows. Chapter 2 presents the formalism of the SM and
413 relevant BSM concepts. Chapter 3 provides an introduction to the LHC and ATLAS detector.
414 Chapter 4 describes the reconstruction and identification of physics object from detector
415 signals. Chapter 5 defines the data and simulated samples used in the analysis. Chapter 6
416 describes the analysis strategy, including object definition, analysis region description and
417 background estimation methods. Chapter 7 summarizes the uncertainties involved in the
418 analysis. Chapter 8 presents the statistical interpretation and analysis results. Finally,
419 Chapter 9 discusses a summary of the analysis and future outlook.

420 Chapter 2. Theoretical Overview

421 2.1 The Standard Model

422 The Standard Model of Physics (SM) [47] is currently the most successful formalism to
423 describe the physical world at a microscopic scale by providing descriptions for all currently
424 known elementary particles, along with three out of four fundamental forces (electromag-
425 netism, weak force, strong force) with the exception of gravity. The SM is however not
426 perfect, and there remains unanswered questions that require development and discovery
427 of new physics beyond the Standard Model (BSM). This chapter describes an overview of
428 important components within the SM and relevant BSM aspects for this analysis.

429 2.1.1 Elementary particles

430 Elementary particles in the SM can be classified into two groups: bosons consisting
431 of particles following Bose-Einstein statistics with integer spin, and fermions consisting of
432 particles following Fermi-Dirac statistics with half-integer spin. Fermions are the building
433 blocks of composite particles and consequently all known matter, and can be further classified
434 into quarks & leptons. Bosons act as force mediators for all fundamental forces described by
435 the SM, and can either be a scalar boson with spin 0 or vector gauge bosons with spin 1. For
436 each elementary particle, there also exists a corresponding antiparticle with identical mass
437 and opposite charge (electric or color). Figure 2.1 shows all known elementary particles in
438 the SM.

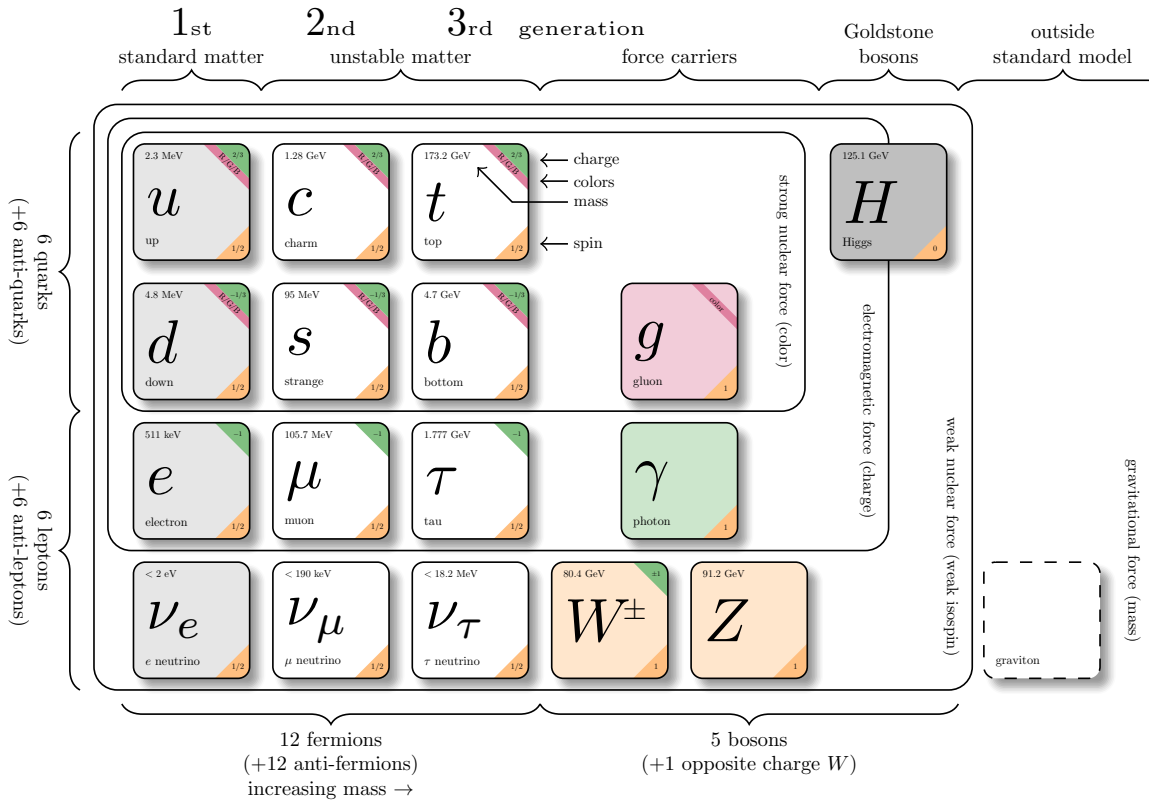


Figure 2.1: Particles within the SM and their properties [48].

439 Fermions

440 Fermions consist of quarks and leptons with six flavors each, grouped into three genera-
 441 tions of doublets. The six quark flavors are up (u), down (d), charm (c), strange (s), bottom
 442 (b) and top (t), arranged in increasing order of mass. The quark flavors form three doublets
 443 (u, d), (c, s) and (t, b), with each doublet containing one quark with electric charge of $+2/3$
 444 (u, s, t), and the other with charge of $-1/3$ (d, c, b). Each quark also possesses a property
 445 known as color charge, with possible values of red (R), green (G), blue (B) or their corre-
 446 sponding anticolor ($\bar{R}, \bar{G}, \bar{B}$). Color charge follows color confinement rules, which allows
 447 only configurations of quarks with total neutral color charge to exist in isolation. Neutral

448 charge configurations can be formed from either a set of three colors (R, G, B), a set of a
449 color and its anticolor, or any combination of the two. Consequently, quarks can only exist
450 in bound states called hadrons and no isolated quark can be found in a vacuum. Quarks are
451 the only elementary particles in the SM that can interact with all four fundamental forces.

452 The three leptons doublets consist of three charged leptons: electron (e), muon (μ), tau
453 (τ), and their respective neutrino flavors: electron neutrino (ν_e), muon neutrino (ν_μ), tau
454 neutrino (ν_τ). Charged leptons carry an electric charge of -1 , while their antiparticles carry
455 the opposite charge ($+1$) and their corresponding neutrino flavors carry no charge. Charged
456 leptons interact with all fundamental forces except the strong force, while neutrinos only
457 interact with the weak force and gravity.

458 **Bosons**

459 The SM classifies bosons into two types: one scalar boson with spin 0 known as the
460 Higgs (H) boson, and vector gauge bosons with spin 1 known as gluons (g), photon (γ), W^\pm
461 and Z bosons [22]. Gluons and photon are massless, while the W^\pm , Z and H bosons are
462 massive. Each vector gauge boson serves as the mediator for a fundamental force described
463 by the SM. Gluons are massless particles mediating the strong interaction by carrying color
464 charges between quarks following quantum chromodynamics (QCD). Each gluon carries a
465 non-neutral color charge out of eight linearly independent color states in the gluon color octet
466 [49]. The photon is the massless and charge-neutral mediator particle for the electromagnetic
467 interaction following quantum electrodynamics (QED). The W^\pm and Z bosons are massive
468 mediator particles for the weak interaction, with the W^\pm boson carrying an electric charge
469 of ± 1 while the Z boson is charge neutral.

470 Other than the vector gauge boson, the only scalar boson in the SM is the massive and

471 charge neutral Higgs boson [22]. The Higgs boson does not mediate any fundamental force
 472 like vector bosons, but serve to provide the rest mass for all massive elementary particles in
 473 the SM through the Higgs mechanism described in section 2.1.2.3.

474 **Top quark**

475 As of now, the top quark (t) is the heaviest particle in the SM with mass of about 173 GeV
 476 [50], approaching the EW symmetry breaking scale. Its high mass gives the top quark the
 477 strongest Yukawa coupling to the Higgs boson ($y_t \approx 1$) [24] and exotic resonances in many
 478 proposed BSM models [51–54], making the top quark and its processes attractive vehicles
 479 with which to probe new physics.

480 Due to its mass, the top quark has a

481 very short lifetime of 10^{-24} s [22] and de-
 482 cays before it can hadronize following color
 483 confinement. The top quark decays to a W
 484 boson and a b -quark with a branching ratio
 485 of almost 100%. The W boson can subse-
 486 quently decay to a quark-antiquark pair or
 487 to a lepton-neutrino pair (Figure 2.2), with
 488 branching ratios of approximately 68% and
 489 32% respectively. All lepton flavors have
 490 similar branching ratios during a leptonic W
 491 decay, assuming lepton universality.

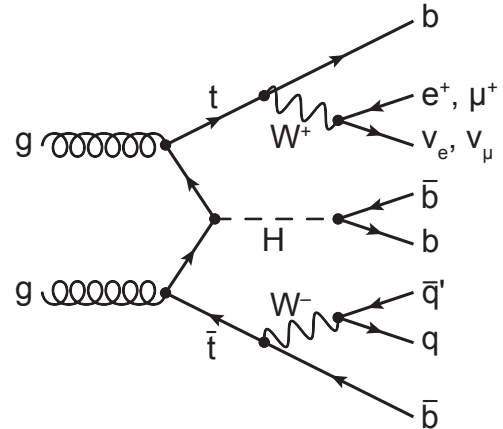


Figure 2.2: Feynman diagram for $t\bar{t}$ production and subsequent decay processes [55]. Top quark decays into a W -boson and b -quarks, and W -boson can decay to a $q\bar{q}$ or a $\ell\nu_\ell$ pair.

492 2.1.2 Mathematical formalism

493 The SM can be described within the formalism of quantum field theory (QFT) with the
494 Lagrangian [56]

$$\mathcal{L}_{\text{SM}} = \mathcal{L}_{\text{QCD}} + \underbrace{(\mathcal{L}_{\text{gauge}} + \mathcal{L}_{\text{fermion}} + \mathcal{L}_{\text{Higgs}} + \mathcal{L}_{\text{Yukawa}})}_{\mathcal{L}_{\text{EW}}} \quad (2.1)$$

495 where \mathcal{L}_{QCD} is the QCD term and \mathcal{L}_{EW} is the electroweak (EW) term of the Lagrangian.
496 Formalism of QFT within the SM treats particles as excitations [57] of their corresponding
497 quantum fields i.e. fermion field ψ , electroweak boson fields $W_{1,2,3}$ & B , gluon fields G_α and
498 Higgs field ϕ .

499 The foundation of modern QFT involves gauge theory. A quantum field has gauge sym-
500 metry if there exists a continuous gauge transformation that when applied to every point in
501 a field (local gauge transformation) leaves the field Lagrangian unchanged. The set of gauge
502 transformations of a gauge symmetry is the symmetry group of the field which comes with
503 a set of generators, each with a corresponding gauge field. Under QFT, the quanta of these
504 gauge fields are called gauge bosons.

505 The SM Lagrangian is gauge invariant under global Poincaré symmetry and local $SU(3)_C \times$
506 $SU(2)_L \times U(1)_Y$ gauge symmetry, with the $SU(3)_C$ symmetry group corresponding to the
507 strong interaction and $SU(2)_L \times U(1)_Y$ to the EW interaction. Global Poincaré symmetry
508 ensures that \mathcal{L}_{SM} satisfies translational symmetry, rotational symmetry and Lorentz boost
509 frame invariance [58]. These symmetries give rise to corresponding conservation laws, which
510 lead to conservation of momentum, angular momentum and energy in the SM as a result of
511 Noether's theorem [59].

512 **2.1.2.1 Quantum chromodynamics**

513 Quantum chromodynamics is a non-Abelian gauge theory i.e. Yang-Mills theory [6, 7]
514 describing the strong interaction between quarks in the SM with the gauge group $SU(3)_C$,
515 where C represents conservation of color charge under $SU(3)_C$ symmetry. According to
516 QFT, quarks can be treated as excitations of the corresponding quark fields ψ . The free Dirac
517 Lagrangian for the quark fields $\mathcal{L}_0 = \bar{\psi}(i\gamma^\mu\partial_\mu - m)\psi$ is invariant under global $SU(3)$ sym-
518 metry, but not under local $SU(3)_C$ symmetry. To establish invariance under local $SU(3)_C$
519 symmetry, the gauge covariant derivative D_μ is defined so that

$$D_\mu\psi = (\partial_\mu - ig_s G_\mu^a T_a)\psi, \quad (2.2)$$

520 where $g_s = \sqrt{4\pi\alpha_s}$ is the QCD coupling constant, $G_\mu^a(x)$ are the eight gluon fields, and
521 T_a are generators of $SU(3)_C$, represented as $T_a = \lambda_a/2$ with λ_a being the eight Gell-Mann
522 matrices [49]. Let the gluon field strength tensors $G_{\mu\nu}^a$ be

$$G_{\mu\nu}^a \equiv \partial_\mu G_\nu^a - \partial_\nu G_\mu^a - g_s f^{abc} G_\mu^b G_\nu^c, \quad (2.3)$$

523 where f^{abc} are the structure constants of $SU(3)_C$. The gauge invariant QCD Lagrangian
524 can then be written as

$$\begin{aligned} \mathcal{L}_{\text{QCD}} &= \bar{\psi}(i\gamma^\mu D_\mu - m)\psi - \frac{1}{4}G_{\mu\nu}^a G_a^{\mu\nu} \\ &= \underbrace{-\frac{1}{4}G_{\mu\nu}^a G_a^{\mu\nu}}_{\text{gluon kinematics}} + \underbrace{\bar{\psi}(i\gamma^\mu\partial_\mu - m)\psi}_{\text{quark kinematics}} + \underbrace{\bar{\psi}^i(g_s\gamma^\mu(T_a)_{ij}G_\mu^a)\bar{\psi}^j}_{\text{quark-gluon interaction}}, \end{aligned} \quad (2.4)$$

525 where i, j are color indices with integer values from 1 to 3. Gluons are forced to be massless
526 from the lack of a gluon mass term to maintain gauge invariance for the Lagrangian.

527 **2.1.2.2 Electroweak theory**

528 The electroweak interaction is the unified description of the weak interaction and electro-
529 magnetism under the $SU(2)_L \times U(1)_Y$ symmetry group, where L represents the left-handed
530 chirality of the weak interaction and Y represents the weak hypercharge quantum number.
531 Fermions can have either left-handed or right-handed chirality with the exception of neutrili-
532 nos which can only have left-handed chirality in the SM, and can be divided into left-handed
533 doublets and right-handed singlets

$$\psi_L = \begin{pmatrix} \nu_e \\ e_L \end{pmatrix}, \begin{pmatrix} \nu_\mu \\ \mu_L \end{pmatrix}, \begin{pmatrix} \nu_\tau \\ \tau_L \end{pmatrix}, \begin{pmatrix} u_L \\ d_L \end{pmatrix}, \begin{pmatrix} c_L \\ s_L \end{pmatrix}, \begin{pmatrix} t_L \\ b_L \end{pmatrix} \quad (2.5)$$

$$\psi_R = e_R, \mu_R, \tau_R, u_R, d_R, c_R, s_R, t_R, b_R.$$

534 where g' is the B_μ coupling constant and $B_\mu(x)$ is a vector gauge field that transforms under
535 $U(1)_Y$ as

$$B_\mu \rightarrow B_\mu + \frac{1}{g'} \partial_\mu \theta(x). \quad (2.6)$$

536 Right-handed fermion singlets are not affected by $SU(2)_L$ transformation, so the fermion
537 fields ψ transform under $SU(2)_L$ as

$$\psi_L \rightarrow e^{i I_3 \vec{\theta}(x) \cdot \vec{\sigma}/2} \psi_L \quad (2.7)$$

$$\psi_R \rightarrow \psi_R.$$

538 where $\vec{\sigma}/2$ are generators of $SU(2)_L$ with $\vec{\sigma}$ being the Pauli matrices. In order to preserve
539 local symmetry, the gauge covariant derivative for $SU(2)_L$ and $U(1)_Y$ can be defined [60] so

⁵⁴⁰ that the gauge covariant derivative for $SU(2)_L \times U(1)_Y$ can be written as

$$\begin{aligned} D_\mu \psi_L &= \left(\partial_\mu - ig' \frac{Y_L}{2} B_\mu - ig \frac{\sigma_i}{2} W_\mu^i \right) \psi_L \\ D_\mu \psi_R &= \left(\partial_\mu - ig' \frac{Y_R}{2} B_\mu \right) \psi_R. \end{aligned} \quad (2.8)$$

⁵⁴¹ where $B_\mu(x)$ is a vector gauge field associated with $U(1)_Y$ and $W_\mu^i(x)$ ($i = 1, 2, 3$) are three
⁵⁴² vector gauge fields associated with $SU(2)_L$. The B_μ and W_μ^i gauge fields transform under
⁵⁴³ their corresponding symmetry groups $U(1)_Y$ and $SU(2)_L$ as

$$\begin{aligned} B_\mu &\rightarrow B_\mu + \frac{1}{g'} \partial_\mu \theta(x) \\ W_\mu^i &\rightarrow W_\mu^i + \frac{2}{g} \partial_\mu \theta_a(x) + \epsilon^{ijk} \theta_j(x) W_\mu^k, \end{aligned} \quad (2.9)$$

⁵⁴⁴ where g' is the B_μ gauge coupling constant, g is the W_μ^i gauge coupling constants and ϵ^{ijk}
⁵⁴⁵ is the $SU(2)_L$ structure constant. Similar to section 2.1.2.1, the kinetic term is added by
⁵⁴⁶ defining field strengths for the four gauge fields

$$\begin{aligned} B_{\mu\nu} &\equiv \partial_\mu B_\nu - \partial_\nu B_\mu \\ W_{\mu\nu}^i &\equiv \partial_\mu W_\nu^i - \partial_\nu W_\mu^i - g e^{ijk} W_\mu^j W_\nu^k. \end{aligned} \quad (2.10)$$

⁵⁴⁷ The local $SU(2)_L \times U(1)_Y$ invariant EW Lagrangian [60] is then

$$\begin{aligned} \mathcal{L}_{\text{EW}} &= i \bar{\psi} (\gamma^\mu D_\mu) \psi - \frac{1}{4} W_{\mu\nu}^i W_i^{\mu\nu} - \frac{1}{4} B_{\mu\nu} B^{\mu\nu} \\ &= \underbrace{i \bar{\psi} (\gamma^\mu \partial_\mu) \psi}_{\text{fermion kinematics}} - \underbrace{\bar{\psi} \left(\gamma^\mu g' \frac{Y}{2} B_\mu \right) \psi}_{\text{fermion-gauge boson interaction}} - \underbrace{\bar{\psi}_L \left(\gamma^\mu g \frac{\sigma_i}{2} W_\mu^i \right) \psi_L}_{\text{boson kinematics \& self-interaction}} - \frac{1}{4} W_{\mu\nu}^i W_i^{\mu\nu} - \frac{1}{4} B_{\mu\nu} B^{\mu\nu}. \end{aligned} \quad (2.11)$$

548 Under ≈ 159.5 GeV, the EW symmetry $SU(2)_L \times U(1)_Y$ undergoes spontaneous symmetry
 549 breaking [61] into $U(1)_{\text{QED}}$ symmetry, which corresponds to a separation of the weak and
 550 electrodynamic forces. Electroweak spontaneous symmetry breaking replaces the four mass-
 551 less and similarly-behaved EW gauge bosons B_μ and W_μ^i with the EM boson γ and the weak
 552 bosons Z/W^\pm , as well as giving the Z and W^\pm bosons masses via the Higgs mechanism.
 553 This is due to a specific choice of gauge for the Higgs field leading to the reparameterization
 554 of the EW bosons B_μ and W_μ^i to $W^\pm/Z/\gamma$ using the relations

$$\begin{aligned}
 W_\mu^\pm &\equiv \frac{1}{\sqrt{2}} (W_\mu^1 \mp iW_\mu^2) \\
 \begin{pmatrix} A_\mu \\ Z_\mu \end{pmatrix} &\equiv \begin{pmatrix} \cos \theta_W & \sin \theta_W \\ -\sin \theta_W & \cos \theta_W \end{pmatrix} \begin{pmatrix} B_\mu \\ W_\mu^3 \end{pmatrix}
 \end{aligned} \tag{2.12}$$

555 where $\theta_W \equiv \cos^{-1} (g/\sqrt{g^2 + g'^2})$ is the weak mixing angle. The boson kinetic term can also
 556 be refactorized to extract cubic (three vertices) and quartic (four vertices) self-interactions
 557 among the gauge bosons [60]. The Lagrangian can then be rewritten as

$$\begin{aligned}
 \mathcal{L} = & \underbrace{eA_\mu \bar{\psi} (\gamma^\mu Q) \psi}_{\text{electromagnetism}} + \underbrace{\frac{e}{2 \sin \theta_W \cos \theta_W} \bar{\psi} \gamma^\mu (v_f - a_f \gamma_5) \psi Z_\mu}_{\text{neutral current interaction}} \\
 & + \underbrace{\frac{g}{2\sqrt{2}} \sum_{\psi_L} [\bar{f}_2 \gamma^\mu (1 - \gamma_5) f_1 W_\mu^+ + \bar{f}_1 \gamma^\mu (1 - \gamma_5) f_2 W_\mu^-]}_{\text{charged current interaction}} \\
 & + \underbrace{\mathcal{L}_{\text{kinetic}} + \mathcal{L}_{\text{cubic}} + \mathcal{L}_{\text{quartic}}}_{\text{boson self-interaction}}
 \end{aligned} \tag{2.13}$$

558 where $\gamma_5 = i\gamma^0\gamma^1\gamma^2\gamma^3$ is the chirality projection operator, $a_f = I_3$, $v_f = I_3(1 - 4|Q| \sin^2 \theta_W)$
 559 and f_1, f_2 are up and down type fermions of a left-handed doublet.

560 **2.1.2.3 Higgs mechanism**

561 So far, the EW bosons are massless since the mass terms $-m\bar{\psi}\psi$ for fermions and
562 $-mA^\mu A_\mu$ for bosons are not invariant under the EW Lagrangian symmetries. The parti-
563 cles must then acquire mass under another mechanism. The Brout-Engler-Higgs mechanism
564 [11–13] was introduced in 1964 to rectify this issue and verified in 2012 with the discovery
565 of the Higgs boson [20, 21].

566 The Higgs potential is expressed as

$$V(\phi^\dagger \phi) = \mu^2 \phi^\dagger \phi + \lambda (\phi^\dagger \phi)^2 \quad (2.14)$$

567 where μ^2 and $\lambda > 0$ are arbitrary parameters, and the $SU(2)_L$ doublet $\phi = \begin{pmatrix} \phi^+ \\ \phi^0 \end{pmatrix}$ is the Higgs
568 field with complex scalar fields ϕ^+ and ϕ^0 carrying +1 and 0 electric charge respectively.

569 The Lagrangian for the scalar Higgs field is

$$\mathcal{L}_H = (\partial_\mu \phi)^\dagger (\partial^\mu \phi) - V(\phi^\dagger \phi). \quad (2.15)$$

570 Since the potential $V(\phi^\dagger \phi)$ is constrained by $\lambda > 0$, the ground state is solely controlled by
571 μ . If $\mu^2 > 0$, the ground state energy is $\phi = 0$, and the EW bosons would remain massless.
572 If $\mu^2 < 0$, the ground state is

$$|\phi|^2 = -\frac{\mu^2}{2\lambda} \equiv \frac{v^2}{\sqrt{2}}, \quad (2.16)$$

573 where v is defined as the vacuum expectation value (VEV). The standard ground state for
574 the Higgs potential without loss of generality can be chosen as $\phi(0) = 1/\sqrt{2}(0)_v$.

575 Having $U(1)$ symmetry allows any $-e^{i\theta} \sqrt{\mu^2/\lambda}$ to be a ground state energy for the Higgs

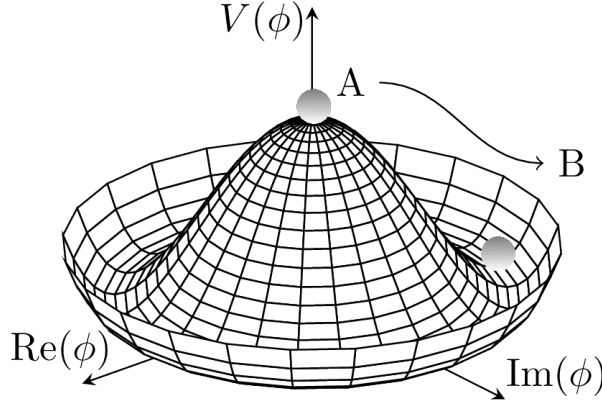


Figure 2.3: Illustration of a common representation of the Higgs potential [62]. Before SSB, the ground state $\phi(0)$ is located at A which is symmetric with respect to the potential. A perturbation to this state fixes the ground state energy $|\phi(0)|^2$ to a particular value at B, "spontaneously" breaking the symmetry and degeneracy in $|\phi(0)|^2$.

576 Lagrangian. This degeneracy results in spontaneous symmetry breaking of the $SU(2)_L \times$
 577 $U(1)_Y$ symmetry into $U(1)_{\text{EM}}$ symmetry when the Higgs field settles on a specific vacuum
 578 state as a result of a perturbation or excitation (Figure 2.3). The spontaneous symmetry
 579 breaking introduces three massless (Nambu-Goldstone [63]) vector gauge boson ξ and a
 580 massive scalar boson η , each corresponds to a generator of the gauge group. The vector field
 581 for ξ and η are real fields parameterized as $\xi \equiv \phi^+ \sqrt{2}$ and $\eta \equiv \phi^0 \sqrt{2} - v$ [64]. The Higgs
 582 field now becomes

$$\phi = \frac{v + \eta + i\xi}{\sqrt{2}} = \frac{1}{\sqrt{2}} e^{i\xi} \begin{pmatrix} 0 \\ v + \eta \end{pmatrix}. \quad (2.17)$$

583 Due to $U(1)_{\text{EM}}$ invariance, a unitary gauge with the transformation $\phi \rightarrow \exp(-i\xi \cdot) \frac{\sigma}{2v}$ can
 584 be chosen for the Higgs field to eliminate the massless bosons and incorporate them into the
 585 EM/weak bosons via Equation 2.12. This leaves the massive η which can now be observed as
 586 an excitation of the Higgs field from the standard ground state and must be the Higgs boson
 587 h . Using the EW covariant derivative from Equation 2.8, the Higgs Lagrangian around the

588 vacuum state becomes

$$\begin{aligned}\mathcal{L}_H &= (D_\mu \phi)^\dagger (D^\mu \phi) - \mu^2 \left(\frac{v+h}{\sqrt{2}} \right)^2 - \lambda \left(\frac{v+h}{\sqrt{2}} \right)^4 \\ &= (D_\mu \phi)^\dagger (D^\mu \phi) - \frac{1}{2} \mu^2 h^2 - \lambda v h^3 - \frac{\lambda}{4} h^4 - \dots\end{aligned}\tag{2.18}$$

589 The Higgs mass can be extracted from the quadratic term as $m_H = \sqrt{-2\mu^2}$. The kinetic

590 term in the Lagrangian can be written as

$$\begin{aligned}(D_\mu \phi)^\dagger (D^\mu \phi) &= \frac{1}{2} (\partial_\mu h)^2 + \frac{g^2}{8} (v+h)^2 \left| W_\mu^1 - i W_\mu^2 \right|^2 + \frac{1}{8} (v+h)^2 (g' W_\mu - g B_\mu) \\ &= \frac{1}{2} (\partial_\mu h)^2 + (v+h)^2 \left(\frac{g^2}{4} W_\mu^+ W^{-\mu} + \frac{1}{8} (g^2 + g'^2) Z_\mu^0 Z^{0\mu} \right).\end{aligned}\tag{2.19}$$

591 Masses for the EW bosons can be extracted from the quadratic terms

$$m_{W^\pm} = \frac{v}{2} g, \quad m_Z = \frac{v}{2} \sqrt{g^2 + g'^2}, \quad m_\gamma = 0.\tag{2.20}$$

592 However, the fermion mass term $-m\bar{\psi}\psi$ still breaks EW invariance after spontaneous symmetry breaking. Instead, fermions acquire mass by replacing the mass term with a gauge invariant Yukawa term in the EW Lagrangian representing fermions' interactions with the 594 Higgs field [64]

$$\begin{aligned}\mathcal{L}_{\text{Yukawa}} &= -c_f \frac{v+h}{\sqrt{2}} (\bar{\psi}_R \psi_L + \bar{\psi}_L \psi_R) \\ &= -\underbrace{\frac{c_f}{\sqrt{2}} v (\bar{\psi} \psi)}_{\text{fermion mass}} - \underbrace{\frac{c_f}{\sqrt{2}} (h \bar{\psi} \psi)}_{\text{fermion-Higgs interaction}},\end{aligned}\tag{2.21}$$

596 where c_f is the fermion-Higgs Yukawa coupling. The fermion mass is then $m_f = c_f v / \sqrt{2}$.

597 2.2 Beyond the Standard Model: $t\bar{t}Z' \rightarrow t\bar{t}t\bar{t}$

598 This analysis uses the $t\bar{t}t\bar{t}$ final state signal signature to search for the existence of a heavy
599 neutral BSM resonance that couples strongly to the top quark, nominally named Z' . Cross-
600 section for $t\bar{t}t\bar{t}$ production can be enhanced by many possible BSM models, in particular
601 production of heavy scalars and pseudoscalar bosons predicted in Type-II two-Higgs-doublet
602 models (2HDM) [39–43] or possible production of a heavy neutral resonance boson $Z'(\rightarrow t\bar{t})$
603 in association with a $t\bar{t}$ pair [74, 75]. The $t\bar{t}Z'$ production mode and consequently $t\bar{t}t\bar{t}$ signal
604 signature can provide a more sensitive channel for searches by avoiding contamination from
605 the large SM $gg \rightarrow t\bar{t}$ background in an inclusive $Z' \rightarrow t\bar{t}$ search.

606 2.2.1 Top-philic vector resonance

607 Many BSM models extend the SM by adding to the SM gauge group additional $U(1)'$
608 gauge symmetries [65, 66], each with an associated vector gauge boson (Z'). In the case of
609 a BSM global symmetry group with rank larger than the SM gauge group, the symmetry
610 group can spontaneously break into $G_{\text{SM}} \times U(1)'^n$, where G_{SM} is the SM gauge group
611 $SU(3)_C \times SU(2)_L \times U(1)_Y$ and $U(1)'^n$ is any $n \geq 1$ number of $U(1)'$ symmetries. The
612 existence of additional vector boson(s) Z' would open up many avenues of new physics e.g.
613 extended Higgs sectors from $U(1)'$ symmetry breaking [67, 68], existence of flavor-changing
614 neutral current (FCNC) mediated by Z' [69], and possible exotic production from heavy Z'
615 decays [70].

616 Due to the top quark having the largest mass out of all known elementary particles in the
617 SM, many BSM models [38–43, 71, 72] predict ‘top-philic’ vector resonances that have much
618 stronger coupling to the top quark compared to other quarks. Previous BSM $t\bar{t}t\bar{t}$ search for

619 top-philic resonances [28] with a similar model in the single-lepton final state and similar
 620 mass ranges set upper limits on observed (expected) Z' production cross section between 21
 621 (14) fb to 119 (86) fb depending on parameter choice. This analysis is also motivated by the
 622 recent observation of SM $t\bar{t}t\bar{t}$ production in the same-sign multilepton (SSML) channel by
 623 ATLAS [44] and CMS [73] at 6.1σ and 5.6σ discovery significance respectively.

624 A simplified color-singlet vector particle model [45, 71] is employed in the search. The
 625 interaction Lagrangian assumes only Z' to top coupling and has the form

$$\begin{aligned}
 \mathcal{L}_{Z'} &= \bar{t}\gamma_\mu (c_L P_L + c_R P_R) t Z'^\mu \\
 &= c_t \bar{t}\gamma_\mu (\cos\theta P_L + \sin\theta P_R) t Z'^\mu,
 \end{aligned} \tag{2.22}$$

626 where $c_t = \sqrt{c_L^2 + c_R^2}$ is the Z' -top coupling strength, $P_{L/R} = (1 \mp \gamma_5)/2$ are the chirality
 627 projection operators, and $\theta = \tan^{-1}(c_R/c_L)$ is the chirality mixing angle. Expanding the
 628 Lagrangian results in

$$\mathcal{L}_{Z'} = \frac{1}{\sqrt{2}} \bar{t}\gamma_\mu \left[\sin\left(\theta + \frac{\pi}{4}\right) - \left(\sqrt{2} \cos\left(\theta + \frac{\pi}{4}\right) \right) \gamma_5 \right] t Z'^\mu, \tag{2.23}$$

629 which bears striking resemblance to the EW Lagrangian neutral current interaction term in
 630 Equation 2.13, showing the similarity between the Z' and the Z boson that acquires mass
 631 from $SU(2)_L \times U(1)_Y$ spontaneous symmetry breaking. Assuming the Z' mass $m_{Z'}$ is much
 632 larger than the top mass ($m_t^2/m_{Z'}^2 \approx 0$), the Z' decay width at leading-order (LO) can be
 633 approximated as

$$\Gamma(Z' \rightarrow t\bar{t}) \approx \frac{c_t^2 m_{Z'}}{8\pi}. \tag{2.24}$$

634 It can be observed that $\Gamma/m_{Z'} \approx c_t^2/8\pi \ll 1$ for $c_t \approx 1$, which suggests a very narrow and

635 well-defined resonance peak, validating the narrow-width approximation for the choice of

636 $c_t = 1$.

637 2.2.2 Production channels

638 The main production channels for the aforementioned heavy topophilic color singlet Z'

639 are at tree level and loop level, with the one-loop level being the dominant processes [45].

640 Loop level processes are dependent on the chirality angle θ , where $\theta = \pi/4$ suppresses all

641 but gluon-initiated box sub-processes. To minimize model dependence, only the tree level

642 production was considered for this analysis by choosing $\theta = \pi/4$. Figure 2.4 illustrates

643 several tree level Z' production processes.

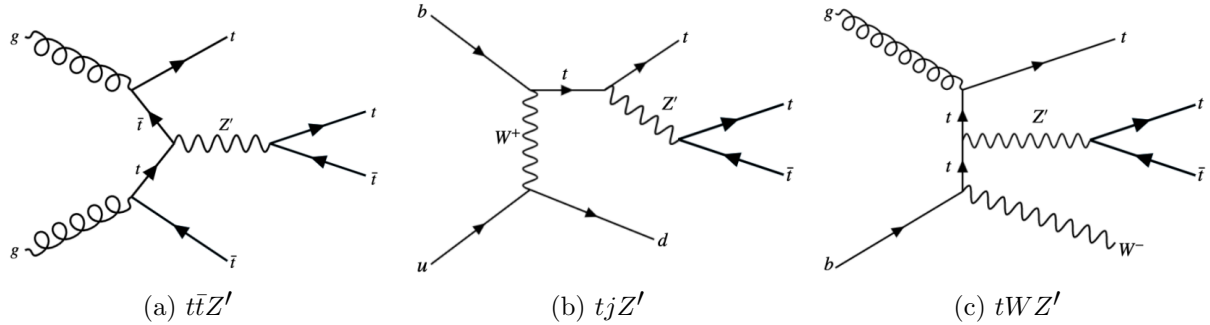


Figure 2.4: Feynman diagrams for tree level Z' production in association with (a) $t\bar{t}$, (b) tj (light quark) and (c) tW , decaying to final states containing (a) $t\bar{t}t\bar{t}$ or (b)(c) $t\bar{t}t$ [45].

644 The tree level $t\bar{t}$ -associated process $t\bar{t}Z'$ is the targeted production channel for the search

645 in this dissertation. Contributions from the single-top-associated channels tjZ' and tWZ'

646 are not considered due to a smaller cross-section by a factor of two compared to $t\bar{t}Z'$ due

647 to suppression in the three-body phase space [45]. Additionally, $t\bar{t}Z' \rightarrow t\bar{t}t\bar{t}$ production is

648 independent of θ while tjZ' and tWZ' are minimally suppressed under pure left-handed

649 interactions ($\theta = 0$) and maximally suppressed under pure right-handed interactions ($\theta =$

650 $\pi/2$); both channels are affected by the choice of $\theta = \pi/4$ to suppress loop level production.

651 **2.2.3 Decay modes**

652 The different W boson decay modes
653 shown in Figure 2.2 result in many differ-
654 ent final states for $t\bar{t}Z'/t\bar{t}\bar{t}$ decay, which
655 can each be classified into one of three chan-
656 nels shown in Figure 2.5: all hadronic de-
657 cays; exactly one lepton or two opposite-sign
658 leptons (1LOS); exactly two same-sign lep-
659 tons or three or more leptons (SSML). The
660 branching ratio for each channel is shown
661 in Figure 2.5. The all hadronic and 1LOS
662 channels have much larger branching ratios
663 compared to SSML channel but suffer heavily from $gg \rightarrow t\bar{t}$ background contamination,
664 giving the SSML channel better sensitivity at the cost of lower statistics. This is also the
665 targeted channel for this analysis.

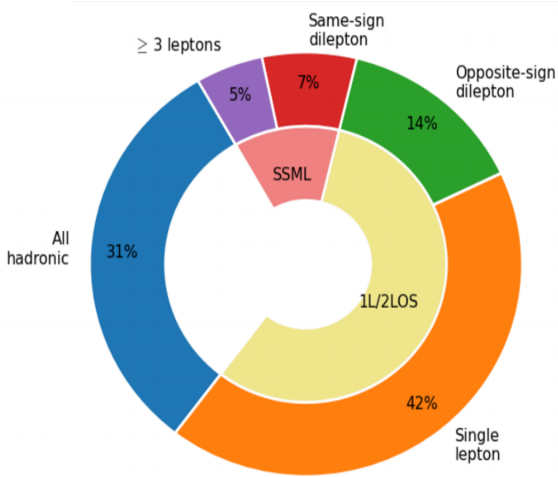


Figure 2.5: Branching ratios for $t\bar{t}t\bar{t}$ decay [76]. The same-sign dilepton and multilepton chan-
nels together forms the SSML channel.

666 Chapter 3. LHC & ATLAS Experiment

667 3.1 The Large Hadron Collider

668 Predictions from theoretical models are evaluated against experimental data collected
669 from particle detectors. This chapter provides a detailed overview of the Large Hadron
670 Collider (LHC) and the ATLAS detector, one of the key experiments designed to study
671 high-energy collisions at the LHC.

672 3.1.1 Overview

673 The Large Hadron Collider [77] (LHC) is currently the world's largest particle collider
674 with a circumference of almost 27 km. Built by CERN on the border of Switzerland and
675 France, the LHC is designed as a particle collider for proton-proton (pp), sometimes heavy
676 ions i.e. lead-lead (PbPb) and proton-lead (pPb) beams at TeV-scale energies. Two beams
677 of particles are injected into the LHC in opposite directions and allowed to collide at the
678 center of four major experiments:

- 679 • **A Toroidal LHC ApparatuS** (ATLAS) [27] and **Compact Muon Solenoid** (CMS)
680 [78]: multi-purpose detectors, designed to target a variety of phenomena including SM,
681 BSM and heavy-ion physics.
- 682 • **Large Ion Collider Experiment** (ALICE) [79]: specialized detector to record ion
683 collisions and study heavy-ion physics.
- 684 • **Large Hadron Collider beauty** (LHCb) [80]: detector dedicated to study properties
685 of b -quarks and b -hadrons.

686 Aside from the four major experiments, the LHC also houses smaller experiments e.g.
687 AWAKE [81], FASER [82], KATRIN [83], that either share an interaction point with one of
688 the above experiments or make use of particle beams pre-LHC injection.

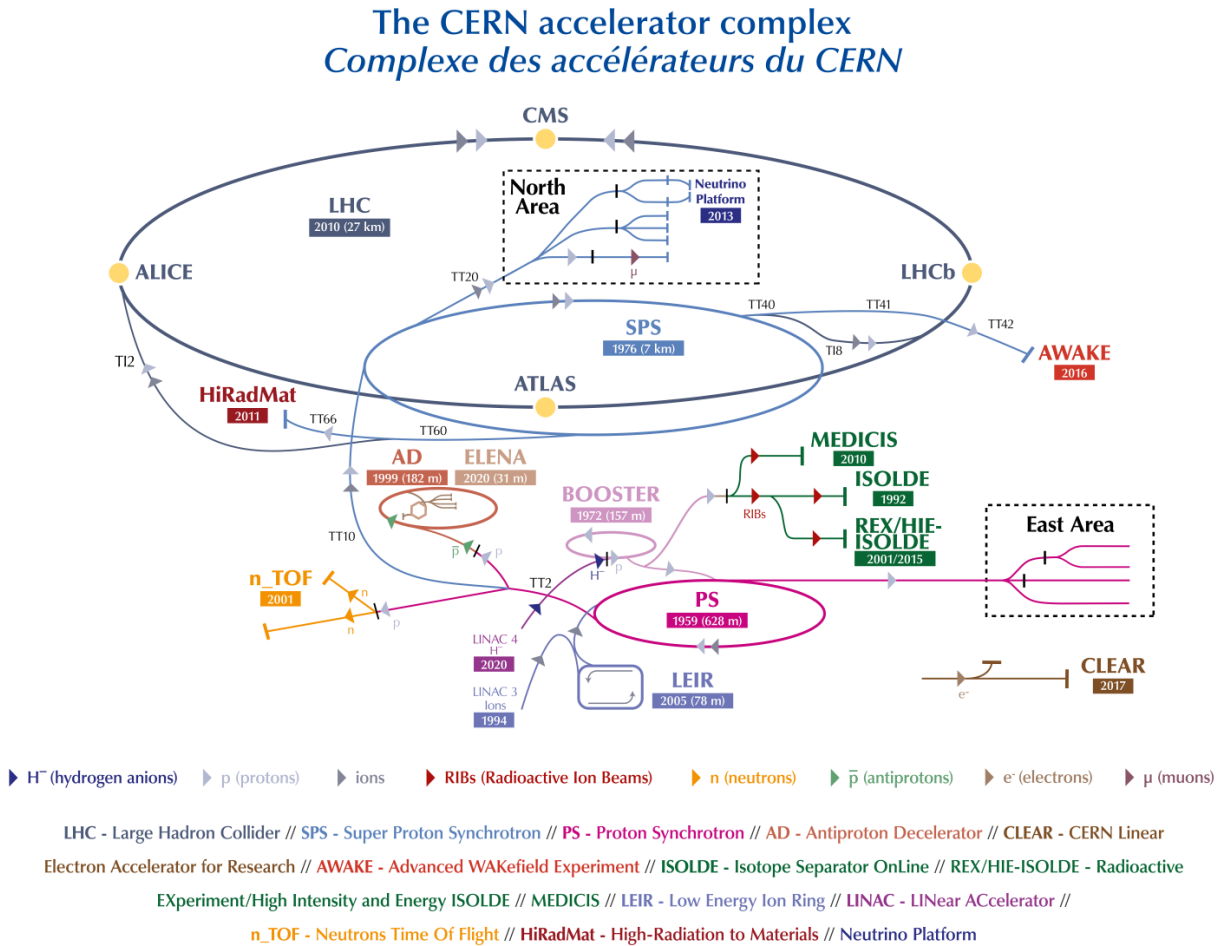


Figure 3.1: The full CERN accelerator complex as of 2022 [84].

689 The majority of the LHC operational time is dedicated to studying pp collisions of up to
690 ~ 13 TeV center-of-mass energy, denoted as \sqrt{s} . Reaching collision energy requires a sequence
691 of accelerators within the CERN accelerator complex, shown in Figure 3.1. Proton produc-
692 tion starts at LINAC 4, where hydrogen atoms are accelerated to 160 MeV then stripped
693 of electrons. The leftover proton beams are injected into the Proton Synchrotron Booster

694 (PSB) and accelerated to 2 GeV before being transferred into the Proton Synchrotron (PS).
 695 Here, the beams are ramped up to 26 GeV then injected into the Super Proton Synchrotron
 696 (SPS) to further raise the energy threshold to 450 GeV. The beams are finally injected into
 697 the LHC in opposite directions, continuously increasing in energy up to 6.5 TeV per beam,
 698 reaching the 13 TeV center-of-mass energy threshold necessary for collision during Run 2.
 699 As of the start of Run 3 in 2022, proton beams can now be ramped up to 6.8 TeV per beam
 700 for a total of $\sqrt{s} = 13.6$ TeV.

701 3.1.2 LHC operations

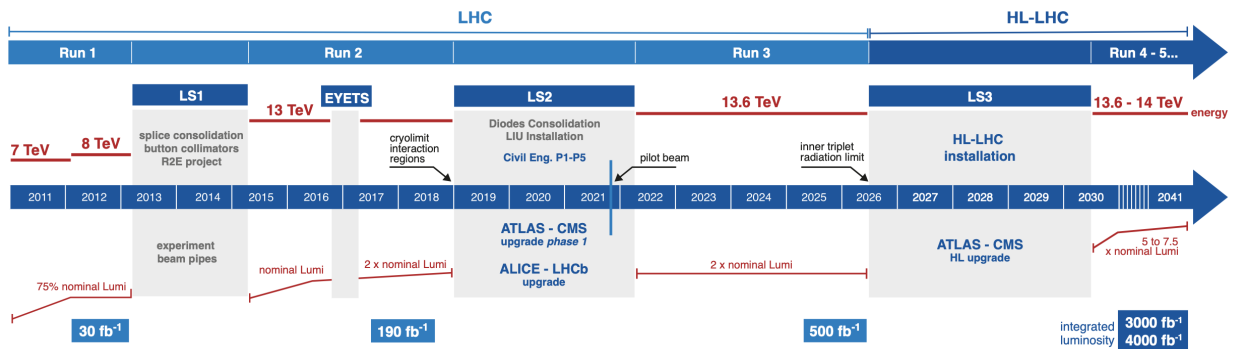


Figure 3.2: Current and future timeline of LHC operations with corresponding center-of-mass energies and projected integrated luminosities. [85].

702 Operations at the LHC are defined in periods of data-taking and shut-down known as
 703 runs and long shutdowns respectively; the first period (Run 1) started with first collisions
 704 at the LHC in 2010 at $\sqrt{s} = 7$ TeV [86]. Upgrades are usually carried out for detectors and
 705 accelerators during long shutdowns, raising the maximum energy threshold in preparation
 706 for the next run. An overview of the LHC runtime and corresponding center-of-mass energies
 707 are summarized in Figure 3.2. During Run 2 from 2015-2018, the ATLAS detector recorded
 708 a total of 1.1×10^{16} pp collisions at $\sqrt{s} = 13$ TeV, which corresponds to an integrated

709 luminosity of $140 \pm 0.83\% \text{ fb}^{-1}$ that passed data quality control and are usable for analyses
710 [87]. This is also the data set used for the analysis in this dissertation.

711 3.1.3 Physics at the LHC

712 The majority of physics studied at the LHC focus primarily on QCD proton-proton hard
713 scattering processes and the resulting products. Hard scattering processes involve large
714 momentum transfer compared to the proton mass e.g. top pair production ($gg \rightarrow t\bar{t}$) and
715 Higgs production ($gg \rightarrow H$), and can be predicted using perturbative QCD [88]. Hard
716 processes probe distance scales much lower than the proton radius and can be considered
717 collisions between the constituent quarks and gluons i.e. partons. Soft processes involve
718 lower momentum transfer between partons and are dominated by less well-understood non-
719 perturbative QCD effects. The hard interaction between two partons are represented by a
720 parton distribution function (PDF) $f_i(x, Q^2)$, which describes the probability of interacting
721 with a constituent parton i that carries a fraction x of the external hadron's momentum
722 when probed at a momentum scale of Q^2 [89]. Other partons within the hadron that did
723 not participate in the collision can still interact via lower momentum underlying-events
724 (UE). The probability of a particular interaction occurring is defined as its cross-section
725 $\sigma[b]$. Figure 3.3 gives an overview of SM processes produced within the LHC and their
726 cross-sections.

727 3.2 The ATLAS detector

728 One of the four main experiments at the LHC is ATLAS [27], designed as a multi-purpose
729 detector for the role of studying high-energy physics in pp and heavy-ion collisions. ATLAS

Standard Model Production Cross Section Measurements

Status: October 2023

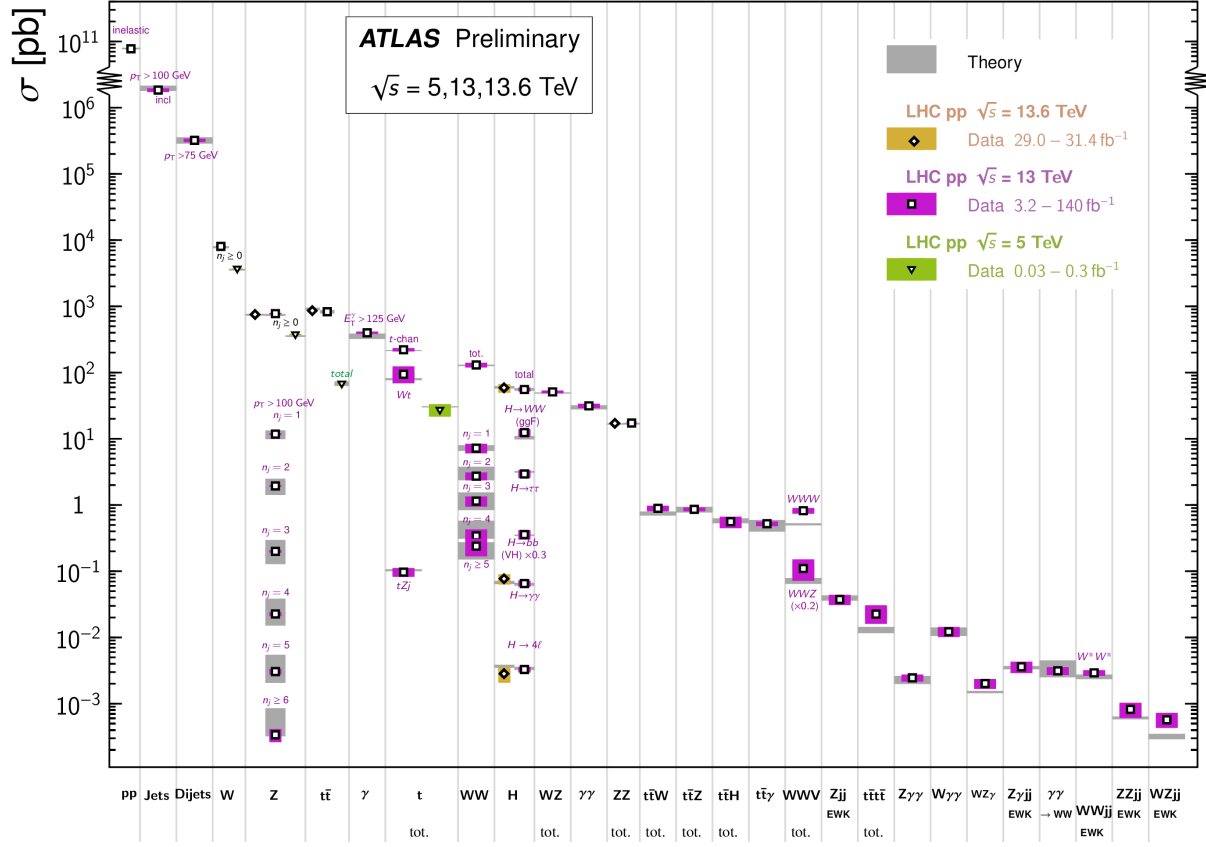


Figure 3.3: Summary of predicted and measured cross-section for SM processes at the LHC at different center-of-mass energies [90].

730 is a detector with symmetric cylindrical geometry with dimensions of 44 m in length and 25
 731 m in diameter, covering a solid angle of almost 4π around the collision point. The detector is
 732 built concentrically around the beamline with the collision point at the center to maximally
 733 capture signals produced by interactions. Figure 3.4 shows a slice of the ATLAS detector.
 734 From the inside out, the main ATLAS subdetector system consists of the inner detector
 735 (ID), calorimeter systems (electromagnetic and hadronic) and the muon spectrometer (MS).
 736 The ATLAS detector uses a right-handed coordinate system [27] designed to align with
 737 the geometry of a collision interaction, with the origin set at the interaction point, the z -axis

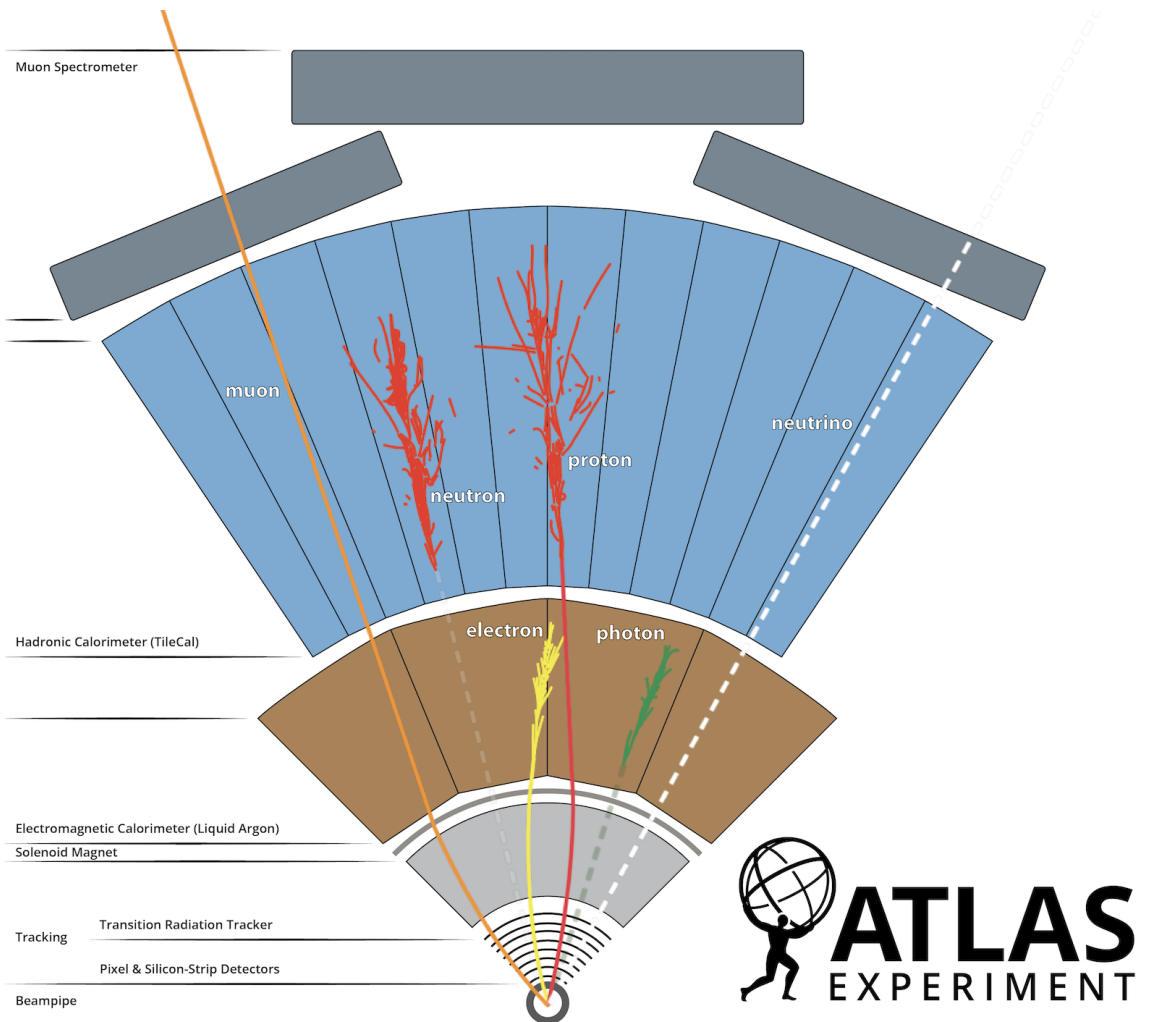


Figure 3.4: A cross section slice of the ATLAS detector showing different subsystems along with visualization of different types of particles traveling through the detector [91].

738 following (either of) the beamline and the x -axis pointing towards the center of the LHC
 739 ring. In cylindrical coordinates, the polar angle θ is measured from the beam axis, and
 740 the azimuthal angle ϕ is measured along the transverse plane (xy -plane) starting at the x -
 741 axis. Additional observables are defined for physics purposes: the pseudorapidity defined as
 742 $\eta = -\ln \tan(\theta/2)$; angular distance within the detector defined as $\Delta R = \sqrt{\Delta\eta^2 + \Delta\phi^2}$; and
 743 transverse momentum p_T (transverse energy E_T) defined as the component of the particle's
 744 momentum (energy) projected onto the transverse plane.

745 3.2.1 Inner detector

746 The innermost part of ATLAS is the inner detector (ID) [27], constructed primarily for
747 the purpose of measuring and reconstructing charged tracks within the $|\eta| < 2.5$ region with
748 high momentum resolution ($\sigma_{p_T}/p_T = 0.05\% \pm 1\%$). Figure 3.5 shows the composition of
749 the ID with three subsystems, the innermost being the pixel detector, then Semiconductor
750 Tracker (SCT), and the Transition Radiation Tracker (TRT) on the outermost layer; all of
751 which are surrounded by a solenoid magnet providing a magnetic field of 2 T.

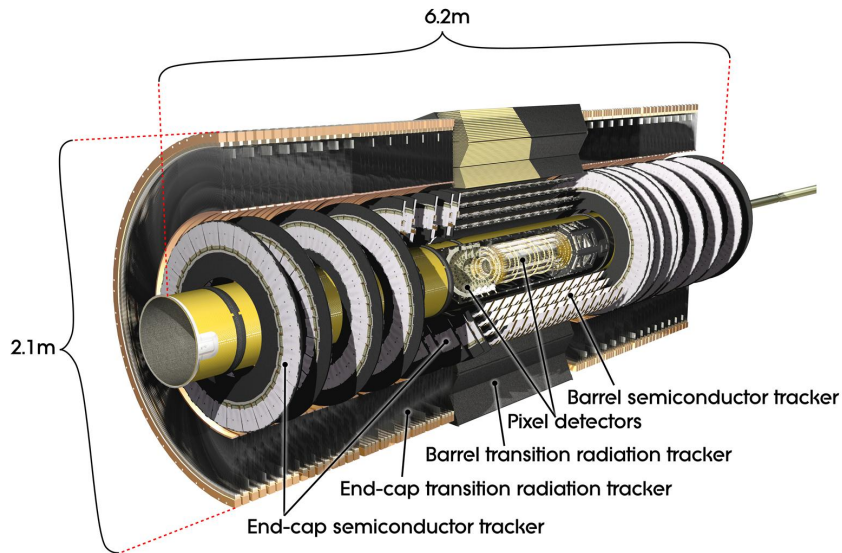


Figure 3.5: Cutaway illustration of the inner detector along with its subsystems [92].

752 Pixel detector

753 The pixel detector subsystem [27] consists of 250 μm silicon semiconductor pixel layers
754 with about 80.4 million readout channels, reaching a spatial resolution of 10 μm in the
755 $R - \phi$ (transverse) plane and 115 μm in the z -direction for charged tracks. Charged particles
756 passing through the pixel detector ionize the silicon layers and produce electron-hole pairs;

757 the electrons drift towards the detector's electrode under an applied electric field and the
758 resulting electric signals are collected in read-out regions. The pixel detector is used primarily
759 for impact parameter measurement, pile-up suppression, vertex finding and seeding for track
760 reconstruction.

761 Semiconductor Tracker

762 The Semiconductor Tracker (SCT) [27] functions similarly to the pixel detector, using
763 silicon semiconductor microstrips totaling about 6.3 million read-out channels, reaching a
764 per layer resolution of 17 μm in the $R\text{-}\phi$ plane and 580 μm in the z -direction [27]. The
765 SCT plays an important role in precise p_{T} measurement of charged particles as well as track
766 reconstruction.

767 Transition Radiation Tracker

768 The outermost layer of the ID, the Transition Radiation Tracker (TRT) [27], consists of
769 layers of 4 mm diameter straw tubes filled with a xenon-based gas mixture and a 30 μm
770 gold-plated wire in the center. The TRT contains a total of about 351 thousand readout
771 channels with a resolution of 130 μm for each straw tube in the $R\text{-}\phi$ plane, and provides
772 extended track measurement, particularly estimation of track curvature under the solenoidal
773 magnetic field. Importantly, the TRT also serves to identify electrons through absorption of
774 emitted transition-radiation within the Xe-based gas mixture.

775 3.2.2 Calorimeter systems

776 Surrounding the ID is the ATLAS calorimeter system [27] with electromagnetic (EM) and
777 hadronic calorimeters, covering a range of $|\eta| < 4.9$. The calorimeters are sampling calorime-

778 ters with alternating absorbing layers to stop incoming particles and active layers to collect
 779 read-out signals from energy deposits. Incoming particles passing through the calorimeters
 780 interact with the absorbing layers, producing EM or hadronic showers of secondary particles.
 781 The particle showers deposit energy in the corresponding layer of the calorimeters, which
 782 are collected and aggregated to identify and reconstruct the original particle's energy and
 783 direction. Figure 3.6 shows a schematic overview of the ATLAS calorimeter system.

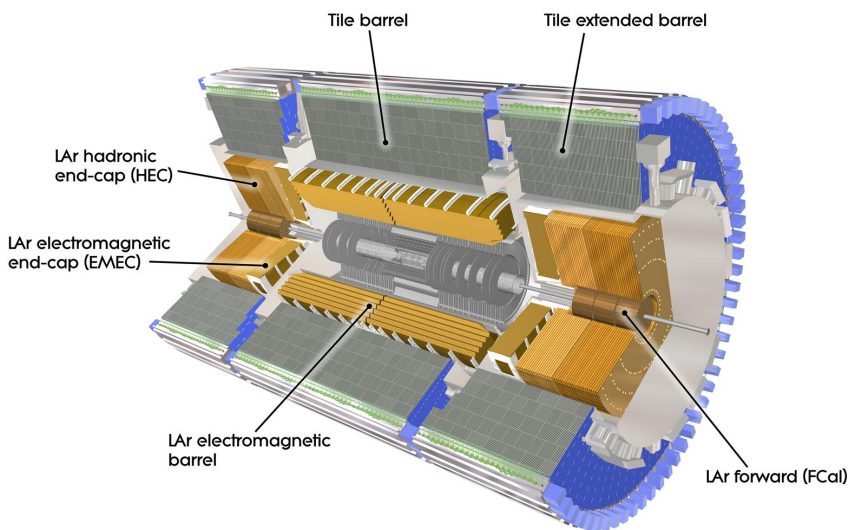


Figure 3.6: Cutaway illustration of the calorimeter system including the EM, hadronic and LAr forward calorimeters [93].

784 Electromagnetic calorimeter

785 The EM calorimeter [27] covers the innermost part of the calorimeter system, with lead
 786 (Pb) absorbing layers and liquid argon (LAr) active layers to capture the majority of electrons
 787 and photons exiting the ID. The EM calorimeter is divided into regions depending on η
 788 coverage: a barrel region ($|\eta| < 1.475$), two endcap regions ($1.375 < |\eta| < 3.2$) and a
 789 transition region ($1.372 < |\eta| < 1.52$). The endcap calorimeters are further divided into an

790 outer wheel region ($1.372 < |\eta| < 2.5$) and an inner wheel region ($2.5 < |\eta| < 3.2$) in order
791 to provide precise coverage within the same η range as the ID. Overlap between the barrel
792 and endcap regions compensates for the lower material density in the transition region.

793 **Hadronic calorimeter**

794 The hadronic calorimeter [27] covers up to $|\eta| < 4.9$ and is comprised of three parts: the
795 tile calorimeter with a barrel region ($|\eta| < 1.0$) and extended barrel regions ($0.8 < |\eta| < 1.7$);
796 the hadronic endcap calorimeter (HEC) covering $1.5 < |\eta| < 3.2$; and the forward calorimeter
797 (FCal) covering $3.2 < |\eta| < 4.9$. The tile calorimeter covers the EM calorimeter barrel region
798 and uses steel as material for the absorbing layers with scintillating tiles for the active layers.
799 Signals captured by scintillating tiles are read out from both sides using photomultiplier
800 tubes. The HEC calorimeter covers the endcap regions of the EM calorimeter and uses a
801 copper-LAr calorimeter layer scheme. The FCal is located close to the beamline providing
802 coverage for particles traveling close to parallel with the beam axis. The subdetector contains
803 three modules: one with copper absorbing layers optimized for EM measurements, and two
804 with tungsten absorbing layers targeting hadronic cascades. All modules in the FCal use
805 LAr as the active layer.

806 **3.2.3 Muon spectrometer**

807 Generally, the only particles that penetrate past the calorimeter layer are muons and
808 neutrinos. The muon spectrometer (MS) [27] is situated on the outermost of the ATLAS
809 detector and aims to track and measure muons within $|\eta| < 2.7$. The MS utilizes an array of
810 toroid magnets to provide a magnetic field perpendicular to the muon trajectory, bending
811 the track in order to measure its curvature. The magnetic field is powered by a large barrel

812 toroid ($|\eta| < 1.4$) with strength of 0.5 T and two endcap toroid magnets ($1.6 < |\eta| < 2.7$) of
813 1 T. Both types contribute to the magnetic field in the transition region ($1.4 < |\eta| < 1.6$).

814 To measure the muon itself, four types of large gas-filled chambers known as muon cham-
815 bers [27] are designed and constructed for two main goals: triggering on potential muon
816 candidates entering the MS and tracking their trajectories through the detector with high
817 precision. The tracking system include Monitored Drift Tubes (MDTs), which record muon
818 track information over the entire MS η range ($|\eta| < 2.7$). The MDTs are built with multi-
819 ple layers of drift tubes and filled with a mixture of 93% Ar and 7% CO₂. Muons passing
820 through drift tubes in the MDT ionize the gas within each tube; signals are then recorded
821 as freed electrons drift to read-out channels under an applied electric field. In the forward
822 region ($2.0 < |\eta| < 2.7$), Cathode Strip Chambers (CSCs) are included along with MDTs.
823 The CSCs are multiwire proportional chambers built with higher granularity and shorter
824 drift time than the MDTs to handle tracking in an environment with high background rates

825 .

826 The MS trigger system includes Resistive Plate Chambers (RPCs) [27], which provide
827 triggering in the barrel region ($|\eta| < 1.05$) using parallel electrode plates made of resistive
828 materials with a gas mixture inbetween. High voltage is applied to the plates, accelerat-
829 ing the electrons freed from ionized gas and creating a fast avalanche of charge, which is
830 collected on external read-out strips almost instantaneously. Triggering and coarse position
831 measurements in the endcap region ($1.05 < |\eta| < 2.5$) is handled by Thin-Gap Chambers
832 (TGCs). Similar to CSCs, TGCs are multiwire proportional chambers with a small wire gap
833 ("thin-gap") and high applied voltage across the gap, resulting in fast response time giving
834 TGCs the capabilities to identify muon candidates in real time.

835 **3.2.4 Trigger & data acquisition**

836 The LHC produces a colossal amount of collision data at a bunch crossing rate of 40 MHz
837 with bunch spacing of 25 ns. The ATLAS Trigger and Data Acquisition (TDAQ) system [94]
838 synchronously identifies and records interesting events for in-depth analysis. The ATLAS
839 trigger system in Run 2 consists of two steps: Level-1 (L1) trigger and High-Level Trigger
840 (HLT). Events failing any step in the trigger chain are permanently lost.

841 The L1 trigger hardware is divided into L1 calorimeter triggers (L1Calo) and L1 muon
842 triggers (L1Muon) [94]. L1Calo trigger uses information from ATLAS calorimeter system
843 to quickly identify signs of high p_T objects e.g. EM clusters, jets and missing transverse
844 energy E_T^{miss} (section 4.4). Similarly, L1Muon uses information from the RPCs and TGCs
845 of the MS to make quick decisions on potentially interesting muon candidates. Outputs
846 from L1Calo and L1Muon are fed into the L1 topological trigger (L1Topo) for additional
847 filtering based on event topology and multi-object correlation, allowing for more selective
848 and physics-motivated triggering. Decisions from all three types of L1 triggers are provided
849 as inputs for the Central Trigger Processor (CTP) for a final Level-1 Accept (L1A) decision.

850 The entire L1 trigger chain results in a 2.5 μs latency and reduces the event rate to 100 kHz.

851 Events passing L1 triggers are sent to HLTs before being saved to offline storage at
852 CERN data centers. HLTs are software-based triggers used for more complex and specific
853 selections on physics objects required by targeted analysis goals, in turn requiring more
854 computing power with longer latency. After HLT selections, the event rate is reduced to 1
855 kHz on average [94]. Overall, the full trigger chain reduces the event rate for ATLAS by
856 approximately a factor of 4×10^4 .

857 **Chapter 4. Particle Reconstruction & Identifi-**
858 **fication**

859 Activity within the ATLAS detector is recorded as raw electronic signals, which can
860 be utilized by ATLAS reconstruction software to derive physics objects for analysis. This
861 chapter describes the reconstruction and identification of basic objects (e.g. interaction
862 vertices, tracks, topological clusters of energy deposits) and subsequently of complex physics
863 objects i.e. particles and particle signatures.

864 **4.1 Primary reconstruction**

865 **4.1.1 Tracks**

866 Charged particles traveling through the ATLAS detector deposit energy in different layers
867 of the ID and MS. The ID track reconstruction software consists of two algorithm chains:
868 inside-out and outside-in track reconstruction [95–97].

869 The inside-out algorithm is primarily used for the reconstruction of primary particles
870 i.e. particles directly produced from pp collisions or decay products of short-lived particles.
871 The process starts by forming space points from seeded hits in the silicon detectors within
872 the pixel & SCT detectors. Hits further away from the interaction vertex are added to
873 the track candidate using a combinatorial Kalman filter [98] pattern recognition algorithm.
874 Track candidates are then fitted with a χ^2 filter [99] and loosely matched to a fixed-sized
875 EM cluster. Successfully matched track candidates are re-fitted with a Gaussian-sum filter
876 (GSF) [100], followed by a track scoring strategy to resolve fake tracks & hit ambiguity

877 between different tracks [101]. The track candidate is then extended to the TRT to form
878 final tracks satisfying $p_T > 400$ MeV. The outside-in algorithm handles secondary tracks
879 mainly produced from long-lives particles or decays of primary particles by back-tracking
880 from TRT segments, which are then extended inward to match silicon hits in the pixel and
881 SCT detectors to form track reconstruction objects.

882 4.1.2 Vertices

883 Vertices represent the point of interaction or decay for particles within the ATLAS de-
884 tector. Primary vertices (PVs) are defined as the point of collision for hard-scattering pp
885 interactions, while secondary or displaced vertices result from particle decays occurring at a
886 distance from its production point.

887 Reconstruction of PVs is crucial to accurately profile the kinematic information of an
888 event and form a basis for subsequent reconstruction procedures. Primary vertex recon-
889 struction occurs in two stages: vertex finding and vertex fitting [102]. The vertex finding
890 algorithm uses the spatial coordinates of reconstructed tracks to form the seed for a vertex
891 candidate. An adaptive vertex fitting algorithm [103] then iteratively evaluates track-vertex
892 compatibility to estimate a new best vertex position. Less compatible tracks are down-
893 weighted in each subsequent iteration, and incompatible tracks are removed and can be
894 used for another vertex seed; the process is repeated until no further PV can be found.
895 All reconstructed vertices without at least two matched tracks are considered invalid and
896 discarded.

897 Secondary vertex reconstruction uses the Secondary Vertex Finder (SVF) algorithm [104]
898 which is primarily designed to reconstruct b - and c -hadrons for flavor tagging purposes. The
899 SVF aims to reconstruct one secondary vertex per jet and only considers tracks that are

900 matched to a two-track vertex and contained within a p_T -dependent cone around the jet
901 axis. The tracks are then used to reconstruct a secondary vertex candidate using an iterative
902 process similar to the PV vertex fitting procedure.

903 **Pile-up**

904 At high luminosities, multiple interactions can be associated with one bunch crossing,
905 resulting in many PVs. The effect is called pile-up [105], and usually result from soft QCD
906 interactions. Pile-up can be categorized into two types: in-time pile-up, stemming from
907 additional pp collisions in the same bunch crossing that is not the hard-scatter process; out-
908 of-time pile-up, resulting from leftover energy deposits in the calorimeters from other bunch
909 crossings.

910 **4.1.3 Topological clusters**

911 Topological clusters (topo-clusters) [106] consist of clusters of spatially related calorimeter
912 cell signals. Topo-clusters are primarily used to reconstruct hadron- and jet-related objects
913 in an effort to extract signal while minimizing electronic effects and physical fluctuations, and
914 also allow for recovery of energy lost through bremsstrahlung or photon conversions. Cells
915 with signal-to-noise ratio $\zeta_{\text{cell}}^{\text{EM}}$ passing a primary seed threshold are seeded into a dynamic
916 topological cell clustering algorithm as part of a proto-cluster. Neighboring cells satisfying a
917 cluster growth threshold are collected into the proto-cluster. If a cell is matched to two proto-
918 clusters, the clusters are merged. Two or more local signal maxima in a cluster satisfying
919 $E_{\text{cell}}^{\text{EM}} > 500 \text{ MeV}$ suggest the presence of multiple particles in close proximity, and the cluster
920 is split accordingly to maintain good resolution of the energy flow. The process continues
921 iteratively until all cells with $\zeta_{\text{cell}}^{\text{EM}}$ above a principal cell filter level have been matched to a

922 cluster.

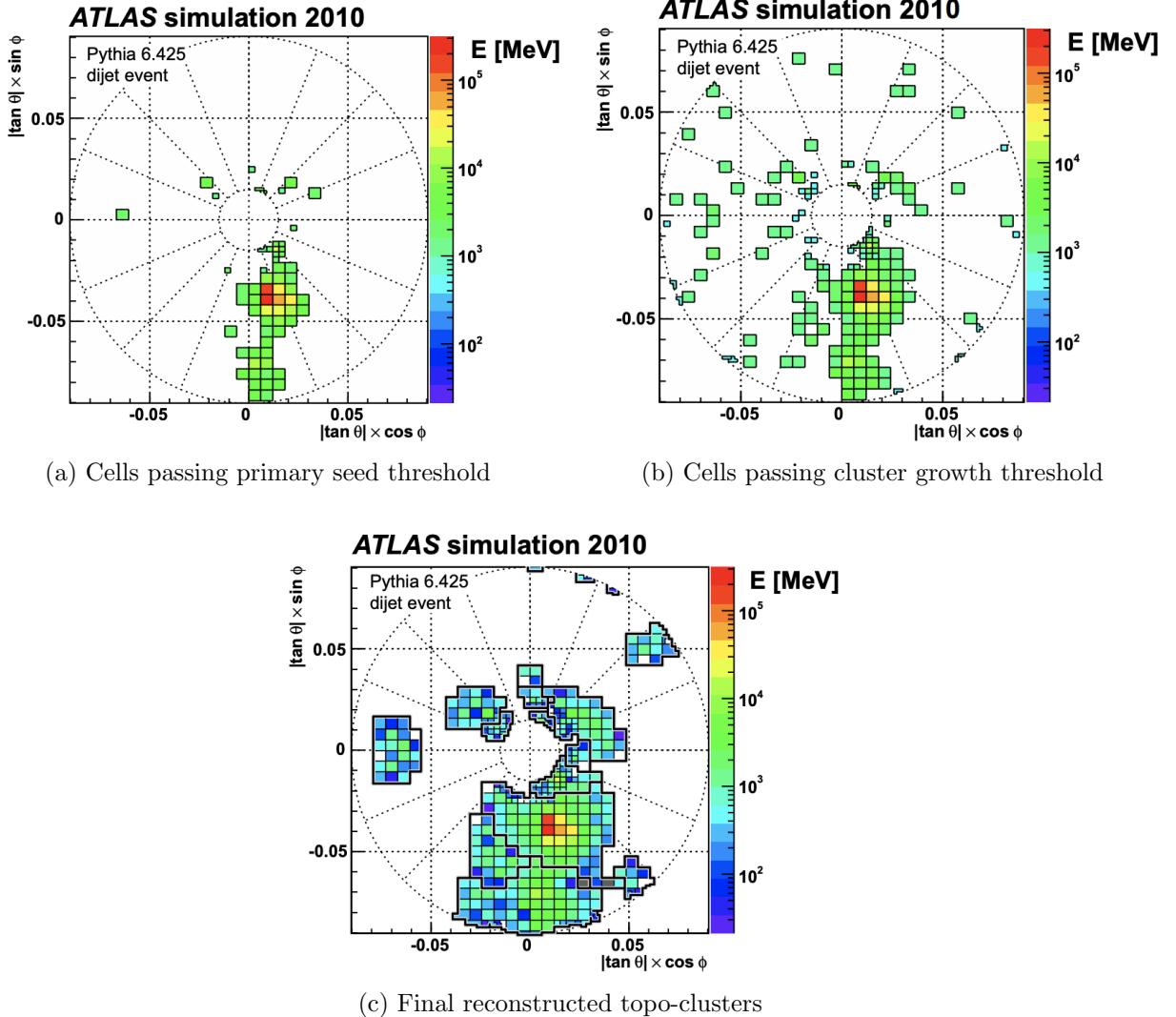


Figure 4.1: Stages of topo-cluster formation corresponding to each threshold. In (a), proto-clusters are seeded from cells with adequate signal significance $\zeta_{\text{cell}}^{\text{EM}}$. The clusters are further merged and split in (b) following a predefined cluster growth threshold. The process stops in (c) when all sufficiently significant signal hits have been matched to a cluster [106].

923 4.2 Jets

924 Quarks, gluons and other hadrons with non-neutral color charge cannot be observed
925 individually due to QCD color confinement, which forces a non-color-neutral hadron to

926 almost immediately undergo hadronization, producing a collimated cone of color-neutral
927 hadrons defined as a jet. Jet signals can be used to reconstruct and indirectly observe the
928 quarks or gluons from which the jet originated in the original hard-scattering process.

929 4.2.1 Jet reconstruction

930 The ATLAS jet reconstruction pipeline is largely carried out using a particle flow (PFlow)
931 algorithm combined with an anti- k_t jet clustering algorithm. The PFlow algorithm [107]
932 utilizes topo-clusters along with information from both the calorimeter systems and the ID in
933 order to make use of the tracker system’s advantages in low-energy momentum resolution and
934 angular resolution. First, the energy from charged particles is removed from the calorimeter
935 topo-clusters; then, it is replaced by particle objects created using the remaining energy in
936 the calorimeter and tracks matched to topo-clusters. The ensemble of ”particle flow objects”
937 and corresponding matched tracks are used as inputs for the iterative anti- k_t algorithm [108].

938 The main components of the anti- k_t algorithm involve the distance d_{ij} between two
939 jet candidates i and j , and the distance d_{iB} between the harder jet candidate of the two
940 (defined as i) and the beamline B . If $d_{ij} < d_{iB}$, then the two jet candidates are combined
941 and returned to the pool of candidates; otherwise, jet candidate i is considered a jet and
942 removed from the pool. The distance d_{ij} is inversely proportional to a predefined radius
943 parameter ΔR in order to control reconstruction quality for small- R and large- R jets. This
944 analysis uses $\Delta R = 0.4$ to better handle heavily collimated small- R jets resulting from parton
945 showers.

946 The anti- k_t jets so far have only been reconstructed at the EM level and need to be
947 calibrated to match the energy scale of jets reconstructed at particle level. This is done
948 via a MC-based jet energy scale (JES) calibration sequence, along with further calibrations

949 to account for pile-up effects and energy leakage. The full JES calibration sequence is
 950 shown in Figure 4.2. All calibrations except origin correction are applied to the jet's four-
 951 momentum i.e. jet p_T , energy and mass. Afterwards, a jet energy resolution (JER) [109]
 952 calibration step is carried out in a similar manner to JES to match the resolution of jets in
 953 dijet events. To further suppress pile-up effects, a neural-network based jet vertex tagger
 954 (NNJvt) discriminant was developed based on the previous jet vertex tagger (JVT) algorithm
 955 [105] and applied to low- p_T reconstructed jets.

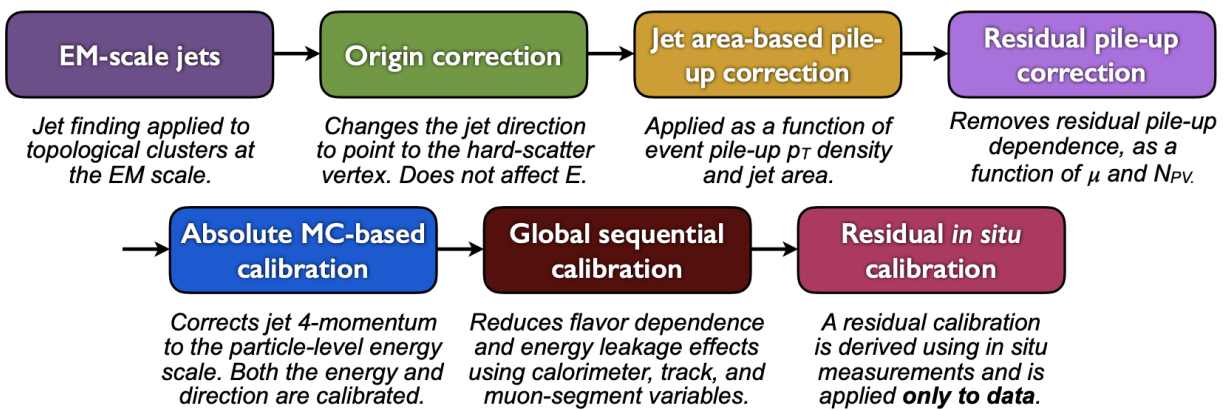


Figure 4.2: Jet energy scale calibration sequence for EM-scale jets [110].

956 4.2.2 Flavor tagging

957 Identifying and classifying hadronic jets are important tasks for ATLAS physics, for
 958 example analyses involving Higgs decays $H \rightarrow b\bar{b}$ or top quarks. Flavor tagging or b -tagging
 959 is the process of identifying jets containing b -hadrons, c -hadrons, light-hadrons (uds -hadrons)
 960 or jets from hadronically decaying τ leptons. Distinguishing b -jets is possible due to their
 961 characteristically long lifetime ($\tau \approx 1.5$ ps), displaced secondary decay vertex and high decay
 962 multiplicity.

963 Usage of b -tagging in this analysis is done via five operating points (OPs), corresponding

964 to 65%, 70%, 77%, 85% and 90% b -jet tagging efficiency ε_b in simulated $t\bar{t}$ events, in order
965 from the tightest to loosest discriminant cut point. The OPs are defined by placing selections
966 on the tagger output to provide a predefined ε_b level; the selection cuts act as a variable
967 trade-off between b -tagging efficiency and b -jet purity i.e. c - or light-jet rejection. For this
968 analysis, a jet is considered b -tagged if it passes the 85% OP. The b -tagged jet is then
969 assigned a pseudo-continuous b -tagging (PCBT) score, which quantifies a jet's ability to
970 satisfy different OPs. The score can take integer values between 1 and 6, where a score of 6
971 is assigned to jets passing all OP thresholds; a score of 2 for jets that pass only the tightest
972 OP (90%); and a score of 1 for jets that pass no OP. A value of -1 is also defined for any jet
973 that does not satisfy b -tagging criteria. Since the targeted $t\bar{t}t\bar{t}$ final states contain at least
974 four b -hadrons from top and W decays, a b -tagging OP of 85% is used to maintain high
975 purity during b -tagged jet selections in the signal region.

976 **GN2 b -tagging algorithm**

977 For this analysis, b -jets are identified and tagged with the GN2v01 b -tagger [111]. The
978 GN2 algorithm uses a Transformer-based model [112] modified to incorporate domain knowl-
979 edge and additional auxiliary physics objectives: grouping tracks with a common vertex and
980 predicting the underlying physics process for a track. The network structure is shown in
981 Figure 4.3. The GN2 b -tagger form the input vector by concatenating 2 jet variables and
982 19 track reconstruction variables (for up to 40 tracks), normalized to zero mean and unit
983 variance. The output consists of a track-pairing output layer of size 2, a track origin clas-
984 sification layer of 7 categories, and a jet classification layer of size 4 for the probability of
985 each jet being a b -, c -, light- or τ -jet respectively. For b -tagging purpose, a discriminant is

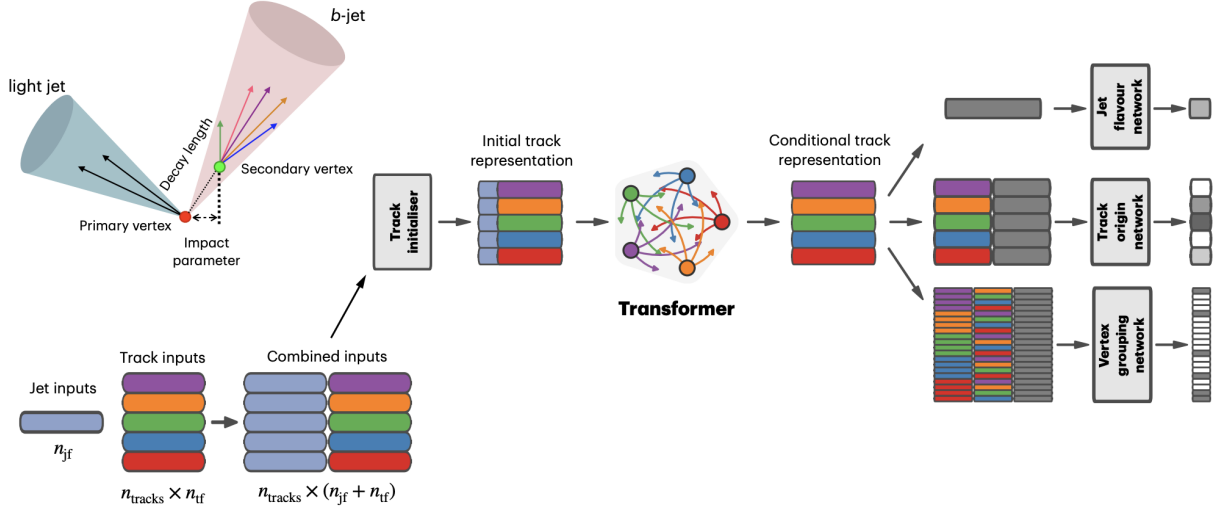


Figure 4.3: Overview of the GN2 architecture. The number of jet and track features are represented by n_{jf} and n_{tf} respectively. The global jet representation and track embeddings output by the Transformer encoder are used as inputs for three task-specific networks [111].

986 defined using these four outputs

$$D_b = \ln \left(\frac{p_b}{f_c p_c + f_\tau p_\tau + (1 - f_c - f_\tau)p_{\text{light}}} \right) \quad (4.1)$$

987 where p_x is the probability of the jet being an x -jet as predicted by GN2, and f_c , f_τ are tun-
 988 able free parameters controlling balance between c - and light-jet rejection. Simulated SM $t\bar{t}$
 989 and BSM Z' events from pp collisions were used as training and evaluation samples. In order
 990 to minimize bias, both b - and light-jet samples are re-sampled to match c -jet distributions.
 991 Figure 4.4 shows the performance of GN2 compared to the previous convolutional neural
 992 network-based standard b -tagging algorithm DL1d, in terms of c -, light- and τ -jet rejection
 993 as a function of b -tagging efficiency. The network gives a factor of 1.5-4 improvement in
 994 experimental applications compared to DL1d [111], without dependence on the choice of
 995 MC event generator or inputs from low-level flavor tagging algorithm.

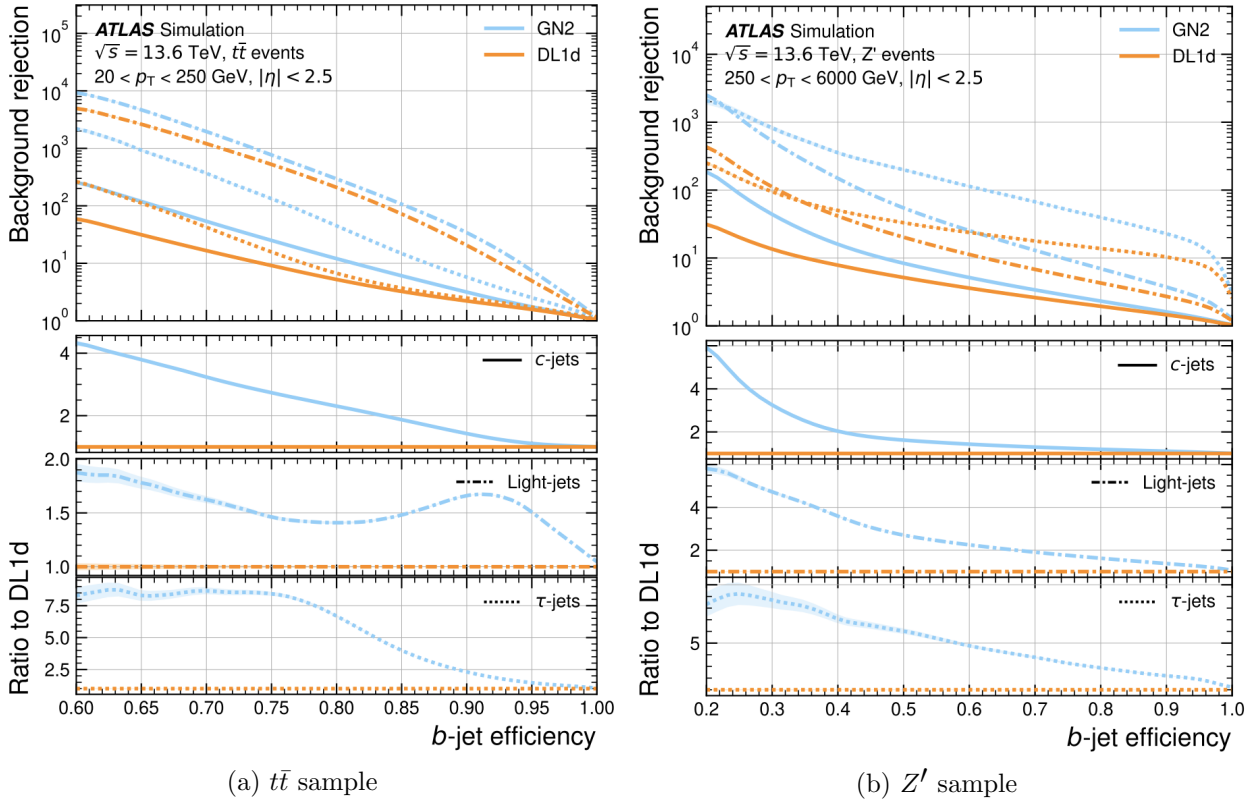


Figure 4.4: The c -, light- and τ -jet rejection rate as a function of b -tagging efficiency for GN2 and DL1d using (a) jets in the $t\bar{t}$ sample, and (b) jets in the Z' sample. The performance ratios of GN2 to DL1d are shown in the bottom panels [111].

996 Efficiency calibration

997 Due to imperfect description of detector response and physics modeling effects in simu-
 998 lation, the b -tagging efficiency predicted by MC simulation $\varepsilon_b^{\text{sim}}$ requires a correction factor
 999 to match the efficiency measured in collision data $\varepsilon_b^{\text{data}}$. The correction scale factors (SFs)
 1000 are defined as $\text{SF} = \varepsilon_b^{\text{data}} / \varepsilon_b^{\text{sim}}$ and are determined by data-to-MC calibration using samples
 1001 enriched in dileptonic $t\bar{t}$ decays [113]. The resulting SFs are applied to MC simulated jets
 1002 individually.

1003 4.3 Leptons

1004 Lepton reconstruction in ATLAS involves electron and muon reconstruction since tau
1005 decays quickly, and depending on decay mode can be reconstructed using either jets or light
1006 leptons. From here on out within this dissertation, leptons will be used exclusively to refer to
1007 electrons and muons. Leptons can be classified into two categories: prompt leptons resulting
1008 from heavy particle decays and non-prompt leptons resulting from detector or reconstruction
1009 effects, or from heavy-flavor hadron decays.

1010 4.3.1 Electrons

1011 Electrons leave energy signature in the detector by interacting with the detector materials
1012 and losing energy in the form of bremsstrahlung photons. A bremsstrahlung photon can
1013 produce an electron-positron pair which can itself deposit signals in the detector, creating a
1014 cascade of particles that can leave multiple of either tracks in the ID or EM showers in the
1015 calorimeters, all of which are considered part of the same EM topo-cluster. Electron signal
1016 signature has three characteristic components: localized energy deposits in the calorimeters,
1017 multiple tracks in the ID and compatibility between the above tracks and energy clusters in
1018 the $\eta \times \phi$ plane [114]. Electron reconstruction in ATLAS follows these steps accordingly.

1019 Seed-cluster reconstruction and track reconstruction are performed sequentially in ac-
1020 cordance with the iterative topo-clustering algorithm and track reconstruction method de-
1021 scribed in section 4.1. The seed-cluster and GSF-refitted track candidate not associated
1022 with a conversion vertex are matched to form an electron candidate. The cluster energy is
1023 then calibrated using multivariate techniques on data and simulation to match the original
1024 electron energy.

1025 **Electron identification**

1026 Additional LH-based identification selections using ID and EM calorimeter information
1027 are implemented to further improve the purity of reconstructed electrons in the $|\eta| < 2.47$ re-
1028 gion of the detector [114]. The electron LH function is built with the signal being prompt elec-
1029 trons and background being objects with similar signature to prompt electrons i.e. hadronic
1030 jet deposits, photon conversions or heavy-flavor hadron decays. Three identification OPs
1031 are defined for physics analyses: *Loose*, *Medium* and *Tight*, optimized for 9 bins in $|\eta|$ and
1032 12 bins in E_T with each OP corresponding to a fixed efficiency requirement for each bin.
1033 For typical EW processes, the target efficiencies for *Loose*, *Medium* and *Tight* start at 93%,
1034 88% and 80% respectively and increase with E_T . Similar to b -tagging OPs, the electron
1035 identification OPs represent a trade-off in signal efficiency and background rejection. The
1036 electron efficiency are estimated using tag-and-probe method on samples of $J/\Psi \rightarrow ee$ and
1037 $Z \rightarrow ee$ [114]. The *Tight* electron identification OP is used for this analysis.

1038 **Electron isolation**

1039 A characteristic distinction between prompt electrons and electrons from background
1040 processes is the relative lack of activity in both the ID and calorimeters within an $\Delta\eta \times \Delta\phi$
1041 area surrounding the reconstruction candidate. Calorimeter-based and track-based electron
1042 isolation variables [114] are defined to quantify the amount of activity around the electron
1043 candidate using topo-clusters and reconstructed tracks respectively.

1044 Calorimeter-based isolation variables $E_T^{\text{cone}XX}$ are computed by first summing the energy
1045 of topo-clusters with barycenters falling within a cone of radius $\Delta R = \sqrt{(\Delta\eta)^2 + (\Delta\phi)^2} =$
1046 $XX/100$ around the direction of the electron candidate. The final isolation variables are

obtained by subtracting from the sum the energy belonging to the candidate electron at the core of the cone, then applying corrections for pile-up effects and energy leakage outside of the core. Similar to calorimeter-based variables, track-based isolation variables $p_T^{\text{varcone}XX}$ are calculated by summing all track p_T within a cone of radius ΔR around the electron candidate, minus the candidate's contribution. The cone radius is variable as a function of p_T and is described as

$$\Delta R \equiv \min \left(\frac{10}{p_T}, \Delta R_{\max} \right), \quad (4.2)$$

where p_T is expressed in GeV and ΔR_{\max} is the maximum cone size, defined to account for closer proximity of decay products to the electron in high-momentum heavy particle decays. Four isolation operating points are implemented to satisfy specific needs by physics analyses: *Loose*, *Tight*, *HighPtCaloOnly* and *Gradient* [114]. For this analysis, electrons isolation uses *Tight* requirements.

1058 Electron charge misidentification

Charge misidentification is a crucial irreducible background, particularly for analyses with electron charge selection criteria. Electron charge is determined by the curvature of the associated reconstructed track, and misidentification of charge can occur via either an incorrect curvature measurement or an incorrectly matched track. Inaccurate measurement is more likely for high energy electrons due to the small curvature in track trajectories at high p_T , while track matching error usually results from bremsstrahlung pair-production generating secondary tracks in close proximity [114]. Suppression of charge misidentification background in Run 2 is additionally assisted by a boosted decision tree discriminant known

1067 as the Electron Charge ID Selector (ECIDS). For this analysis, all electrons are required to
1068 pass the ECIDS criterion.

1069 **4.3.2 Muons**

1070 Muons act as minimum-ionizing particles, leaving tracks in the MS or characteristics
1071 energy deposits in the calorimeter and can be reconstructed globally using information from
1072 the ID, MS and calorimeters. Five reconstruction strategies corresponding to five muon
1073 types [116] are utilized in ATLAS:

- Combined (CB): the primary ATLAS muon reconstruction method. Combined muons
1074 are first reconstructed using MS tracks then extrapolated to include ID tracks (outside-in strategy). A global combined track fit is performed on both MS and ID tracks.
- Inside-out combined (IO): complementary to CB reconstruction. IO muon tracks are
1075 extrapolated from ID to MS, then fitted with MS hits and calorimeter energy loss in a
1076 combined track fit.
- MS extrapolated (ME): ME muons are defined as muons with a MS track that cannot
1077 be matched to an ID track using CB reconstruction. ME muons allow extension of
1078 muon reconstruction acceptance to regions not covered by the ID ($2.5 < |\eta| < 2.7$)
- Segment-tagged (ST): ST muons are defined as a successfully matched ID track that
1079 satisfies tight angular matching criteria to at least one reconstructed MDT or CSC
1080 segment when extrapolated to the MS. MS reconstruction is used primarily when
1081 muons only crossed one layer of MS chambers.
- Calorimeter-tagged (CT): CT muons are defined as an ID track that can be matched to
1082 1083 1084 1085 1086 1087

1088 energy deposits consistent with those of a minimum-ionizing particle when extrapolated
1089 through the calorimeter. CT reconstruction extends acceptance range to regions in the
1090 MS with sparse instrumentation ($|\eta| < 0.1$) with a higher p_T threshold of 5 GeV,
1091 compared to the 2 GeV threshold used by other muon reconstruction algorithms due
1092 to large background contamination at the low p_T range of $15 < p_T < 100$ GeV [117].

1093 Muon identification

1094 Reconstructed muons are further filtered by identification criteria to select for high-
1095 quality prompt muons. Requirements include number of hits in the MS and ID, track fit
1096 properties and compatibility between measurements of the two systems. Three standard
1097 OPs (*Loose*, *Medium*, *Tight*) are defined to better match the needs of different physics
1098 analyses concerning prompt muon p_T resolution, identification efficiency and non-prompt
1099 muon rejection. The default identification OP for ATLAS physics and also the OP used in
1100 this analysis is *Medium*, which provides efficiency and purity suitable for a wide range of
1101 studies while minimizing systematic uncertainties [116].

1102 Muon isolation

1103 Muons from heavy particle decays are often produced in an isolated manner compared to
1104 muons from semileptonic decays, and is therefore an important tool for background rejection
1105 in many physics analyses. Muon isolation strategies are similar to that of electron in section
1106 4.3.1, with track-based and calorimeter-based isolation variables. Seven isolation OPs are
1107 defined using either or both types of isolation variables, balancing between prompt muon
1108 acceptance and non-prompt muon rejection. The full definition and description for the muon
1109 isolation OPs are detailed in Ref. [116].

1110 4.4 Missing transverse momentum

1111 Collisions at the LHC happen along the z -axis of the ATLAS coordination system between
 1112 two particle beam of equal center-of-mass energy. By conservation of momentum, the sum of
 1113 transverse momenta of outgoing particles should be zero. A discrepancy between measured
 1114 momentum and zero would then suggest the presence of undetectable particles, which would
 1115 consist of either SM neutrinos or some unknown BSM particles, making missing transverse
 1116 momentum (E_T^{miss}) an important observable to reconstruct.

1117 Reconstructing E_T^{miss} utilizes information from fully reconstructed leptons, photons, jets
 1118 and other matched track-vertex objects not associated with a prompt object (soft signals),
 1119 defined with respect to the $x(y)$ -axis as

$$E_{x(y)}^{\text{miss}} = - \sum_{i \in \{\text{hard objects}\}} p_{x(y),i} - \sum_{j \in \{\text{soft signals}\}} p_{x(y),j}, \quad (4.3)$$

1120 where $p_{x(y)}$ is the $x(y)$ -component of p_T for each particle [118]. The following observables
 1121 can then be defined:

$$\begin{aligned} \mathbf{E}_T^{\text{miss}} &= (E_x^{\text{miss}}, E_y^{\text{miss}}), \\ E_T^{\text{miss}} &= |\mathbf{E}_T^{\text{miss}}| = \sqrt{(E_x^{\text{miss}})^2 + (E_y^{\text{miss}})^2}, \\ \phi^{\text{miss}} &= \tan^{-1}(E_y^{\text{miss}}/E_x^{\text{miss}}), \end{aligned} \quad (4.4)$$

1122 where E_T^{miss} represents the magnitude of the missing transverse energy vector $\mathbf{E}_T^{\text{miss}}$, and
 1123 ϕ^{miss} its direction in the transverse plane. The vectorial sum $\mathbf{E}_T^{\text{miss}}$ can be broken down into

$$\mathbf{E}_T^{\text{miss}} = - \underbrace{\sum_{\text{selected electrons}} \mathbf{p}_T^e - \sum_{\text{selected muons}} \mathbf{p}_T^\mu - \sum_{\text{accepted photons}} \mathbf{p}_T^\gamma - \sum_{\text{accepted } \tau\text{-leptons}} \mathbf{p}_T^\tau}_{\text{hard term}} - \underbrace{\sum_{\text{accepted jets}} \mathbf{p}_T^{\text{jet}} - \sum_{\text{unused tracks}} \mathbf{p}_T^{\text{track}}}_{\text{soft term}}. \quad (4.5)$$

1124 Two OPs are defined for E_T^{miss} , *Loose* and *Tight*, with selections on jet p_T and JVT criteria
 1125 [119]. The *Tight* OP is used in this analysis; *Tight* reduces pile-up dependence of E_T^{miss}
 1126 by removing the phase space region containing more pile-up than hard-scatter jets, at the
 1127 expense of resolution and scale at low pile-up,

1128 4.5 Overlap removal

1129 Since different objects are reconstructed independently, it is possible for the same de-
 1130 tector signals to be used to reconstruct multiple objects. An overlap removal strategy is
 1131 implemented to resolve ambiguities; the overlap removal process for this analysis applies
 1132 selections in Table 4.1 sequentially, from top to bottom.

Table 4.1: Overlap removal process for this analysis, applied sequentially from top to bottom.

Remove	Keep	Matching criteria
Electron	Electron	Shared ID track, $p_{T,1}^e < p_{T,2}^e$
Muon	Electron	Shared ID track, CT muon
Electron	Muon	Shared ID track
Jet	Electron	$\Delta R < 0.2$
Electron	Jet	$\Delta R < 0.4$
Jet	Muon	($\Delta R < 0.2$ or ghost-associated) & $N_{\text{track}} < 3$
Muon	Jet	$\Delta R < \min(0.4, 0.04 + 10\text{GeV}/p_T^\mu)$

1133 4.6 Object definition

1134 Table 4.2 summarizes the selections on physics objects used in this analysis. Each se-
1135 lection comes with associated calibration scale factors (SFs) to account for discrepancies
1136 between data and MC simulation, and are applied multiplicatively to MC event weights.

Table 4.2: Summary of object selection criteria used in this analysis. ℓ_0 refers to the leading lepton in the event.

Selection	Electrons	Muons	Jets
p_T [GeV]	> 15 $p_T(\ell_0) > 28$	> 15	> 20
$ \eta $	$1.52 \leq \eta < 2.47$ < 1.37	< 2.5	< 2.5
Identification	<i>TightLH</i> pass ECIDS ($ee/e\mu$)	<i>Medium</i>	NNJvt <i>FixedEffPt</i> ($p_T < 60$, $ \eta < 2.4$)
Isolation	<i>Tight_VarRad</i>	<i>PflowTight_VarRad</i>	
Track-vertex assoc.			
$ d_0^{\text{BL}}(\sigma) $	< 5	< 3	
$ \Delta z_0^{\text{BL}} \sin \theta $ [mm]	< 0.5	< 0.5	

1137 Chapter 5. Data & Simulated Samples

1138 5.1 Data samples

1139 Data samples used in this analysis were collected by the ATLAS detector during Run
1140 2 data-taking campaign between 2015-2018. The samples contain pp collisions at center-of-
1141 mass energy of $\sqrt{s} = 13$ TeV with 25 ns bunch-spacing, which corresponds to an integrated
1142 luminosity of 140 fb^{-1} with an uncertainty of 0.83% [87]. The HLT trigger strategy is similar
1143 to that of previous $t\bar{t}t\bar{t}$ observation analysis [44] and include single lepton and dilepton
1144 triggers. Calibration for di-muon and electron-muon triggers were not ready for the samples
1145 used in this analysis, and are therefore not included. Events are also required to contain at
1146 least one lepton matched to the corresponding object firing the trigger. Triggers used are
1147 summarized in Table 5.1.

1148 5.2 Monte Carlo samples

1149 Monte Carlo simulated samples are used to estimate signal acceptance before unblinding,
1150 profile the physics background for the analysis and to study object optimizations. Simulated
1151 samples for this analysis use are generated from ATLAS generalized MC20a/d/e samples for
1152 Run 2, using full detector simulation (FS) and fast simulation (AF3) to simulate detector
1153 response. MC samples used and simulation processes are summarized in Table 5.2.

Table 5.1: Summary of all HLT triggers used in this analysis. Events are required to pass at least one trigger.

Trigger	Data period			
	2015	2016	2017	2018
Single electron triggers				
HLT_e24_lhmedium_L1EM20VH	✓	-	-	-
HLT_e60_lhmedium	✓	-	-	-
HLT_e120_lhloose	✓	-	-	-
HLT_e26_lhtight_nod0_ivarloose	-	✓	✓	✓
HLT_e60_lhmedium_nod0	-	✓	✓	✓
HLT_e140_lhloose_nod0	-	✓	✓	✓
Di-electron triggers				
HLT_2e12_lhloose_L12EM10VH	✓	-	-	-
HLT_2e17_lhvloose_nod0	-	✓	-	-
HLT_2e24_lhvloose_nod0	-	-	✓	✓
HLT_2e17_lhvloose_nod0_L12EM15VHI	-	-	-	✓
Single muon trigger				
HLT_mu20_iloose_L1MU15	✓	-	-	-
HLT_mu40	✓	-	-	-
HLT_mu26_ivarmedium	-	✓	✓	✓
HLT_mu50	-	✓	✓	✓

¹¹⁵⁴ 5.2.1 $t\bar{t}Z'$ signal samples

¹¹⁵⁵ Signal $t\bar{t}Z'$ samples were generated based on the simplified top-philic resonance model in
¹¹⁵⁶ section 2.2.1. Six Z' mass points were utilized for the generation of the signal sample: 1000,
¹¹⁵⁷ 1250, 1500, 2000, 2500 and 3000 GeV. The top- Z' coupling c_t is chosen to be 1 for a narrow
¹¹⁵⁸ resonance peak, and the chirality angle θ is chosen to be $\pi/4$ to suppress loop production
¹¹⁵⁹ of Z' . The samples were then generated with MADGRAPH5_AMC@NLO v.3.5.0 [120] at
¹¹⁶⁰ LO with the NNPDF3.1LO [121] PDF set interfaced with PYTHIA8 [122] using A14 tune
¹¹⁶¹ and NNPDF2.3lo PDF set for parton showering and hadronization. The resonance width is
¹¹⁶² calculated to be 4% for $c_t = 1$.

Table 5.2: Summary of all Monte-Carlo samples used in this analysis. V refers to an EW ($W^\pm/Z/\gamma^*$) or Higgs boson. Matrix element (ME) order refers to the order in QCD of the perturbative calculation. Tune refers to the underlying-event tune of the parton shower (PS) generator.

Process	ME Generator	ME Order	ME PDF	PS	Tune	Sim.
Signals						
$t\bar{t}Z'$	MADGRAPH5_AMC@NLO LO		NNPDF3.1LO		PYTHIA8 A14	FS
$t\bar{t}t\bar{t}$ and $t\bar{t}\bar{t}$						
$t\bar{t}t\bar{t}$	MADGRAPH5_AMC@NLO NLO		NNPDF3.0nlo		PYTHIA8 A14	AF3
	MADGRAPH5_AMC@NLO NLO		MMHT2014 LO		HERWIG7 H7-UE-MMHT	AF3
	SHERPA	NLO	NNPDF3.0nnlo		HERWIG7 SHERPA	FS
$t\bar{t}\bar{t}$	MADGRAPH5_AMC@NLO LO		NNPDF2.3lo		PYTHIA8 A14	AF3
$t\bar{t}V$						
$t\bar{t}H$	POWHEGBOX v2	NLO	NNPDF3.0nlo		PYTHIA8 A14	FS
	POWHEGBOX v2	NLO	NNPDF3.0nlo		HERWIG7 H7.2-Default	FS
$t\bar{t}(Z/\gamma^*)$	MADGRAPH5_AMC@NLO NLO		NNPDF3.0nlo		PYTHIA8 A14	FS
	SHERPA	NLO	NNPDF3.0nnlo		SHERPA SHERPA	FS
$t\bar{t}W$	SHERPA	NLO	NNPDF3.0nnlo		SHERPA SHERPA	FS
	SHERPA	LO	NNPDF3.0nnlo		SHERPA SHERPA	FS
$t\bar{t}$ and Single-Top						
$t\bar{t}$	POWHEGBOX v2	NLO	NNPDF3.0nlo		PYTHIA8 A14	FS
tW	POWHEGBOX v2	NLO	NNPDF3.0nlo		PYTHIA8 A14	FS
$t(q)b$	POWHEGBOX v2	NLO	NNPDF3.0nlo (s)		PYTHIA8 A14	FS
			NNPDF3.0nlo 4f (t)			FS
tWZ	MADGRAPH5_AMC@NLO NLO		NNPDF3.0nlo		PYTHIA8 A14	FS
tZ	MADGRAPH5_AMC@NLO LO		NNPDF3.0nlo 4f		PYTHIA8 A14	FS
$t\bar{t}VV$						
$t\bar{t}WW$	MADGRAPH5_AMC@NLO LO		NNPDF3.0nlo		PYTHIA8 A14	FS
$t\bar{t}WZ$	MADGRAPH	LO	NNPDF3.0nlo		PYTHIA8 A14	AF3
$t\bar{t}HH$	MADGRAPH	LO	NNPDF3.0nlo		PYTHIA8 A14	AF3
$t\bar{t}WH$	MADGRAPH	LO	NNPDF3.0nlo		PYTHIA8 A14	AF3
$t\bar{t}ZZ$	MADGRAPH	LO	NNPDF3.0nlo		PYTHIA8 A14	AF3
$V(VV)+\text{jets}$ and VH						
$V+\text{jets}$	SHERPA	NLO	NNPDF3.0nnlo		SHERPA SHERPA	FS
$VV+\text{jets}$	SHERPA	NLO	NNPDF3.0nnlo		SHERPA SHERPA	FS
		LO ($gg \rightarrow VV$)				FS
$VVV+\text{jets}$	SHERPA	NLO	NNPDF3.0nnlo		SHERPA SHERPA	FS
VH	POWHEGBOX v2	NLO	NNPDF3.0aznlo		PYTHIA8 A14	FS

₁₁₆₃ **5.2.2 Background samples**

₁₁₆₄ **SM $t\bar{t}t\bar{t}$ background**

₁₁₆₅ The nominal SM $t\bar{t}t\bar{t}$ sample was generated with MADGRAPH5_AMC@NLO [120] at
₁₁₆₆ NLO in QCD with the NNPDF3.0nlo [121] PDF set and interfaced with PYTHIA8.230 [122]
₁₁₆₇ using A14 tune [123]. Decays for top quarks are simulated at LO with MADSPIN [124,
₁₁₆₈ 125] to preserve spin information, while decays for b - and c -hadrons are simulated with
₁₁₆₉ EVTGEN v1.6.0 [126]. The renormalization and factorization scales μ_R and μ_F are set
₁₁₇₀ to $1/4\sqrt{m^2 + p_T^2}$, which represents the sum of transverse mass of all particles generated
₁₁₇₁ from the ME calculation [127]. The ATLAS detector response was simulated with AF3.
₁₁₇₂ Additional auxiliary $t\bar{t}t\bar{t}$ samples are also generated to evaluate the impact of generator and
₁₁₇₃ PS uncertainties as shown in 5.2.

₁₁₇₄ **$t\bar{t}W$ background**

₁₁₇₅ Nominal $t\bar{t}W$ sample was generated using SHERPA v2.2.10 [128] at NLO in QCD with
₁₁₇₆ the NNPDF3.0nnlo [121] PDF with up to one extra parton at NLO and two at LO, which
₁₁₇₇ are matched and merged with SHERPA PS based on Catani-Seymour dipole factorization
₁₁₇₈ [129] using the MEPS@NLO prescription [130–133] and a merging scale of 30 GeV. Higher-
₁₁₇₉ order ME corrections are provided in QCD by the OpenLoops 2 library [134–136] and in
₁₁₈₀ EW from $\mathcal{O}(\alpha^3) + \mathcal{O}(\alpha_S^2\alpha^2)$ (LO3 & NLO2) via two sets of internal event weights. An
₁₁₈₁ alternative sample with only EW corrections at LO from $\mathcal{O}(\alpha_S\alpha^3)$ (NLO3) diagrams were
₁₁₈₂ also simulated with the same settings.

₁₁₈₃ **$t\bar{t}(Z/\gamma^*)$ background**

₁₁₈₄ Nominal $t\bar{t}(Z/\gamma^*)$ samples were generated separately for different ranges of dilepton in-
₁₁₈₅ variant mass $m_{\ell\ell}$ to account for on-shell and off-shell Z/γ^* production. Sample for $m_{\ell\ell}$
₁₁₈₆ between 1 and 5 GeV was produced using MADGRAPH5_AMC@NLO [120] at NLO with
₁₁₈₇ the NNPDF3.0nlo [121] PDF set, interfaced with PYTHIA8.230 [122] using A14 tune [123] and
₁₁₈₈ NNPDF2.3l0 PDF set. Sample for $m_{\ell\ell} < 5$ GeV was produced with SHERPA v2.2.10 [128]
₁₁₈₉ at NLO using NNPDF3.0nnlo PDF set. To account for generator uncertainty, an alternative
₁₁₉₀ $m_{\ell\ell} > 5$ GeV sample was generated with identical settings to the low $m_{\ell\ell}$ sample. The
₁₁₉₁ ATLAS detector response was simulated with full detector simulation (FS).

₁₁₉₂ **$t\bar{t}H$ background**

₁₁₉₃ **$t\bar{t}t$ background**

₁₁₉₄ **$t\bar{t}$ background**

₁₁₉₅ **Single-top (tW & $t(q)b$) background**

₁₁₉₆ **tWZ background**

₁₁₉₇ **tZ & $t\bar{t}VV$ background**

₁₁₉₈ **Single boson (V) +jets background**

₁₁₉₉ **Diboson (VV) +jets background**

₁₂₀₀ **Triboson (VVV) +jets background**

₁₂₀₁ **VH background**

₁₂₀₂ **Chapter 6. Analysis Strategy**

₁₂₀₃ **6.1 Event selection**

₁₂₀₄ Events for the analysis first are preselected following a list of criteria to optimize for event
₁₂₀₅ quality and background rejection. The following criteria are applied sequentially from top
₁₂₀₆ to bottom along with cleaning and veto cuts

₁₂₀₇ 1. **Good Run List (GRL)**: data events must be part of a predefined list of suitable
₁₂₀₈ runs and luminosity blocks [[137](#)].

₁₂₀₉ 2. **Primary vertex**: events must have at least one reconstructed vertex matched to 2 or
₁₂₁₀ more associated tracks with $p_T > 500$ MeV.

₁₂₁₁ 3. **Trigger**: events must be selected by at least one trigger in Table 5.1.

₁₂₁₂ 4. **Kinematic selection**: events must have exactly two *Tight* leptons with the same
₁₂₁₃ electric charge, or at least three *Tight* leptons of any charge. The leading lepton must
₁₂₁₄ have $p_T > 28$ GeV, and all leptons must satisfy $p_T > 15$ GeV.

₁₂₁₅ Events are separated into two channels based on the number of leptons: same-sign di-
₁₂₁₆ lepton (SS2L) for events with exactly two leptons of the same charge, or multilepton (ML)
₁₂₁₇ for events with three or more leptons. The channels are further separated into regions defined
₁₂₁₈ in section 6.2 to prepare for analysis.

₁₂₁₉ Additional selections are applied based on the lepton flavors present. In the SS2L channel,
₁₂₂₀ if both leptons are electrons, the invariant mass m_{ll} must satisfy $m_{ll} < 81$ GeV and $m_{ll} > 101$
₁₂₂₁ GeV to suppress background involving Z -bosons. In the ML channel, the same criteria must
₁₂₂₂ be satisfied for every opposite-sign same-flavor pair of leptons in an event.

1223 6.1.1 Event categorization

1224 Simulated events are categorized using truth information of leptons (e/μ) and their orig-
1225 inating MC particle (mother-particle). Each lepton can be classified as either prompt or
1226 non-prompt, with non-prompt leptons further categorized for background estimation pur-
1227 poses. If an event contains only prompt leptons, the event is classified as its corresponding
1228 process. If the event contains one non-prompt lepton, the event is classified as the corre-
1229 sponding type of the non-prompt lepton. If the event contains more than one non-prompt
1230 lepton, the event is classified as other.

1231 • **Prompt:** if the lepton originates from $W/Z/H$ boson decays, or from a mother-
1232 particle created by a final state photon.

1233 • **Non-prompt:**

1234 – **Charge-flip (e only):** if the reconstructed charge of the lepton differs from that
1235 of the first mother-particle.

1236 – **Material conversion (e only):** if the lepton originated from a photon conversion
1237 and the mother-particle is an isolated prompt photon, non-isolated final state
1238 photon, or heavy boson.

1239 – **γ^* -conversion (e only):** if the lepton originated from a photon conversion and
1240 the mother-particle is a background electron.

1241 – **Heavy flavor decay:** if the lepton originated from a b - or c -hadron.

1242 – **Fake:** if the lepton originated from a light- or s -hadron, or if the truth type of
1243 the lepton is hadron.

1244 – **Other:** any lepton that does not belong to one of the above categories.

1245 6.2 Analysis regions

1246 Events are selected and categorized into analysis regions belonging to one of two types:
 1247 control regions (CRs) enriched in background events, and signal regions (SRs) enriched in
 1248 signal events. This allows for the examination and control of backgrounds and systematic
 1249 uncertainties, as well as study of signal sensitivities. The signal is then extracted from the
 1250 SRs with a profile LH fit using all regions. The full selection criteria for each region are
 1251 summarized in Table 6.1. The post-fit background compositions in different CRs and SR
 1252 sub-regions are shown in Figure 6.1.

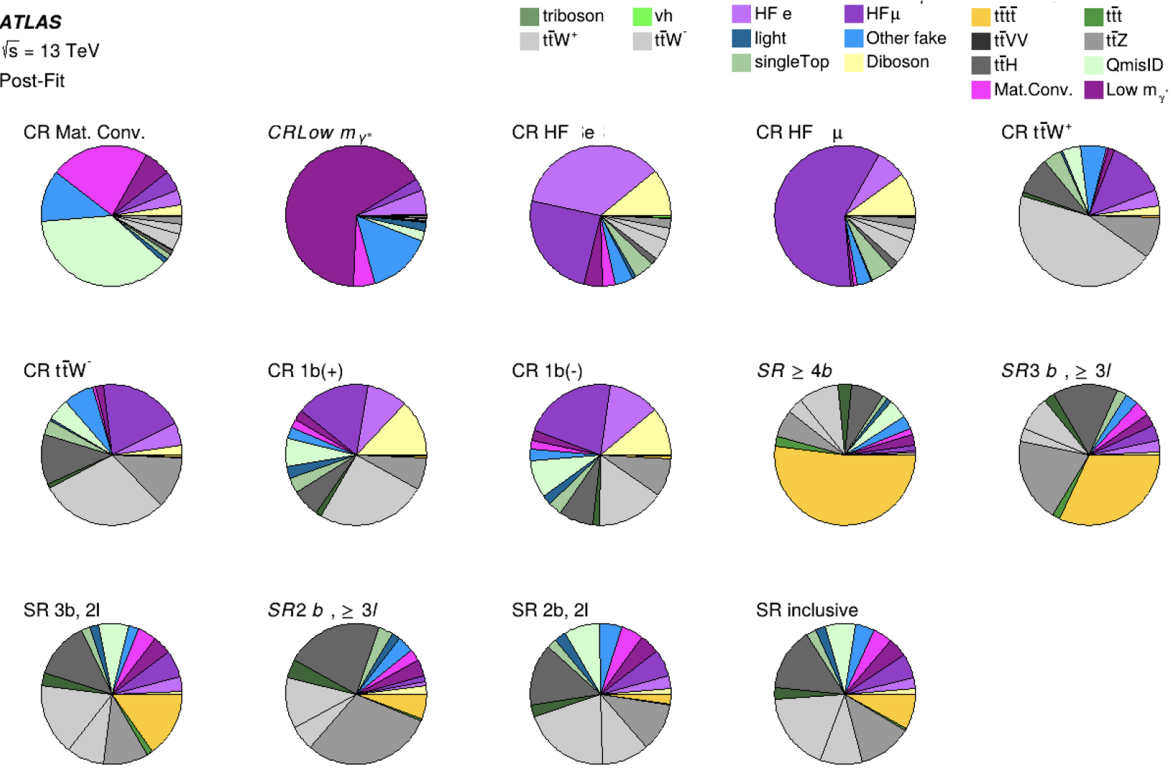


Figure 6.1: Post-fit background composition in each analysis region and sub-region. The fit was performed using ideal pseudo-datasets (Asimov data) in the SR.

Table 6.1: Definitions of signal, control and validation regions (VR) used in this analysis. N_{jets} and N_b refers to the number of jets and number of b -tagged jets respectively. ℓ_1 refers to the leading lepton, ℓ_2 refers to the subleading lepton and so on. H_T refers to the p_T scalar sum of all leptons and jets in the event. $m_{\ell\ell}$ refers to the dilepton invariant mass, which must not coincide with the Z -boson mass range of 81-101 GeV for SS2L+3L events.

Region	Channel	N_{jets}	N_b	Other selections	Fitted variable
CR Low m_{γ^*}	SS $e\ell$	[4, 6)	≥ 1	ℓ_1/ℓ_2 is from virtual photon decay $\ell_1 + \ell_2$ not from material conversion	event yield
CR Mat. Conv.	SS $e\ell$	[4, 6)	≥ 1	ℓ_1/ℓ_2 is from material conversion $\ell_1 + \ell_2$ not conversion candidates	event yield
CR HF μ	$\ell\mu\mu$	≥ 1	1	$100 < H_T < 300$ GeV $E_T^{\text{miss}} > 35$ GeV total charge = ± 1	$p_T(\ell_3)$
CR HF e	$e\ell\ell$	≥ 1	1	$\ell_1 + \ell_2$ not conversion candidates $100 < H_T < 275$ GeV $E_T^{\text{miss}} > 35$ GeV total charge = ± 1	$p_T(\ell_3)$
CR $t\bar{t}W^+$	SS $\ell\mu$	≥ 4	≥ 2	$ \eta(e) < 1.5$ for $N_b = 2$: $H_T < 500$ GeV or $N_{\text{jets}} < 6$ for $N_b \geq 3$: $H_T < 500$ GeV total charge > 0	N_{jets}
CR $t\bar{t}W^-$	SS $\ell\mu$	≥ 4	≥ 2	$ \eta(e) < 1.5$ for $N_b = 2$: $H_T < 500$ GeV or $N_{\text{jets}} < 6$ for $N_b \geq 3$: $H_T < 500$ GeV total charge < 0	N_{jets}
CR 1b(+)	SS2L+3L	≥ 4	1	$\ell_1 + \ell_2$ not from material conversion $H_T > 500$ GeV total charge > 0	N_{jets}
CR 1b(-)	SS2L+3L	≥ 4	1	$\ell_1 + \ell_2$ not from material conversion $H_T > 500$ GeV total charge < 0	N_{jets}
VR $t\bar{t}Z$	3L $\ell^\pm\ell^\mp$	≥ 4	≥ 2	$m_{\ell\ell} \in [81, 101]$ GeV	$N_{\text{jets}}, m_{\ell\ell}$
VR $t\bar{t}W +1b$	SS2L+3L			CR $t\bar{t}W^\pm$ CR 1b(\pm)	N_{jets}
VR $t\bar{t}W +1b+SR$	SS2L+3L			CR $t\bar{t}W^\pm$ CR 1b(\pm) SR	N_{jets}
SR	SS2L+3L	≥ 6	≥ 2	$H_T > 500$ GeV $m_{\ell\ell} \notin [81, 101]$ GeV	H_T

₁₂₅₃ **6.2.1 Signal regions**

₁₂₅₄ All events selected for the SR must satisfy the following criteria:

- ₁₂₅₅ • Contains 6 or more jets, with at least 2 jets b -tagged at the 85% OP.
- ₁₂₅₆ • Scalar sum of the transverse momenta of all leptons and jets $H_T > 500$ GeV.
- ₁₂₅₇ • Dilepton invariant mass $m_{\ell\ell}$ does not coincide with the Z -boson mass range of 81 – 101
₁₂₅₈ GeV

₁₂₅₉ The SR is further divided into sub-regions by the number of b -tagged jets and leptons
₁₂₆₀ present to study signal behavior and sensitivity with respect to the selection variables.

Table 6.2: Definitions of SR sub-regions. Events are sorted into different sub-regions based on the number of b -tagged jets and leptons present.

Sub-region	Selection criteria	
	b -jets	leptons
SR 2b2l	$N_b = 2$	$N_l = 2$
SR 2b3l4l	$N_b = 2$	$N_l \geq 3$
SR 3b2l	$N_b = 3$	$N_l = 2$
SR 3b3l4l	$N_b = 3$	$N_l \geq 3$
SR 4b	$N_b \geq 4$	

₁₂₆₁ **Signal extraction**

₁₂₆₂ Signal extraction in the SR is performed via a binned profile likelihood (LH) fit as de-
₁₂₆₃ scribed in section 8.1 using H_T as the discriminant observable. The discriminant observable

₁₂₆₄ for a LH fit serves as the set of observed data upon which the LH function is constructed.

₁₂₆₅ Ideally, the chosen observable shows significant separation between the functional forms of
₁₂₆₆ the signal and background distributions, allowing for effective separation of the two. Fig-

₁₂₆₇ ure 6.2 shows several pre-fit kinematic distributions in the inclusive SR. From empirical

1268 optimization studies, H_T possesses good discriminating power compared to other observ-
 1269 ables constructed using event-level information.

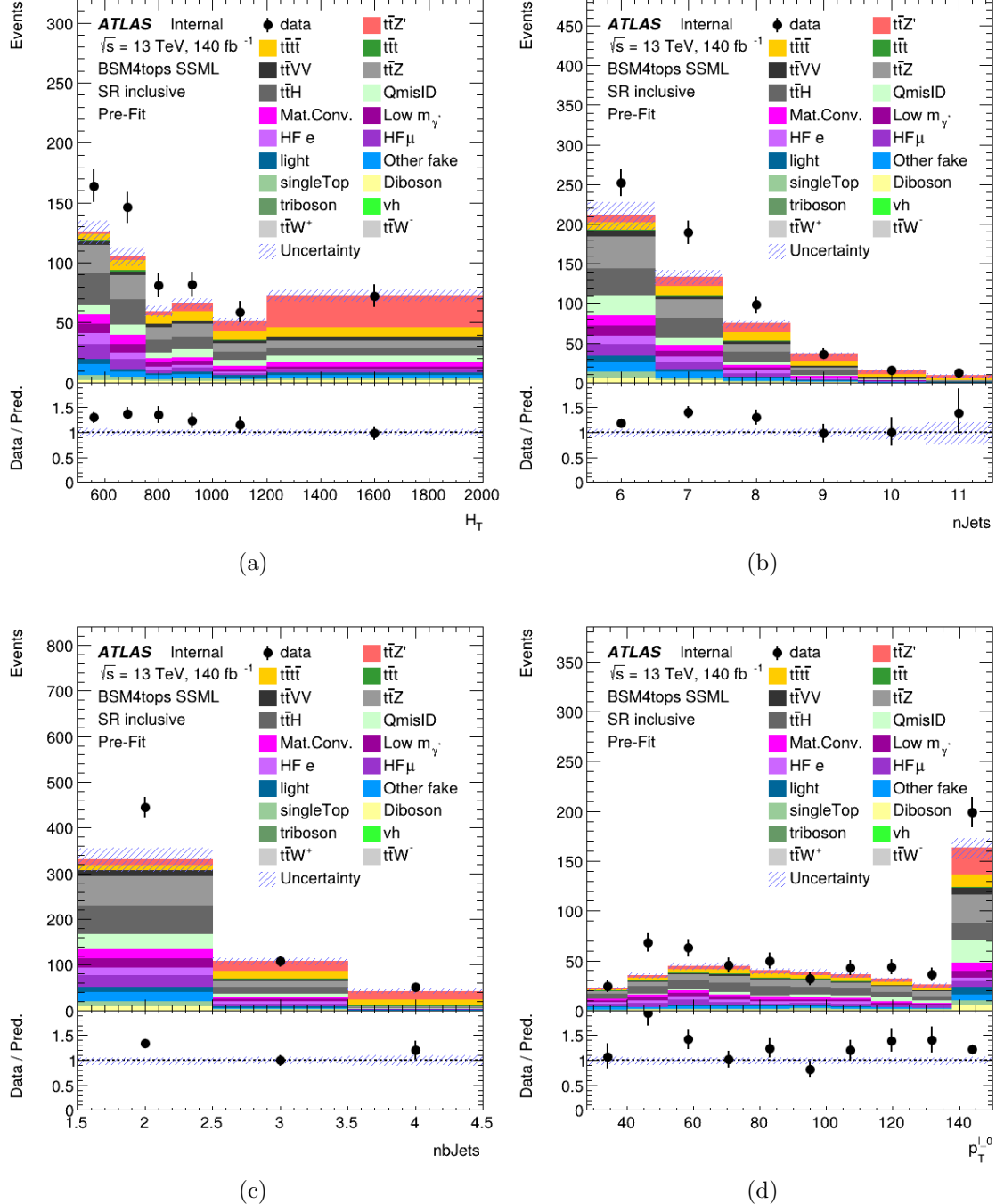


Figure 6.2: Pre-fit kinematic distributions and event compositions for several observables in the inclusive SR. The shaded band represents the uncertainty in the total distribution. The first and last bins of each distribution contain underflow and overflow events respectively.

₁₂₇₀ **6.2.2 Control regions**

₁₂₇₁ Control regions are defined for each background to be enriched in the targeted process, in
₁₂₇₂ order to maximize the background's purity and minimize contamination from other sources
₁₂₇₃ within the region. This helps to constrain and reduce correlation between background nor-
₁₂₇₄ malization factors in the final fit. Fit variables and selection criteria are determined via
₁₂₇₅ optimization studies performed on CRs that aimed to achieve the largest discriminating
₁₂₇₆ power possible between the target background and other event types.

₁₂₇₇ **$t\bar{t}W$ background CRs**

₁₂₇₈ Theoretical modeling for $t\bar{t}W$ +jets background in the phase space of this analysis suffers
₁₂₇₉ from large uncertainties, especially at high jet multiplicities [138]. A data-driven method was
₁₂₈₀ employed in a similar manner to the SM $t\bar{t}t\bar{t}$ observation analysis [44] to mitigate this effect,
₁₂₈₁ and are described in further details in section 6.3.3. The method necessitates the definition
₁₂₈₂ of two groups of dedicated CRs to estimate the flavor composition and normalization of $t\bar{t}W$
₁₂₈₃ +jets background: CR $t\bar{t}W$ +jets to constrain flavor composition, and CR 1b to constrain
₁₂₈₄ the jet multiplicity spectrum. These are further split into CR $t\bar{t}W^\pm$ and CR 1b(\pm) due to
₁₂₈₅ the pronounced asymmetry in $t\bar{t}W$ production from pp collisions, with $t\bar{t}W^+$ being produced
₁₂₈₆ at approximately twice the rate of $t\bar{t}W^-$ [139].

₁₂₈₇ Events in CR $t\bar{t}W^\pm$ are required to contain at least two b -tagged jets similar to the SR
₁₂₈₈ to determine the $t\bar{t}W$ normalization within an SR-related phase space. Orthogonality with
₁₂₈₉ SR is ensured by requiring $H_T < 500$ GeV or $N_{\text{jets}} < 6$ when $N_b = 2$, and $H_T < 500$
₁₂₉₀ GeV when $N_b \geq 3$. Events in CR 1b(\pm) are required to have $H_T > 500$ GeV and at least
₁₂₉₁ four jets to encompass events with high N_{jets} , which can be used to determine the $t\bar{t}W$ jet

1292 multiplicity spectrum for fitting $a_{0,1}$. The selection criteria also include exactly one b -tagged
1293 jet to maintain orthogonality with the SR.

1294 **Fake/non-prompt background CRs**

1295 Selection for fake/non-prompt CRs are determined using the `DFCommonAddAmbiguity`
1296 (`DFCAA`) variable for reconstructed leptons.

Table 6.3: List of possible assigned values for `DFCAA`.

DFCAA	Description
-1	No 2nd track found
0	2nd track found, no conversion found
1	Virtual photon conversion candidate
2	Material conversion candidate

1297 Four CRs are defined for the three main types of fake/non-prompt backgrounds in the
1298 analysis - virtual photon (γ^*) conversion, photon conversion in detector material (Mat.
1299 Conv.) and heavy flavor decays (HF). The full selection criteria for fake/non-prompt CRs
1300 are shown in Table 6.1.

- 1301 • **Low m_γ^* :** events with an e^+e^- pair produced from a virtual photon.

1302 Events are selected if there are two same-sign leptons with at least one electron recon-
1303 structed as an internal conversion candidate, and neither reconstructed as a material
1304 conversion candidate.

- 1305 • **Mat. Conv.:** events with an electron originating from photon conversion within the
1306 detector material.

1307 Events are selected if there are two same-sign leptons with at least one electron recon-
1308 structed as a material conversion candidate.

- 1309 • **HF** $e(\mu)$: events with a reconstructed non-prompt lepton from semi-leptonic decays of
1310 **b - and c -hadrons** (heavy flavor decays).

1311 Events are selected if there are three leptons with at least two electrons (muons), with
1312 no lepton reconstructed as a conversion candidate.

1313 6.3 Background estimation

1314 Background in this analysis consist of SM processes that can result in a signal signature
1315 similar to a $t\bar{t}t\bar{t}$ SSML final state and can be divided into two types, reducible and irreducible.
1316 Reducible background consists of processes that do not result in a SSML final state physically,
1317 but are reconstructed as such due to detector and reconstruction effects. The main types
1318 of reducible background considered are charge misidentification (QmisID) and fake/non-
1319 prompt leptons. Fake/non-prompt lepton backgrounds contaminate the SR when a non-
1320 prompt lepton is reconstructed as a prompt lepton in a $t\bar{t}$ -associated process, leading to
1321 a similar final state to that of SSML $t\bar{t}t\bar{t}$. These backgrounds are estimated using the
1322 template fitting method described in subsection 6.3.1, where MC simulations are normalized
1323 to their theoretical SM cross section via floating normalization factors (NFs) constrained by
1324 the corresponding CRs. Lepton charge misidentification background contaminates the SR
1325 similarly when one of the two leptons in a $t\bar{t}$ -associated process with two opposite-sign leptons
1326 is misidentified, producing a SS2L $t\bar{t}t\bar{t}$ final state. Charge misidentification background is
1327 estimated using a data-driven method described in section 6.3.2 along with ECIDS described
1328 in section 4.3.1.

1329 Irreducible background consists of SM processes that result in SSML final states physi-
1330 cally with all leptons being prompt. The dominating background in the SR are SM $t\bar{t}t\bar{t}$, $t\bar{t}W$,

₁₃₃₁ $t\bar{t}Z$, and $t\bar{t}H$ production with smaller contributions from VV , VVV , VH and rarer processes
₁₃₃₂ like $t\bar{t}VV$, tWZ , tZq and $t\bar{t}t$. Most irreducible backgrounds are estimated using template
₁₃₃₃ fitting method, with the exception of $t\bar{t}W + \text{jets}$ background. The $t\bar{t}W + \text{jets}$ background is
₁₃₃₄ instead given four dedicated CRs, and estimated using a data-driven method with a fitted
₁₃₃₅ function parameterized in N_{jets} . All CRs and SR are included in the final profile LH fit to
₁₃₃₆ data.

₁₃₃₇ 6.3.1 Template fitting for fake/non-prompt estimation

₁₃₃₈ Template fitting method is a semi-data-driven approach [138] that estimates fake/non-
₁₃₃₉ prompt background distributions by fitting the MC kinematic profile of background processes
₁₃₄₀ arising from fake/non-prompt leptons to data. The four main sources of fake/non-prompt
₁₃₄₁ leptons are generated from $t\bar{t} + \text{jets}$ samples and are constrained by four CRs enriched with
₁₃₄₂ the corresponding backgrounds. Each of the aforementioned background is assigned a free-
₁₃₄₃ floating NF resulting in $\text{NF}_{\text{HF } e}$, $\text{NF}_{\text{HF } \mu}$, $\text{NF}_{\text{Mat. Conv.}}$ and $\text{NF}_{\text{Low } m_{\gamma^*}}$. The NFs are fitted
₁₃₄₄ simultaneously with the signal within their constraining CRs.

₁₃₄₅ 6.3.2 Charge misidentification data-driven estimation

₁₃₄₆ The ee and $e\mu$ channels in the SS2L $t\bar{t}t\bar{t}$ region are contaminated with opposite-sign
₁₃₄₇ (OS) dilepton $t\bar{t}$ -associated events where one electron has its charge misidentified. Charge
₁₃₄₈ misidentification (QmisID) largely affects electrons due to muons' precise curvature informa-
₁₃₄₉ tion using ID and MS measurements and low bremsstrahlung rate. The charge flip rates are
₁₃₅₀ significant at higher p_T and varies with $|\eta|$ which is proportional to the amount of detector
₁₃₅₁ material the electron interacted with.

1352 The charge flip probability ϵ is estimated in this analysis with a data-driven method
 1353 [140] using a sample of $Z \rightarrow e^+e^-$ events with additional constraints on the invariant mass
 1354 m_{ee} to be within 10 GeV of the Z -boson mass. The Z -boson mass window is defined to
 1355 be within 4σ to include most events within the peak, and is determined by fitting the m_{ee}
 1356 spectrum of the two leading electrons to a Breit-Wigner function, resulting in a range of
 1357 [65.57, 113.49] for SS events and [71.81, 109.89] for OS events. Background contamination
 1358 near the peak is assumed to be uniform and subtracted using a sideband method. Since the
 1359 Z -boson decay products consist of a pair of opposite-sign electrons, all same-sign electron
 1360 pairs are considered affected by charge misidentification.

1361 Let N_{ij}^{SS} be the number of events with SS electrons with the leading electron in the
 1362 i^{th} 2D bin in $(p_T, |\eta|)$ and the sub-leading electron in the j^{th} bin. Assuming the QmisID
 1363 probabilities of electrons in an event are uncorrelated, N_{ij}^{SS} can be estimated as

$$N_{ij}^{\text{SS}} = N_{ij}^{\text{tot}} [\epsilon_i(1 - \epsilon_j) + \epsilon_j(1 - \epsilon_i)], \quad (6.1)$$

1364 where N_{ij}^{tot} is the total number of events in the i^{th} and j^{th} bin regardless of charge, and
 1365 $\epsilon_{i(j)}$ is the QmisID rate in the $i^{\text{th}}(j^{\text{th}})$ bin. Assuming N_{ij}^{SS} follows a Poisson distribution
 1366 around the expectation value \bar{N}_{ij}^{SS} , the $(i, n)^{\text{th}}$ rate ϵ can be estimated by minimizing a
 1367 negative-LLH function parameterized in p_T and $|\eta|$,

$$\begin{aligned}
 -\ln(\mathcal{L}(\epsilon | N_{\text{SS}})) &= -\ln \prod_{ij} \frac{(N_{ij}^{\text{tot}})^{N_{ij}^{\text{SS}}} \cdot e^{N_{ij}^{\text{tot}}}}{N_{ij}^{\text{SS}}!} \\
 &= -\sum_{ij} \left[N_{ij}^{\text{SS}} \ln(N_{ij}^{\text{tot}}(\epsilon_i(1 - \epsilon_j) + \epsilon_j(1 - \epsilon_i))) - N_{ij}^{\text{tot}}(\epsilon_i(1 - \epsilon_j) + \epsilon_j(1 - \epsilon_i)) \right].
 \end{aligned} \quad (6.2)$$

1368 The QmisID rates are then calculated separately for SR and CRs with different electron
 1369 definitions i.e. CR Low m_{γ^*} , CR Mat. Conv., CR $t\bar{t}W^\pm$, using events from data after
 1370 applying region-specific lepton selections and ECIDS. The events are required to satisfy
 1371 SS2L kinematic selections but contains OS electrons. The following weight is applied to OS
 1372 events to correct for misidentified SS events within the region,

$$w = \frac{\epsilon_i + \epsilon_j - 2\epsilon_i\epsilon_j}{1 - \epsilon_i - \epsilon_j + 2\epsilon_i\epsilon_j}. \quad (6.3)$$

1373 The QmisID rates calculated for SR and CR $t\bar{t}W$ are shown in Figure 6.3

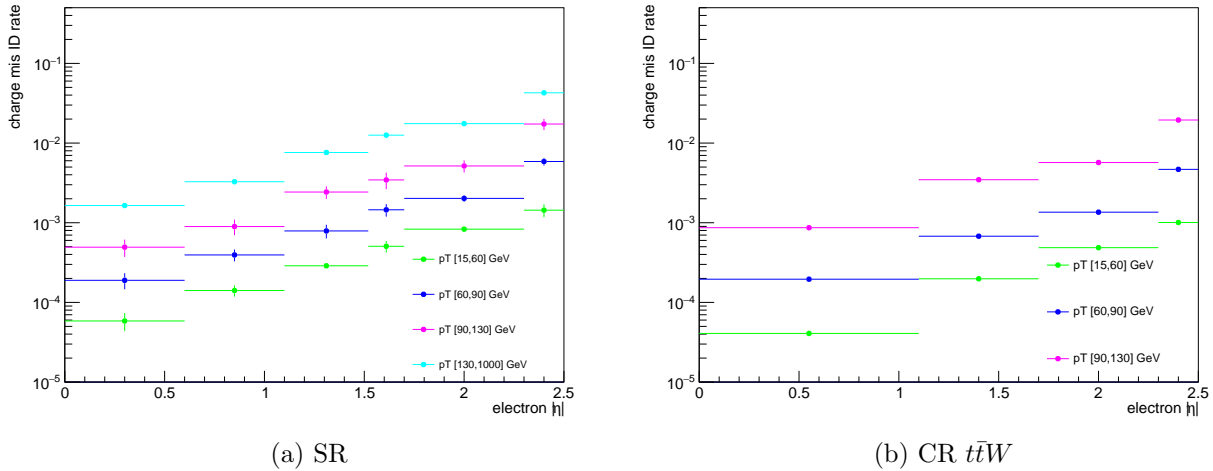


Figure 6.3: Charge flip rate calculated for SR and CR $t\bar{t}W$ in bins of $|\eta|$ and p_T .

1374 The QmisID rates obtained after applying w contain a dependency on jet multiplicity
 1375 and are underestimated at higher N_{jets} . This dependency affect the SR which require events
 1376 with ≥ 6 jets, and is corrected by applying a correction factor $SF_{i,n} = \epsilon_{i,n}/\epsilon_{i,N}$ where N is
 1377 the inclusive bin containing all N_{jets} and $\epsilon_{i,n}$ is the QmisID rate obtained from Equation 6.2
 1378 in the $(i, n)^{\text{th}}$ 2D bin in (p_T, N_{jets}) . Jet multiplicity and consequently the obtained SFs are
 1379 assumed to be independent of $|\eta|$.

1380 **6.3.3 $t\bar{t}W$ background data-driven estimation**

1381 Previously, the $t\bar{t}W$ background in $t\bar{t}t\bar{t}$ final state analysis was handled by assigning large
 1382 ad-hoc systematic uncertainties to $t\bar{t}W$ events with 7 or more jets [46]. A semi-data-driven
 1383 method [141] was shown to be effective in the SM $t\bar{t}t\bar{t}$ observation analysis [44] by improving
 1384 $t\bar{t}W$ modeling, especially in the showering step and switching $t\bar{t}W$ systematic uncertainties
 1385 from predominantly modeling to statistical.

1386 The data-driven method applies correction factors obtained from a fitted function pa-
 1387 rameterized in N_{jets} to $t\bar{t}W$ MC kinematic distributions. The QCD scaling patterns [142] can
 1388 be represented by ratio of successive exclusive jet cross-sections

$$R_{(n+1)/n} = \frac{\sigma_{n+1}}{\sigma_n} = e^{-b} + \frac{\bar{n}}{n+1} = a_0 + \frac{a_1}{1+(j-4)}, \quad (6.4)$$

1389 where $a_{0(1)}$ and b are constants, n is the number of jets in addition to the hard process, j
 1390 is the inclusive number of jets, and \bar{n} is the expectation value for the Poisson distribution
 1391 of exclusive jet cross-section at jet multiplicity n . The $t\bar{t}W$ ME for SS2L events gives 4 jets
 1392 in the hard process, so n is defined starting from the 5th jets and the inclusive number of
 1393 jets $j = n + 4$. The two terms in Equation 6.4 correspond to staircase and Poisson scaling
 1394 in cross section between successive jet multiplicities and are sensitive to high and low jet
 1395 multiplicity events respectively [142]. The scaling pattern can then be reparameterized in
 1396 a_0 and a_1 to obtain the $t\bar{t}W$ yield at $j' \equiv j + 1$ jets

$$\text{Yield}_{t\bar{t}W(j')} = \text{Yield}_{t\bar{t}W(N_{\text{jets}}=4)} \times \prod_{j=4}^{j'-1} \left(a_0 + \frac{a_1}{1+(j-4)} \right) \quad (6.5)$$

1397 with $j \geq 4$. The $t\bar{t}W$ yield in the 4-jet bin can be represented by a NF applied to $t\bar{t}W$ MC
1398 simulation

$$\text{Yield}_{t\bar{t}W(N_{\text{jets}}=4)} = \text{NF}_{t\bar{t}W(N_{\text{jets}}=4)} \times \text{MC}_{t\bar{t}W(N_{\text{jets}}=4)}. \quad (6.6)$$

1399 To account for the asymmetry in $t\bar{t}W^+$ and $t\bar{t}W^-$ cross-sections, $\text{NF}_{t\bar{t}W(N_{\text{jets}}=4)}$ is further
1400 split into $\text{NF}_{t\bar{t}W^\pm(N_{\text{jets}}=4)}$ assuming the scaling is the same for both processes. Both NFs
1401 are left free-floating to constrain $t\bar{t}W$ yields in the 4-jet bin within CR 1b(+) and CR 1b(-).
1402 The final N_{jets} -parameterized function can then be represented by $\text{NF}_{t\bar{t}W(j')}$ as

$$\text{NF}_{t\bar{t}W(j')} = \left(\text{NF}_{t\bar{t}W^+(N_{\text{jets}}=4)} + \text{NF}_{t\bar{t}W^-(N_{\text{jets}}=4)} \right) \times \prod_{j=4}^{j'-1} \left(a_0 + \frac{a_1}{1+(j-4)} \right). \quad (6.7)$$

1403 The normalization is calculated and applied separately for each sub-sample of $t\bar{t}W^+$ and
1404 $t\bar{t}W^-$ in a N_{jets} bin for $4 \leq N_{\text{jets}} < 10$. Due to small contributions in the CRs, events
1405 with $N_{\text{jets}} < 4$ and $N_{\text{jets}} \geq 10$ are not normalized with this scheme. Instead, $N_{\text{jets}} < 4$
1406 events are fitted by propagating the normalization in the 4-jet bin without additional shape
1407 correction. The correction factor for $t\bar{t}W$ events with $N_{\text{jets}} \geq 10$ is obtained by summing
1408 up the overflow from $N_{\text{jets}} = 10$ to $N_{\text{jets}} = 12$, described as $\sum_{j'=10}^{12} \prod_{j=4}^{j'-1} \left(a_0 + \frac{a_1}{1+(j-4)} \right)$.
1409 Events with $N_{\text{jets}} \geq 13$ are negligible and are not included in the sum.

1410 The four regions, CR $t\bar{t}W^\pm$ and CR 1b(\pm), are constructed to fit $\text{NF}_{t\bar{t}W^\pm(N_{\text{jets}}=4)}$ and
1411 the scaling parameters $a_{0(1)}$, as well as validating the parameterization. Assuming the N_{jets}
1412 distribution of $t\bar{t}W$ is similar across bins of N_b -jets, a fitted N_{jets} distribution in CR 1b(\pm)
1413 can be used to describe the $t\bar{t}W$ parameterization at higher N_{jets} .

1414 Chapter 7. Systematic Uncertainties

1415 Physics analysis inherently incurs uncertainties in the form of statistical and systematic
1416 uncertainties, depending on the source. Statistical uncertainties occur in this analysis from
1417 sample size of collected data and simulated MC samples, and from the maximizing of the
1418 LH function. Systematic uncertainties depend on identifiable sources in the analysis i.e.
1419 from detector and reconstruction effects (experimental uncertainties) or theoretical modeling
1420 (theoretical uncertainties). Systematic uncertainties are represented as nuisance parameters
1421 (NP_x) in the profile LH fit. During the fit, systematic uncertainties with negligible impact
1422 on the final results can be pruned to simplify the statistical model and reduce computational
1423 complexity. This section outlines all uncertainties considered in this analysis.

1424 7.1 Experimental uncertainties

1425 7.1.1 Luminosity & pile-up reweighting

1426 The uncertainty on the integrated luminosity of the 2015-2018 Run 2 data set is 0.83%
1427 [87], obtained by the LUCID-2 detector [143] for the primary luminosity measurements and
1428 complemented by the ID and calorimeters. Pile-up was modeled in MC and calibrated
1429 to data through pile-up reweighting, resulting in a set of calibration SFs and associated
1430 uncertainties.

1431 7.1.2 Leptons

1432 In general, calibrating MC simulations to match performance in data incurs uncertainties
1433 associated obtaining the MC-to-data calibration SFs, which are in turn propagated to observ-

Table 7.1: Summary of the experimental systematic uncertainties considered in this analysis.

Systematic uncertainty	Components
Event	
Luminosity	1
Pile-up reweighting	1
Electrons	
Trigger efficiency	1
Reconstruction efficiency	1
Identification efficiency	1
Isolation efficiency	1
Energy scale	1
Energy resolution	1
Charge identification (ECIDS) efficiency	1
Muons	
Trigger efficiency	2
Track-to-vertex association efficiency	2
Reconstruction/identification efficiency	2
Low- p_T (< 15 GeV) reconstruction/identification efficiency	2
Isolation efficiency	2
Charge-independent momentum scale	1
Charge-dependent momentum scale	4
Energy resolution (CB)	1
Energy resolution (ID & MS)	2
Jets	
JES effective NP	15
JES η intercalibration	3
JES flavor composition	2
JES flavor response	1
JES pile-up	4
JES punch-through (FS/AF3)	2
JES non-closure	1
JES high- p_T single particle	1
JES b -jet response	1
JER effective NP	12
JER data/MC (FS/AF3)	2
JVT efficiency	1
GN2v01 b -tagging efficiency	85
GN2v01 c -tagging efficiency	56
GN2v01 light-tagging efficiency	42
E_T^{miss} track-based soft terms	
Transversal resolution	1
Longitudinal resolution	1
Longitudinal energy scale	1

1434 ables in the analysis. The data-to-MC calibration of trigger, reconstruction, identification
1435 and isolation efficiencies for electrons and muons incur associated uncertainties, with sepa-
1436 rate systematic and statistical components for those related to muons. Similarly, electron
1437 energy scale, muon momentum scale and resolution are also subjected to calibration uncer-
1438 tainties estimated by re-simulating the events while varying the energy/momentun scale and
1439 resolution. Electron has an additional uncertainty related to ECIDS efficiency. Muon has
1440 additional uncertainties for charge-independent and charge-dependent momentum scale, as
1441 well as detector-specific track resolution. Systematic uncertainties for electron reconstruc-
1442 tion, identification, isolation, ECIDS efficiencies and muon ID/MS energy resolution were
1443 not ready for the sample version used in this analysis, and are therefore not included.

1444 7.1.3 Jets

1445 Experimental uncertainties for jets are dominated by flavor tagging-related uncertainties,
1446 with subleading contributions from uncertainties related to JES [110], JER [109] and JVT
1447 [144] calibrations.

1448 Jet energy scale

1449 Uncertainties associated with JES are determined using data from LHC collisions along
1450 with MC simulated samples [110], decomposed into uncorrelated components:

- 1451 • **Effective NPs:** 15 total p_T -dependent uncertainty components measured in situ,
1452 grouped based on their origin (2 detector-related, 4 modeling-related, 3 mixed, 6
1453 statistical-related)
- 1454 • η **intercalibration:** 6 total components (1 modeling-related, 4 non-closure and 1

1455 statistical-related) associated with the correction of the forward jets' ($0.8 \leq |\eta| < 4.5$)
1456 energy scale to that of the central jets ($|\eta| < 0.8$).

1457 • **Flavor composition & response:** 2 components for relative quark-gluon flavor com-
1458 positions in background and signal samples, and 2 components for responses to gluon-
1459 initiated versus quark-initiated jets.

1460 • **Pile-up subtraction:** 4 components, 2 for μ (`OffsetMu`) and N_{PV} (`OffsetNPV`) mod-
1461 eling, 1 for residual p_{T} -dependency (`PtTerm`) and 1 for topology dependence on the
1462 per-event p_{T} density modeling (`RhoTopology`).

1463 • **Punch-through effect treatment:** 2 terms for GSC punch-through jet response
1464 deviation between data and MC, one for each detector response simulation method
1465 (AF3 and FS).

1466 • **Non-closure:** 1 term applied to AF3 sample to account for the difference between
1467 AF3 and FS simulation.

1468 • **High- p_{T} single-particle response:** 1 term for the response to high- p_{T} jets from
1469 single-particle and test-beam measurements.

1470 • **b -jets response:** 1 term for the difference between b -jets and light-jets response.

1471 Jet energy resolution

1472 Measurements of JER were performed in bins of p_{T} and η , separately in data using in-
1473 situ techniques and in MC simulation using dijet events [109]. This analysis uses the full
1474 correlation JER uncertainty scheme provided for Run 2 analysis with 14 total components:

₁₄₇₅ 12 for effective NPs and 2 for difference between data and MC, separately for AF3 and FS

₁₄₇₆ [109].

₁₄₇₇ **Jet vertex tagging**

₁₄₇₈ The uncertainty associated with JVT is obtained by varying the JVT efficiency SFs

₁₄₇₉ within their uncertainty range [144]. This uncertainty accounts for remaining contamination

₁₄₈₀ from pile-up jets after applying pile-up suppression and MC generator choice.

₁₄₈₁ **Flavor tagging**

₁₄₈₂ Calibration SFs for b -tagging efficiencies and c -/light-jets mistagging rates are derived as

₁₄₈₃ a function of p_T for b -, c -, light-jets and PCBT score. The full set of flavor tagging-related

₁₄₈₄ uncertainties was reduced in dimensions by diagonalizing the uncertainty covariance matrix

₁₄₈₅ via eigendecomposition [113], resulting in a compact set of orthogonal NPs for this analysis:

₁₄₈₆ 85 for b -jets, 56 for c -jets and 42 for light-jets.

₁₄₈₇ **7.1.4 Missing transverse energy**

₁₄₈₈ Uncertainties on E_T^{miss} arise from possible mis-calibration of the soft-track component

₁₄₈₉ and are estimated using data-to-MC comparison of the p_T scale and resolution between

₁₄₉₀ the hard and soft E_T^{miss} components [118]. These uncertainties are represented by three

₁₄₉₁ independent terms: 1 for scale uncertainty and 2 for resolution uncertainty of the parallel

₁₄₉₂ and perpendicular components.

₁₄₉₃ **7.2 Modeling uncertainties**

₁₄₉₄ **7.2.1 Signal and irreducible background uncertainties**

₁₄₉₅ The signal and background samples used are modeled using MC simulation. Most uncer-
₁₄₉₆ tainties on simulation parameters (e.g. generator choice, PS model) are estimated by varying
₁₄₉₇ the relevant parameters and comparing them with the nominal sample. Uncertainties in-
₁₄₉₈ volving PDF in particular for most processes in the analysis are set to a flat 1% uncertainty.
₁₄₉₉ Cross-section uncertainties were considered for all irreducible background except $t\bar{t}W$, which
₁₅₀₀ is normalized in dedicated CRs following section 6.3.3. Extra uncertainties for the produc-
₁₅₀₁ tion of four or more b -jets (additional b -jets) in association with $t\bar{t}X$ and HF jets were also
₁₅₀₂ considered due to a lack of theoretical predictions or dedicated measurements, rendering
₁₅₀₃ MC modeling challenging. Uncertainties from missing higher-order QCD corrections in MC
₁₅₀₄ simulation are estimated by varying the renormalization scale μ_R and factorization scale μ_F
₁₅₀₅ within seven different combinations

$$(\mu_R, \mu_F) = \{(0.5, 0.5), (0.5, 1), (1, 0.5), (1, 1), (1, 2), (2, 1), (2, 2)\}.$$

₁₅₀₆ Process-specific uncertainty treatments are detailed below.

₁₅₀₇ **SM $t\bar{t}t\bar{t}$ background**

₁₅₀₈ The generator uncertainty for the SM $t\bar{t}t\bar{t}$ background was evaluated between a nominal
₁₅₀₉ sample of MADGRAPH5_AMC@NLO and SHERPA. The parton shower uncertainty was
₁₅₁₀ evaluated between PYTHIA8 and HERWIG. The cross-section uncertainty was estimated to

1511 be 20% computed from a prediction at NLO in QCD+EW [127].

1512 $t\bar{t}t$ background

1513 The cross-section uncertainty for $t\bar{t}t$ was estimated to be 30% computed from a prediction
1514 at NLO in QCD+EW [127]. Events with additional b -jets also incur a 50% uncertainty.

1515 $t\bar{t}W$, $t\bar{t}Z$, $t\bar{t}H$ backgrounds

1516 For $t\bar{t}W$, $t\bar{t}Z$ and $t\bar{t}H$ backgrounds, an uncertainty of 50% is assigned to events with one
1517 additional truth b -jets that did not originate from a top quark decay, and an added 50%
1518 uncertainty is assigned to events with two or more [145] additional b -jets. The generator
1519 uncertainty was estimated for $t\bar{t}Z$ using a MADGRAPH5_AMC@NLO nominal sample and
1520 a SHERPA sample, and for $t\bar{t}H$ using POWHEGBOX samples interfaced with PYTHIA8 (nom-
1521 inal) and HERWIG7. Cross-section uncertainties of 12% and 10% were applied to $t\bar{t}Z$ and
1522 $t\bar{t}H$ respectively [146]. No $t\bar{t}W$ cross-section or PDF uncertainty was considered since the
1523 normalizations and jet multiplicity spectrum for $t\bar{t}W$ are estimated using the data-driven
1524 method described in section 6.3.3.

1525 Other backgrounds

1526 Other backgrounds include processes with small overall contribution in the SR. The
1527 cross-section uncertainty for tZ and tWH is considered to be 30% [147, 148]. A conservative
1528 cross-section uncertainty of 50% is applied to $t\bar{t}VV$, VVV and VH . For VV , the cross-
1529 section uncertainty is dependent on jet multiplicity and is considered to be 20%/50%/60%
1530 for events with $\leq 3/4 \geq 5$ jets [149]. For VV , $t\bar{t}VV$, VVV and VH events with additional
1531 truth b -jets, an uncertainty of 50% is applied.

₁₅₃₂ **7.2.2 Reducible background uncertainties**

₁₅₃₃ Reducible backgrounds consist of $t\bar{t}/V + \text{HF}$ jets and single top events. Reducible back-
₁₅₃₄ ground has small contamination within the SR, thus uncertainties related to reducible back-
₁₅₃₅ ground have minor impact. Treatment for reducible background in this analysis largely
₁₅₃₆ follows Ref. [44], except for QmisID.

₁₅₃₇ **Charge misidentification**

₁₅₃₈ Uncertainties on the QmisID background originate from the charge flip rates obtained
₁₅₃₉ using the data-driven method described in section 6.3.2. Four sources of uncertainty were
₁₅₄₀ considered: statistical uncertainty from the maximum LLH estimation using Equation 6.2;
₁₅₄₁ uncertainty from choice of the Z -mass window and sidebands; non-closure uncertainty de-
₁₅₄₂ fined as the relative difference between the number of SS and OS events; and statistical
₁₅₄₃ uncertainty from the N_{jets} dependency correction SFs. The combined uncertainties from
₁₅₄₄ all four sources are calculated separately for each region involved in section 6.3.2, and are
₁₅₄₅ treated as correlated across all regions. Figure 7.1 shows the uncertainty calculated for SR.

₁₅₄₆ **Internal (low γ^*) and material conversion**

₁₅₄₇ The normalization for internal and material conversion backgrounds are free parameters
₁₅₄₈ in the fit, as a result the only uncertainties evaluated are from the shape of the distributions
₁₅₄₉ used in the template fit method (see section 6.3.1). The uncertainties on internal (material)
₁₅₅₀ conversion are estimated based on the difference between data and MC prediction in a region
₁₅₅₁ enriched in $Z + \gamma \rightarrow \mu^+\mu^- + e^+e^-$ events.

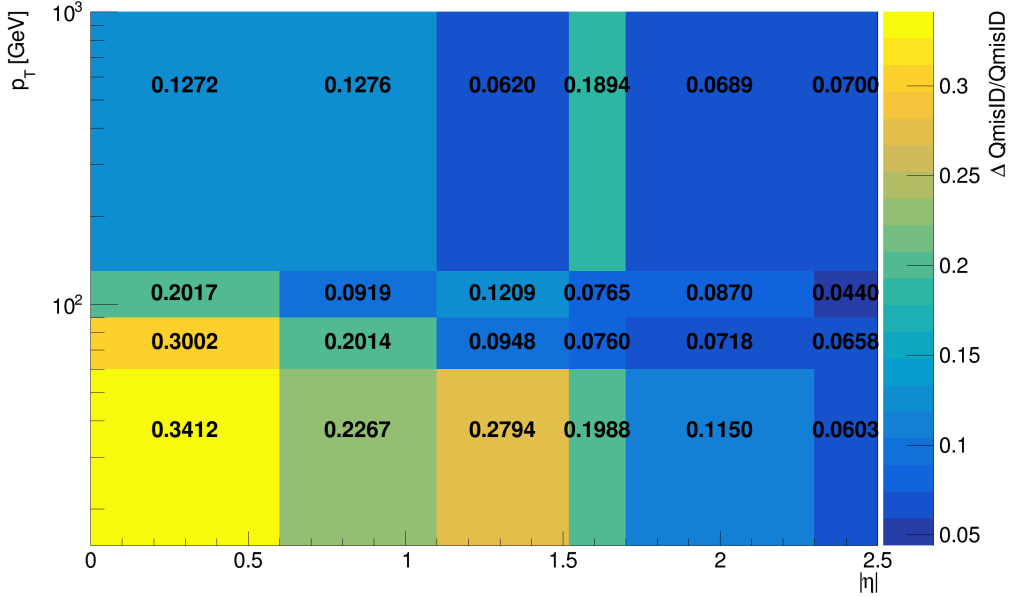


Figure 7.1: Combined QmisID uncertainty rate for SR in bins of $|\eta|$ and p_T .

1552 Heavy-flavor non-prompt lepton

1553 Similar to the conversion backgrounds, the uncertainties on non-prompt HF decays come
1554 from the shape of the distributions, and are estimated by comparing data and MC prediction
1555 between all regions in the analysis on a per bin basis. The events used are required to
1556 contain at least one *Loose* reconstructed lepton used in the region selection criteria detailed
1557 in Table 6.1 to maintain orthogonality with the SR.

1558 Light-flavor decays and other fake/non-prompt backgrounds

1559 A conservative normalization uncertainty of 100% is assigned for light-flavor non-prompt
1560 lepton background [138], and an ad-hoc normalization uncertainty of 30% is applied to all
1561 other fake and non-prompt backgrounds. The shape uncertainties for these backgrounds are
1562 negligible.

1563 **Chapter 8. Results**

1564 **8.1 Statistical interpretation**

1565 This section provides an overview of the statistical methods needed to interpret the
1566 collected and simulated data to estimate unknown physics parameters and determine com-
1567 patibility between data and the analysis hypothesis. For the BSM resonance search, the null
1568 hypothesis H_0 assumes only SM background contributions and none from any new BSM
1569 resonance in the data.

1570 **8.1.1 Profile likelihood fit**

1571 Given a set of observed data points $\mathbf{x} = [x_1, x_2, \dots]$ and unknown parameters $\boldsymbol{\theta} =$
1572 $[\theta_1, \theta_2, \dots, \theta_n]$, the maximum likelihood method aims to find an estimate $\hat{\boldsymbol{\theta}}$ that maximizes
1573 the joint probability function $f(\mathbf{x}, \boldsymbol{\theta})$, or in other words the set of parameters that gives the
1574 highest probability of observing the collected data points for a particular model. The func-
1575 tion to be maximized for this purpose is the log-likelihood (LLH) function $\ln \mathcal{L}(\mathbf{x}, \boldsymbol{\theta})$ where
1576 $\mathcal{L}(\mathbf{x}, \boldsymbol{\theta}) \equiv \prod_i f(x_i, \boldsymbol{\theta})$ is defined as the likelihood (LH) function. The LLH is maximized
1577 when $\partial/\partial\theta_i (\ln \mathcal{L}) = 0$ for each parameter θ_i .

1578 For an usual binned physics analysis, the above variables for the LH function \mathcal{L} can
1579 be expressed as nuisance parameters (NP) $\boldsymbol{\theta}$ and number of events for a model $N_i(\mu)$ for
1580 the i^{th} bin, where μ is the targeted parameter of interest (POI). In this analysis, N_i is
1581 assumed to follow a Poisson distribution and depends on the following quantities: the signal
1582 strength μ defined as the ratio of observed to expected cross sections $\sigma_{\text{obs}}/\sigma_{\text{exp}}$; nuisance
1583 parameters $\boldsymbol{\theta}$ which represents the effects of systematic uncertainties, implemented in the

1584 LH function as Gaussian constraints; and normalization factors (NFs) $\boldsymbol{\lambda}$ that control the
 1585 normalization of background components that do not have a well-known cross section. The
 1586 Poisson probability of observing exactly N_i events for an expected number of event n_i is

$$\mathcal{P}(N_i|n_i(\mu, \boldsymbol{\lambda})) = \frac{n_i^{N_i} e^{-n_i}}{N_i!}. \quad (8.1)$$

1587 The expected Poisson event number in a bin i can be parameterized as

$$n_i = \mu s_i(\boldsymbol{\theta}) + \sum_j \lambda_j b_{ij}(\boldsymbol{\theta}), \quad (8.2)$$

1588 where s_i is the number of signal events in bin i of every region, and b_{ij} is the number of
 1589 events for a certain background source index j in bin i . The LH function in this analysis
 1590 can be written as

$$\mathcal{L}(\mathbf{N}|\mu, \boldsymbol{\theta}, \boldsymbol{\lambda}) = \left(\prod_i \mathcal{P}(N_i|n_i) \right) \cdot \prod_k \mathcal{G}(\theta_k), \quad (8.3)$$

1591 where $\mathcal{G}(\theta_k)$ is the Gaussian constraint for a NP k . The signal significance μ and NFs $\boldsymbol{\lambda}$ are
 1592 left unconstrained and are fitted simultaneously in the profile LH fit. Define the profile LH
 1593 ratio [150] as

$$\lambda(\mu) = \frac{\mathcal{L}(\mu, \hat{\boldsymbol{\theta}}_\mu, \hat{\boldsymbol{\lambda}}_\mu)}{\mathcal{L}(\hat{\mu}, \hat{\boldsymbol{\theta}}, \hat{\boldsymbol{\lambda}})}, \quad (8.4)$$

1594 where $\hat{\mu}$, $\hat{\boldsymbol{\theta}}$ and $\hat{\boldsymbol{\lambda}}$ are parameter values that optimally maximizes the LH function, and $\hat{\boldsymbol{\theta}}_\mu$,
 1595 $\hat{\boldsymbol{\lambda}}_\mu$ are NP and NF values respectively that maximize the LH function for a given signal
 1596 strength μ . Using Neyman-Pearson lemma [151], the optimal test statistic for hypothesis
 1597 testing is

$$q_\mu \equiv -2 \ln \lambda(\mu), \quad (8.5)$$

1598 where $q_\mu = 0$ or $\lambda(\mu) = 1$ corresponds to perfect agreement between the optimal parameter
 1599 $\hat{\mu}$ obtained from data and the hypothesized value μ . From Wilks' theorem [152], the test
 1600 statistic q_μ approaches a χ^2 distribution and can be evaluated as $q_\mu = (\mu - \hat{\mu})^2 / \sigma_\mu^2$.

1601 When evaluating against the background-only hypothesis ($\mu = 0$), it can be assumed
 1602 that the number of events observed under the signal hypothesis is higher than that of the
 1603 background-only hypothesis, or $\mu \geq 0$ according to Equation 8.2. This leads to a corre-
 1604 sponding lower bound on the test statistic

$$q_0 = \begin{cases} -2 \ln \lambda(0), & \text{if } \hat{\mu} \geq 0, \\ 0, & \text{if } \hat{\mu} < 0. \end{cases} \quad (8.6)$$

1605 ***p*-value**

1606 To quantify the incompatibility between the observed data and the background-only hy-
 1607 pothesis, the *p*-value is defined as $p = P(q_\mu \geq q_{\mu, \text{obs}} | H_0)$ or in other words, the probability
 1608 of observing data with a test statistic q_μ under the null hypothesis H_0 that is less compat-
 1609 ible with H_0 than the actual observed data with test statistic $q_{\mu, \text{obs}}$. The *p*-value can be
 1610 expressed in terms of q_μ as

$$p_\mu = \int_{q_{\mu, \text{obs}}}^{\infty} f(q_\mu | \mu) dq_\mu, \quad (8.7)$$

1611 where $f(q_\mu | \mu) dq_\mu$ is the conditional probability density function of q_μ given μ .

1612 In some cases, it is more convenient to evaluate compatibility using the *Z*-value, defined
 1613 as the number of standard deviations between the observed data and the mean in a Gaussian

₁₆₁₄ distribution. The p -value can be converted to Z -value via the relation

$$Z = \Phi^{-1}(1 - p), \quad (8.8)$$

₁₆₁₅ where Φ is the quantile of the standard Gaussian. Rejecting the signal hypothesis usually
₁₆₁₆ requires a 95% confidence level (CL) which corresponds to a p -value of 0.05 or a Z -value of
₁₆₁₇ 1.64, while rejecting the background-only hypothesis generally requires a Z -value of 5 or a
₁₆₁₈ p -value of 2.84×10^{-7} .

₁₆₁₉ 8.1.2 Exclusion limit

₁₆₂₀ If the signal hypothesis is rejected, the exclusion upper limits can still be computed at
₁₆₂₁ a certain CL (usually 95%) to establish the maximum value of μ that is not excluded by
₁₆₂₂ the observed data. The exclusion limits are calculated based on the CL_s method [153, 154]
₁₆₂₃ under which the test statistic is defined as $q_\mu = -2 \ln \frac{\mathcal{L}_{s+b}}{\mathcal{L}_b}$ with \mathcal{L}_{s+b} being the LH function
₁₆₂₄ for the signal and background hypothesis ($\mu > 0$) and \mathcal{L}_b being the LH function for the
₁₆₂₅ background-only hypothesis ($\mu = 0$). The p -value for both hypotheses can then be expressed
₁₆₂₆ as

$$\begin{aligned} p_{s+b} &= P(q \geq q_{\text{obs}} | s + b) = \int_{q_{\text{obs}}}^{\infty} f(q | s + b) dq \\ p_b &= P(q \geq q_{\text{obs}} | b) = \int_{-\infty}^{q_{\text{obs}}} f(q | b) dq. \end{aligned} \quad (8.9)$$

₁₆₂₇ The signal hypothesis is excluded for a CL α when the following condition is satisfied

$$\text{CL}_s \equiv \frac{p_{s+b}}{p_b} \geq 1 - \alpha. \quad (8.10)$$

₁₆₂₈ The value of μ such that the signal hypothesis leads to $CL_s = 1 - \alpha = 0.05$ is then the
₁₆₂₉ exclusio upper limit at a 95% CL.

₁₆₃₀ 8.2 Fit results

₁₆₃₁ The signal strength μ , background NFs, $t\bar{t}W$ scaling factors and uncertainty NPs are
₁₆₃₂ simultaneously fitted using a binned profile LLH fit under the background-only hypothesis
₁₆₃₃ to the H_T distribution in the SR and to corresponding distributions shown in Table 6.1 for
₁₆₃₄ CRs.

₁₆₃₅ Before fitting to real data (unblinded fit), the fit was first performed in both the SR
₁₆₃₆ and CRs using Asimov pseudo-datasets, in which the simulated data match exactly to MC
₁₆₃₇ prediction with nominal μ set to 0. This is done for the purpose of optimizing object selection
₁₆₃₈ criteria and region definition, refining background estimation techniques and testing the
₁₆₃₉ statistical interpretation model for signal extraction described in section 8.1. The fit is then
₁₆₄₀ performed with Asimov data in the SR and real data in CRs to validate background modeling,
₁₆₄₁ estimate sensitivity and assess the influence of statistical effects on fitted parameters. Finally,
₁₆₄₂ the fully unblinded fit is performed with real data in all regions.

₁₆₄₃ The unblinded fit results are presented below. No significant excess over SM predictions
₁₆₄₄ is observed, and the fitted signal strength μ is compatible with zero for all Z' mass points.
₁₆₄₅ Figure 8.1 shows the observed and expected upper limits at 95% confidence level on the
₁₆₄₆ cross-section of $pp \rightarrow t\bar{t}Z'$ production times the branching ratio of $Z' \rightarrow t\bar{t}$ as a function of
₁₆₄₇ the Z' resonance mass. The exclusion limits range from 7.9 fb to 9.44 fb depending on $m_{Z'}$.

₁₆₄₈ No significant variation is observed in fit output behavior using $t\bar{t}Z'$ samples of different
₁₆₄₉ $m_{Z'}$; results fitted using $m_{Z'} = 2$ TeV are shown without substantial loss of generality.

1650 The background modeling is evaluated under the background-only hypothesis. The fitted
1651 background NFs are shown in Table 8.1 and are consistent with their nominal values within
1652 one standard deviation, or two standard deviations in the case of $\text{NF}_{\text{HF } e}$ and $\text{NF}_{t\bar{t}W+(4j)}$.
1653 Figure 8.2 shows good agreement between data and post-fit background distributions in
1654 non-prompt background CRs and $t\bar{t}W$ CRs.

1655 The pre-fit and post-fit background yields are shown in Table 8.2. Except for HF e
1656 background, post-fit yields for various backgrounds e.g. $t\bar{t}t\bar{t}$, $t\bar{t}H$, other fake, etc. are
1657 increased; the pre-fit to post-fit variations are consistent within $\pm\sigma$. Data and total post-fit
1658 yields are also consistent within $\pm\sigma$. Post-fit yield for HF e background is lowered compared
1659 to pre-fit yield within within 2σ which can be related to the fitted value of $\text{NF}_{\text{HF } e}$ in
1660 Table 8.1; however, this difference in pre- and post-fit yields of HF e background has negligible
1661 impact on the μ as seen in Table 8.3.

1662 Table 8.3 outlines the impact on the signal strength μ of various sources of uncertainty
1663 grouped by their corresponding category. The background sources of uncertainty with the
1664 largest impact is $t\bar{t}t\bar{t}$ modeling, in particular $t\bar{t}t\bar{t}$ generator choice and cross-section uncer-
1665 tainties, followed by $t\bar{t}W$ modeling due to their significant contributions in the SR observed
1666 in Figure 6.1, especially in the more sensitive regions requiring three or more b -tagged jets.
1667 The most significant impact on μ within the set of instrumental uncertainties are uncertain-
1668 ties on jet b -tagging attributable to the high jet and b -jet multiplicities in the BSM $t\bar{t}t\bar{t}$ signal
1669 signature.

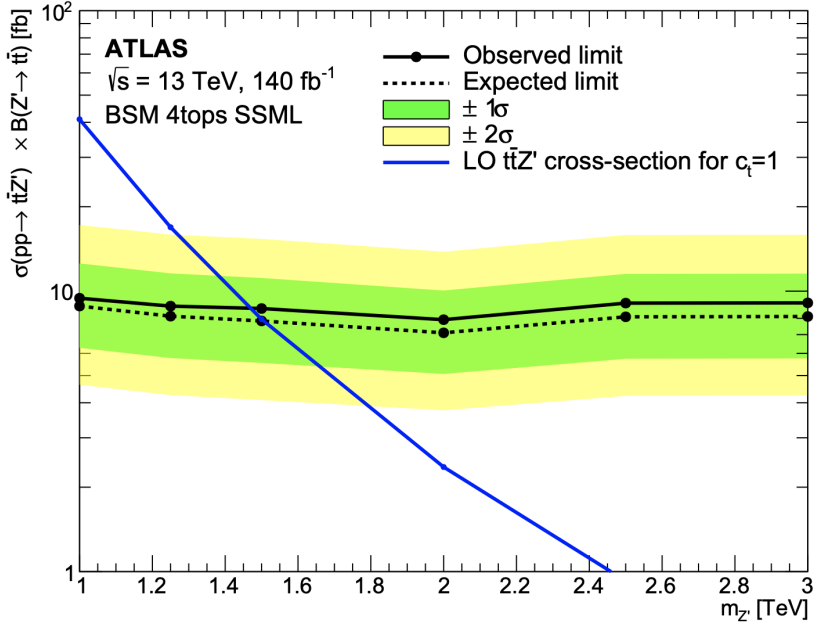


Figure 8.1: Observed (solid line) and expected (dotted line) upper limits as a function of the Z' mass at 95% CL on the cross-section of $pp \rightarrow t\bar{t}Z'$ production times the $Z' \rightarrow t\bar{t}$ branching ratio. The region above the observed limit is excluded. The solid blue line represents the theoretical signal cross-section with $c_t = 1$ at LO in QCD [71]. The green and yellow bands represent the 68% ($\pm\sigma$) and 95% ($\pm 2\sigma$) confidence intervals respectively.

Table 8.1: Normalization factors for backgrounds with dedicated CRs, obtained from a simultaneous fit in all CRs and SR under the background-only hypothesis. The nominal pre-fit value is 1 for all NFs and 0 for the scaling factors a_0 and a_1 . Uncertainties shown include both statistical and systematic uncertainties.

Parameter	NF _{HF e}	NF _{HF μ}	NF _{Mat. Conv.}	NF _{Low m_{γ^*}}	a_0	a_1	NF _{$t\bar{t}W+(4j)$}	NF _{$t\bar{t}W-(4j)$}
Fit value	$0.68^{+0.23}_{-0.22}$	$0.97^{+0.17}_{-0.16}$	$0.97^{+0.31}_{-0.28}$	$0.97^{+0.23}_{-0.20}$	$0.39^{+0.11}_{-0.11}$	$0.42^{+0.25}_{-0.24}$	$1.21^{+0.18}_{-0.18}$	$1.10^{+0.26}_{-0.26}$

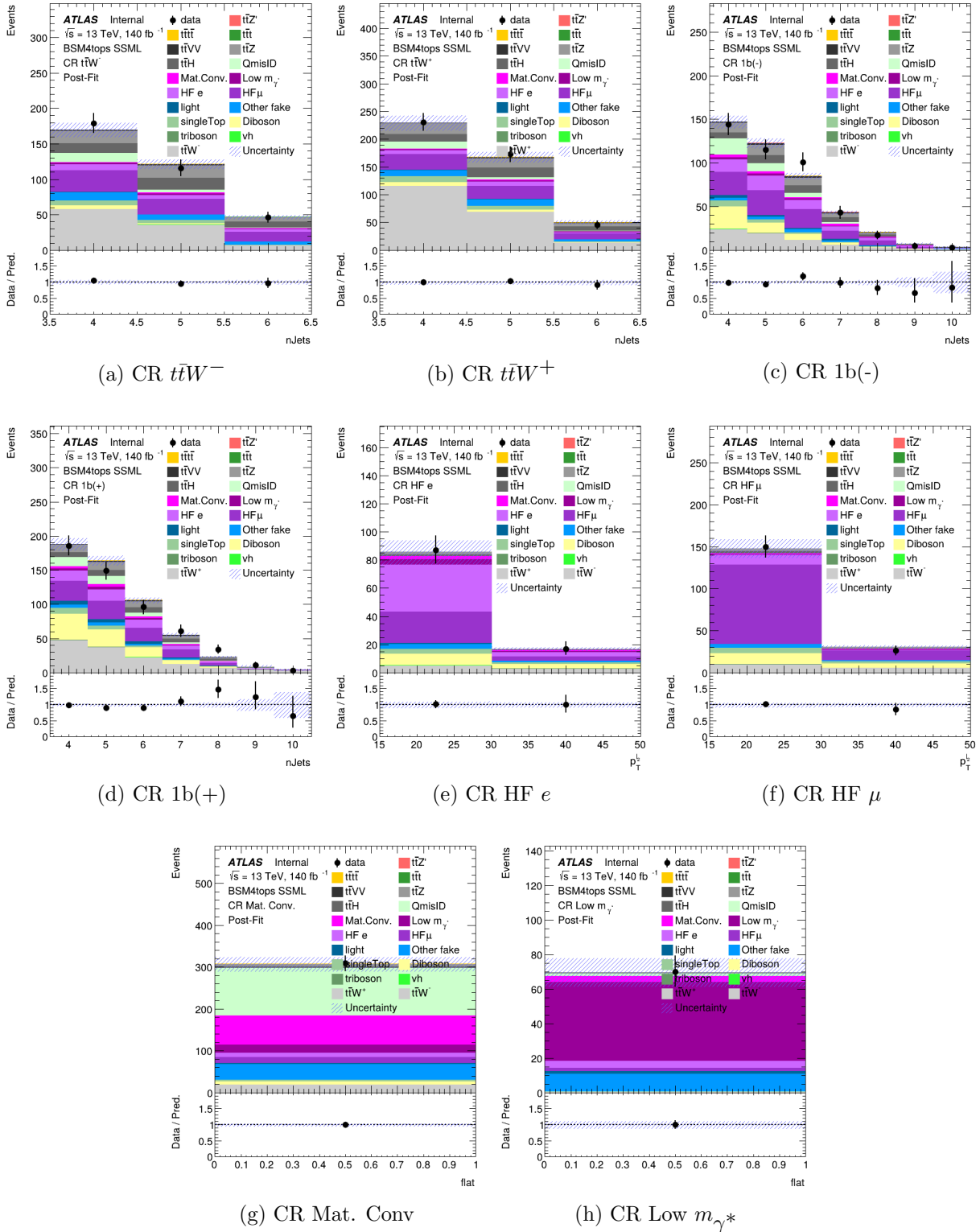


Figure 8.2: Comparison between data and post-fit prediction for the discriminant observable in each non-prompt and $t\bar{t}W$ background CR. The fit is performed simultaneously in all CRs and SR under the background-only hypothesis. The lower panel shows the ratio between data and post-fit predictions. The shaded band represents the total uncertainty on the fit.

Table 8.2: Pre-fit and post-fit background yields in the inclusive SR. The number of data events and pre-fit estimate signal yields are also shown. Background yields shown are obtained from the fit using the $t\bar{t}Z'$ signal sample with $m_{Z'} = 2$ TeV. Pre-fit yields for $t\bar{t}W$ background are set to 0 nominally prior to data-driven normalization. Total yield uncertainty differs from the quadrature sum of constituent uncertainties due to correlation and anticorrelation effects.

Process	Pre-fit	Post-fit
Background		
$t\bar{t}t\bar{t}$	42.35 ± 5.45	46.91 ± 5.19
$t\bar{t}W^+$	-	103.93 ± 15.91
$t\bar{t}W^-$	-	55.27 ± 11.14
$t\bar{t}Z$	78.02 ± 14.12	75.57 ± 11.13
$t\bar{t}H$	81.00 ± 7.10	82.90 ± 7.30
$t\bar{t}t$	3.33 ± 0.59	3.37 ± 0.60
Single-top (tq , tZq , tWZ , etc.)	13.38 ± 2.87	12.69 ± 2.86
$t\bar{t}VV/t\bar{t}VH/t\bar{t}HH$	17.07 ± 4.66	16.44 ± 4.64
Charge misidentification	40.31 ± 0.32	40.33 ± 0.32
$VV/VVV/VH$	10.01 ± 4.76	6.69 ± 2.75
Mat. Conv.	26.20 ± 0.91	25.76 ± 6.06
Low m_{γ^*}	26.14 ± 0.66	25.62 ± 4.23
HF e	21.99 ± 1.45	15.42 ± 3.70
HF μ	31.33 ± 3.47	31.53 ± 5.06
Light-flavor decays	13.47 ± 0.53	13.54 ± 0.53
Other fake & non-prompt	24.90 ± 2.26	26.00 ± 1.96
Total background	-	576.53 ± 19.86
Signal $t\bar{t}Z' \rightarrow t\bar{t}t\bar{t}$		
$m_{Z'} = 1$ TeV	52.83 ± 1.41	-
$m_{Z'} = 1.25$ TeV	52.94 ± 1.35	-
$m_{Z'} = 1.5$ TeV	53.07 ± 1.47	-
$m_{Z'} = 2$ TeV	52.49 ± 1.43	-
$m_{Z'} = 2.5$ TeV	53.07 ± 1.47	-
$m_{Z'} = 3$ TeV	52.45 ± 1.50	-
Data	604	

Table 8.3: Post-fit impact of uncertainty sources on the signal strength μ , grouped by categories. Values shown are obtained from the fit using the $t\bar{t}Z'$ signal sample with $m_{Z'} = 2$ TeV. Impact on μ is evaluated for each uncertainty category by re-fitting with the corresponding set of NPs fixed to their best-fit values. Total uncertainty differs from the quadrature sum of constituent uncertainties due to correlation between NPs in the fit.

Uncertainty source	$\Delta\mu$	
Signal modeling		
$t\bar{t}Z'$	+0.00	-0.00
Background modeling		
$t\bar{t}\bar{t}$	+0.15	-0.13
$t\bar{t}W$	+0.04	-0.03
$t\bar{t}Z$	+0.02	-0.02
$t\bar{t}H$	+0.02	-0.02
Non-prompt leptons	+0.00	-0.00
Other backgrounds	+0.02	-0.02
Instrumental		
Luminosity	+0.00	-0.00
Jet uncertainties	+0.04	-0.04
Jet flavor tagging (b -jets)	+0.04	-0.04
Jet flavor tagging (c -jets)	+0.01	-0.01
Jet flavor tagging (light-jets)	+0.02	-0.01
MC simulation sample size	+0.01	-0.01
Other experimental uncertainties	+0.01	-0.01
Total systematic uncertainty	+0.15	-0.17
Statistical		
$t\bar{t}W$ NFs and scaling factors	+0.01	-0.01
Non-prompt lepton NFs (HF, Mat. Conv., Low m_{γ^*})	+0.00	-0.00
Total statistical uncertainty	+0.25	-0.23
Total uncertainty	+0.29	-0.29

1670 Chapter 9. Summary

1671 This dissertation presents a search for BSM top-philic heavy vector resonance based on a
1672 simplified top-philic color singlet $Z'(\rightarrow t\bar{t})$ model in the top-quark pair associated production
1673 channel ($t\bar{t}Z'$). The search is performed in the same-sign dilepton and multilepton channel
1674 of the $t\bar{t}t\bar{t}$ final states, using the full Run 2 data set collected between 2015 and 2018 by the
1675 ATLAS detector at the LHC, corresponding to an integrated luminosity of 140 fb^{-1} of pp
1676 collisions at center-of-mass energy $\sqrt{s} = 13 \text{ TeV}$.

1677 New data-driven estimation methods for $t\bar{t}W$ and charge misidentification background
1678 are employed to improve background modeling and signal sensitivity compared to previous
1679 analysis [28]. No significant excess over Standard Model predictions is observed. Observed
1680 exclusion limits at 95% confidence level as a function of the Z' mass are set on the production
1681 cross section of $pp \rightarrow t\bar{t}Z'$ times the $Z' \rightarrow t\bar{t}$ branching ratio, ranging from 7.9 fb to 9.4 fb
1682 depending on the Z' mass. The analysis probes a Z' mass range from 1 TeV to 3 TeV under
1683 the assumption of a top- Z' coupling strength of $c_t = 1$ and chirality angle $\theta = \pi/4$.

1684 Further improvements in analysis strategies, including multivariate techniques for signal
1685 discrimination, are expected to increase discovery potential in future searches. Looking
1686 forward, the upcoming Run 3 data with increased luminosity at $\sqrt{s} = 13.6 \text{ TeV}$ along
1687 with prospects of the High-Luminosity LHC will significantly enhance sensitivity to BSM
1688 physics and offer more opportunities to explore top-philic resonances and other exciting new
1689 phenomena.

1690 References

- 1691 [1] J. Schwinger. *On Quantum-Electrodynamics and the Magnetic Moment of the Elec-*
1692 *tron.* Phys. Rev. 73 (4 1948), pp. 416–417 (cit. on p. 1).
- 1693 [2] R. P. Feynman. *Space-Time Approach to Quantum Electrodynamics.* Phys. Rev. 76
1694 (6 1949), pp. 769–789 (cit. on p. 1).
- 1695 [3] S. Tomonaga. *On a relativistically invariant formulation of the quantum theory of*
1696 *wave fields.* Prog. Theor. Phys. 1 (1946), pp. 27–42 (cit. on p. 1).
- 1697 [4] E. Fermi. *An attempt of a theory of beta radiation. I.* Nuclear Physics B 4 (1967).
1698 Translated from the original 1934 German article by C. P. Enz and C. H. Beck, pp. 1–
1699 27 (cit. on p. 1).
- 1700 [5] D. J. Griffiths. *Introduction to Elementary Particles.* 2nd. Weinheim: Wiley-VCH,
1701 2008. ISBN: 978-3-527-40601-2 (cit. on p. 1).
- 1702 [6] C. Yang and R. Mills. *Conservation of Isotopic Spin and Isotopic Gauge Invariance.*
1703 Phys. Rev. 96 (1 1954), pp. 191–195 (cit. on pp. 1, 10).
- 1704 [7] A. Milsted and T. J. Osborne. *Quantum Yang-Mills theory: An overview of a program.*
1705 Phys. Rev. D 98 (1 2018), p. 014505 (cit. on pp. 1, 10).

- 1706 [8] S. L. Glashow. *Partial-symmetries of weak interactions*. Nuclear Physics 22.4 (1961),
1707 pp. 579–588. ISSN: 0029-5582 (cit. on p. 1).
- 1708 [9] D. J. Gross and F. Wilczek. *Ultraviolet Behavior of Non-Abelian Gauge Theories*.
1709 Phys. Rev. Lett. 30 (26 1973), pp. 1343–1346 (cit. on p. 1).
- 1710 [10] H. D. Politzer. *Reliable Perturbative Results for Strong Interactions?* Phys. Rev. Lett.
1711 30 (26 1973), pp. 1346–1349 (cit. on p. 1).
- 1712 [11] P. Higgs. *Broken symmetries and the masses of gauge bosons*. Phys. Rev. Lett. 13 (16
1713 1964), pp. 508–509 (cit. on pp. 1, 14).
- 1714 [12] P. Higgs. *Broken symmetries, massless particles and gauge fields*. Physics Letters 12.2
1715 (1964), pp. 132–133. ISSN: 0031-9163 (cit. on pp. 1, 14).
- 1716 [13] F. Englert and R. Brout. *Broken Symmetry and the Mass of Gauge Vector Mesons*.
1717 Phys. Rev. Lett. 13 (9 1964), pp. 321–323 (cit. on pp. 1, 14).
- 1718 [14] S. Weinberg. *The making of the Standard Model*. The European Physical Journal C
1719 34.1 (May 2004), 513. ISSN: 1434-6052. arXiv: hep-ph/0401010 [hep-ph] (cit. on
1720 p. 2).
- 1721 [15] D. P. Barber et al. *Discovery of Three-Jet Events and a Test of Quantum Chromody-
1722 namics at PETRA*. Phys. Rev. Lett. 43 (12 1979), pp. 830–833 (cit. on p. 2).
- 1723 [16] G. Arnison et al. *Experimental Observation of Isolated Large Transverse Energy Elec-
1724 trons with Associated Missing Energy at $\sqrt{s} = 540 \text{ GeV}$* . Phys. Lett. B 122 (1983),
1725 pp. 103–116 (cit. on p. 2).

- 1726 [17] G. Arnison and others. *Experimental Observation of Lepton Pairs of Invariant Mass*
1727 *Around $95 \text{ GeV}/c^2$ at the CERN SPS Collider.* [Phys. Lett. B 126 \(1983\), pp. 398–410](#)
1728 (cit. on p. 2).
- 1729 [18] CDF Collaboration. *Observation of Top Quark Production in $\bar{p}p$ Collisions with the*
1730 *Collider Detector at Fermilab.* [Phys. Rev. Lett. 74 \(14 1995\), pp. 2626–2631](#) (cit. on
1731 p. 2).
- 1732 [19] DØ Collaboration. *Observation of the Top Quark.* [Phys. Rev. Lett. 74 \(14 1995\),](#)
1733 pp. 2632–2637 (cit. on p. 2).
- 1734 [20] ATLAS Collaboration. *Observation of a new particle in the search for the Standard*
1735 *Model Higgs boson with the ATLAS detector at the LHC.* [Phys. Lett. B 716 \(2012\),](#)
1736 p. 1. arXiv: 1207.7214 [[hep-ex](#)] (cit. on pp. 2, 14).
- 1737 [21] CMS Collaboration. *Observation of a new boson at a mass of 125 GeV with the CMS*
1738 *experiment at the LHC.* [Phys. Lett. B 716 \(2012\), p. 30.](#) arXiv: 1207.7235 [[hep-ex](#)]
1739 (cit. on pp. 2, 14).
- 1740 [22] S. Navas et al. *Review of particle physics.* [Phys. Rev. D 110.3 \(2024\), p. 030001](#) (cit.
1741 on pp. 2, 8).
- 1742 [23] Y. Fukuda et al. *Evidence for Oscillation of Atmospheric Neutrinos.* [Phys. Rev. Lett.](#)
1743 81 (8 1998), pp. 1562–1567 (cit. on p. 2).
- 1744 [24] M. Cristinziani and M. Mulders. *Top-quark physics at the Large Hadron Collider.*
1745 Journal of Physics G: Nuclear and Particle Physics 44.6 (2017), p. 063001. arXiv:
1746 1606.00327 [[hep-ex](#)] (cit. on pp. 2, 8).

- 1747 [25] ATLAS and CMS Collaborations. *Combination of inclusive top-quark pair production*
1748 *cross-section measurements using ATLAS and CMS data at $\sqrt{s} = 7$ and 8 TeV.* *JHEP*
1749 **07** (2023), p. 213. arXiv: [2205.13830 \[hep-ex\]](#) (cit. on p. 3).
- 1750 [26] C. Degrande, J.-M. Grard, C. Grojean, F. Maltoni, and G. Servant. *Non-resonant new*
1751 *physics in top pair production at hadron colliders.* *Journal of High Energy Physics*
1752 **2011.3** (Mar. 2011). ISSN: 1029-8479. arXiv: [1010.6304 \[hep-ph\]](#) (cit. on p. 3).
- 1753 [27] ATLAS Collaboration. *The ATLAS Experiment at the CERN Large Hadron Collider.*
1754 *JINST* **3** (2008), S08003 (cit. on pp. 3, 21, 24, 25, 27–31).
- 1755 [28] ATLAS Collaboration. *Search for top-philic heavy resonances in pp collisions at $\sqrt{s} =$*
- 1756 *13 TeV with the ATLAS detector.* *Eur. Phys. J. C* **84** (2024), p. 157. arXiv: [2304.01678 \[hep-ex\]](#) (cit. on pp. 3, 4, 18, 88).
- 1757 [29] H. P. Nilles. *Supersymmetry, Supergravity and Particle Physics.* *Phys. Rept.* **110**
1759 (1984), pp. 1–162 (cit. on p. 3).
- 1760 [30] G. R. Farrar and P. Fayet. *Phenomenology of the Production, Decay, and Detection*
1761 *of New Hadronic States Associated with Supersymmetry.* *Phys. Lett. B* **76** (1978),
1762 pp. 575–579 (cit. on p. 3).
- 1763 [31] T. Plehn and T. M. P. Tait. *Seeking sgluons.* *Journal of Physics G: Nuclear and*
1764 *Particle Physics* **36.7** (2009), p. 075001. arXiv: [0810.3919 \[hep-ph\]](#) (cit. on p. 3).
- 1765 [32] S. Calvet, B. Fuks, P. Gris, and L. Valry. *Searching for sgluons in multitop events*
1766 *at a center-of-mass energy of 8 TeV.* *Journal of High Energy Physics* **2013.4** (Apr.
1767 2013). ISSN: 1029-8479. arXiv: [1212.3360 \[hep-ph\]](#) (cit. on p. 3).

- 1768 [33] A. Pomarol and J. Serra. *Top quark compositeness: Feasibility and implications*. Phys-
1769 ical Review D 78.7 (Oct. 2008). ISSN: 1550-2368. arXiv: 0806.3247 [hep-ph] (cit. on
1770 p. 3).
- 1771 [34] K. Kumar, T. M. Tait, and R. Vega-Morales. *Manifestations of top compositeness at*
1772 *colliders*. Journal of High Energy Physics 2009.05 (May 2009), 022022. ISSN: 1029-
1773 8479. arXiv: 0901.3808 [hep-ph] (cit. on p. 3).
- 1774 [35] G. Banelli, E. Salvioni, J. Serra, T. Theil, and A. Weiler. *The present and future of*
1775 *four top operators*. Journal of High Energy Physics 2021.2 (Feb. 2021). ISSN: 1029-
1776 8479. arXiv: 2010.05915 [hep-ph] (cit. on p. 3).
- 1777 [36] R. Aoude, H. El Faham, F. Maltoni, and E. Vryonidou. *Complete SMEFT predictions*
1778 *for four top quark production at hadron colliders*. Journal of High Energy Physics
1779 2022.10 (Oct. 2022). ISSN: 1029-8479. arXiv: 2208.04962 [hep-ph] (cit. on p. 3).
- 1780 [37] C. Zhang. *Constraining qqtt operators from four-top production: a case for enhanced*
1781 *EFT sensitivity*. Chinese Physics C 42.2 (Feb. 2018), p. 023104. ISSN: 1674-1137.
1782 arXiv: 1708.05928 [hep-ph] (cit. on p. 3).
- 1783 [38] L. Darmé, B. Fuks, and F. Maltoni. *Topophilic heavy resonances in four-top final*
1784 *states and their EFT interpretation*. Journal of High Energy Physics 2021.9 (Sept.
1785 2021). ISSN: 1029-8479. arXiv: 2104.09512 [hep-ph] (cit. on pp. 3, 17).
- 1786 [39] N. Craig, F. D'Eramo, P. Draper, S. Thomas, and H. Zhang. *The Hunt for the Rest*
1787 *of the Higgs Bosons*. JHEP 06 (2015), p. 137. arXiv: 1504.04630 [hep-ph] (cit. on
1788 pp. 3, 17).

- 1789 [40] N. Craig, J. Hajer, Y.-Y. Li, T. Liu, and H. Zhang. *Heavy Higgs bosons at low $\tan \beta$:
1790 from the LHC to 100 TeV*. *Journal of High Energy Physics* 2017.1 (Jan. 2017). ISSN:
1791 1029-8479. arXiv: [1605.08744 \[hep-ph\]](#) (cit. on pp. 3, 17).
- 1792 [41] G. C. Branco et al. *Theory and phenomenology of two-Higgs-doublet models*. *Phys.
1793 Rept.* 516 (2012), pp. 1–102. arXiv: [1106.0034 \[hep-ph\]](#) (cit. on pp. 3, 17).
- 1794 [42] S. Gori, I.-W. Kim, N. R. Shah, and K. M. Zurek. *Closing the wedge: Search strategies
1795 for extended Higgs sectors with heavy flavor final states*. *Phys. Rev. D* 93 (7 2016),
1796 p. [075038](#) (cit. on pp. 3, 17).
- 1797 [43] P. S. B. Dev and A. Pilaftsis. *Maximally symmetric two Higgs doublet model with
1798 natural Standard Model alignment*. *Journal of High Energy Physics* 2014.12 (Dec.
1799 2014), p. 024. arXiv: [1408.3405 \[hep-ph\]](#) (cit. on pp. 3, 17).
- 1800 [44] ATLAS Collaboration. *Observation of four-top-quark production in the multilepton
1801 final state with the ATLAS detector*. *Eur. Phys. J. C* 83 (2023), p. 496. arXiv: [2303.
1802 15061 \[hep-ex\]](#) (cit. on pp. 3, 4, 18, 50, 61, 67, 76).
- 1803 [45] N. Greiner, K. Kong, J.-C. Park, S. C. Park, and J.-C. Winter. *Model-independent
1804 production of a topophilic resonance at the LHC*. *Journal of High Energy Physics*
1805 2015.4 (2015), p. 29. ISSN: 1029-8479. arXiv: [1410.6099 \[hep-ph\]](#) (cit. on pp. 3, 18,
1806 19).
- 1807 [46] ATLAS Collaboration. *Evidence for $t\bar{t}t\bar{t}$ production in the multilepton final state in
1808 proton–proton collisions at $\sqrt{s} = 13\text{TeV}$ with the ATLAS detector*. *Eur. Phys. J. C*
1809 80 (2020), p. 1085. arXiv: [2007.14858 \[hep-ex\]](#) (cit. on pp. 4, 67).
- 1810 [47] D. H. Perkins. *Introduction to High Energy Physics*. 4th. Cambridge, UK: Cambridge
1811 University Press, Apr. 2000. ISBN: 9780521621960 (cit. on p. 5).

- 1812 [48] C. Burgard and D. Galbraith. *Standard Model of Physics*. URL: <https://texample.net/model-physics/> (visited on 06/02/2025) (cit. on p. 6).
- 1813
- 1814 [49] H. Georgi. *Lie Algebras in Particle Physics: from Isospin to Unified Theories*. 2nd.
- 1815 CRC Press, 2000. ISBN: 9780429499210 (cit. on pp. 7, 10).
- 1816 [50] ATLAS and CMS Collaborations. *Combination of Measurements of the Top Quark*
- 1817 *Mass from Data Collected by the ATLAS and CMS Experiments at $\sqrt{s} = 7$ and 8 TeV*.
- 1818 *Phys. Rev. Lett.* **132** (2023), p. 261902. arXiv: [2402.08713 \[hep-ex\]](https://arxiv.org/abs/2402.08713) (cit. on p. 8).
- 1819 [51] H. de la Torre and T. Farooque. *Looking beyond the Standard Model with Third Gen-*
- 1820 *eration Quarks at the LHC*. *Symmetry* **14**.3 (2022), p. 444 (cit. on p. 8).
- 1821 [52] Q.-H. Cao, J.-N. Fu, Y. Liu, X.-H. Wang, and R. Zhang. *Probing Top-philic New*
- 1822 *Physics via Four-Top-Quark Production*. *Chinese Physics C* **45**.9 (2021), p. 093107.
- 1823 arXiv: [2105.03372 \[hep-ph\]](https://arxiv.org/abs/2105.03372) (cit. on p. 8).
- 1824 [53] H. Beauchesne et al. *A case study about BSM vector resonances with direct couplings*
- 1825 *to the third quark generation*. *European Physical Journal C* **80**.5 (2020), p. 485. arXiv:
- 1826 [1908.11619 \[hep-ph\]](https://arxiv.org/abs/1908.11619) (cit. on p. 8).
- 1827 [54] F. Maltoni, D. Pagani, and S. Tentori. *Top-quark pair production as a probe of light*
- 1828 *top-philic scalars and anomalous Higgs interactions*. *Journal of High Energy Physics*
- 1829 **2024**.9 (Sept. 2024), p. 098. arXiv: [2406.06694 \[hep-ph\]](https://arxiv.org/abs/2406.06694) (cit. on p. 8).
- 1830 [55] CMS Collaboration. *Search for $t\bar{t}H$ production in the $H \rightarrow b\bar{b}$ decay channel with*
- 1831 *leptonic $t\bar{t}$ decays in proton-proton collisions at $\sqrt{s} = 13$ TeV*. *JHEP* **03** (2019),
- 1832 p. 026. arXiv: [1804.03682 \[hep-ex\]](https://arxiv.org/abs/1804.03682) (cit. on p. 8).

- 1833 [56] Y. Grossman and Y. Nir. *The Standard Model: From Fundamental Symmetries to Ex-*
1834 *perimental Tests*. See Chapter 8.2. Cambridge University Press, 2023. ISBN: 9781009320378
1835 (cit. on p. 9).
- 1836 [57] M. E. Peskin and D. V. Schroeder. *An Introduction to Quantum Field Theory*. 1st.
1837 Reading, MA, USA: AddisonWesley, 1995. ISBN: 978-0-201-50397-5 (cit. on p. 9).
- 1838 [58] D. J. Gross. *The role of symmetry in fundamental physics*. Proceedings of the National
1839 Academy of Sciences of the United States of America 93.25 (Dec. 1996), pp. 14256–
1840 14259 (cit. on p. 9).
- 1841 [59] M. Bañados and I. Reyes. *A short review on Noethers theorems, gauge symmetries*
1842 *and boundary terms*. International Journal of Modern Physics D 25.10 (Aug. 2016),
1843 p. 1630021. ISSN: 1793-6594. arXiv: 1601.03616 [hep-th] (cit. on p. 9).
- 1844 [60] A. Pich. *The Standard Model of electroweak interactions. 2004 European School of*
1845 *High-Energy Physics*. Feb. 2005, pp. 1–48. arXiv: hep-ph/0502010 [hep-ex] (cit. on
1846 pp. 11–13).
- 1847 [61] P. Dev and A. Pilaftsis. *High-temperature electroweak symmetry non-restoration from*
1848 *new fermions and implications for baryogenesis*. Journal of High Energy Physics
1849 2020.9 (Sept. 2020), p. 012. arXiv: 2002.05174 [hep-ph] (cit. on p. 13).
- 1850 [62] J. Riebesell. *Higgs Potential*. URL: <https://tikz.net/higgs-potential/> (visited on
1851 07/07/2025) (cit. on p. 15).
- 1852 [63] J. Goldstone, A. Salam, and S. Weinberg. *Broken Symmetries*. Phys. Rev. 127 (3
1853 1962), pp. 965–970 (cit. on p. 15).
- 1854 [64] J. Ellis. *Higgs Physics. 2013 European School of High-Energy Physics*. 2015, pp. 117–
1855 168. arXiv: 1312.5672 [hep-ph] (cit. on pp. 15, 16).

- 1856 [65] CDF Collaboration. *Search for New Physics in High-Mass Electron-Positron Events*
1857 *in $p\bar{p}$ Collisions at $\sqrt{s} = 1.96$ TeV.* Phys. Rev. Lett. 99 (17 2007), p. 171802. arXiv:
1858 0707.2524 [hep-ex] (cit. on p. 17).
- 1859 [66] M. Battaglia and G. Servant. *Four-top production and $t\bar{t}$ +missing energy events at*
1860 *multi TeV e^+e^- colliders.* Nuovo Cim. C 033N2 (2010), pp. 203–208. arXiv: 1005.4632
1861 [hep-ex] (cit. on p. 17).
- 1862 [67] N. Arkani-Hamed, A. G. Cohen, and H. Georgi. *Electroweak symmetry breaking from*
1863 *dimensional deconstruction.* Physics Letters B 513.1-2 (July 2001), pp. 232–240. arXiv:
1864 hep-ph/0105239 [hep-ph] (cit. on p. 17).
- 1865 [68] T. Han, H. E. Logan, B. McElrath, and L.-T. Wang. *Phenomenology of the little Higgs*
1866 *model.* Phys. Rev. D 67 (9 2003), p. 095004. arXiv: hep-ph/0301040 [hep-ph] (cit. on
1867 p. 17).
- 1868 [69] P. Langacker and M. Plümacher. *Flavor changing effects in theories with a heavy Z'*
1869 *boson with family nonuniversal couplings.* Phys. Rev. D 62 (1 2000), p. 013006. arXiv:
1870 hep-ph/0001204 [hep-ph] (cit. on p. 17).
- 1871 [70] P. Langacker. *The Physics of Heavy Z' Gauge Bosons.* Rev. Mod. Phys. 81 (2009),
1872 pp. 1199–1228. arXiv: 0801.1345 [hep-ph] (cit. on p. 17).
- 1873 [71] J. H. Kim, K. Kong, S. J. Lee, and G. Mohlabeng. *Probing TeV scale top-philic*
1874 *resonances with boosted top-tagging at the high luminosity LHC.* Phys. Rev. D 94 (3
1875 2016), p. 035023. arXiv: 1604.07421 [hep-ph] (cit. on pp. 17, 18, 84).
- 1876 [72] P. J. Fox, I. Low, and Y. Zhang. *Top-philic Z' forces at the LHC.* Journal of High
1877 Energy Physics 2018.3 (Mar. 2018). ISSN: 1029-8479. arXiv: 1801.03505 [hep-ph]
1878 (cit. on p. 17).

- 1879 [73] CMS Collaboration. *Observation of four top quark production in proton-proton col-*
1880 *lisions at $\sqrt{s} = 13\text{TeV}$* . Physics Letters B 847 (2023), p. 138290. arXiv: 2305.13439
1881 [hep-ex] (cit. on p. 18).
- 1882 [74] G. Ferretti and D. Karateev. *Fermionic UV completions of composite Higgs models*.
1883 Journal of High Energy Physics 2014.3 (Mar. 2014). ISSN: 1029-8479 (cit. on p. 17).
- 1884 [75] L. Vecchi. *A dangerous irrelevant UV-completion of the composite Higgs*. JHEP 02
1885 (2017), p. 094. arXiv: 1506.00623 [hep-ph] (cit. on p. 17).
- 1886 [76] P. Sabatini. *Evidence for four-top-quarks production with the ATLAS detector at the*
1887 *Large Hadron Collider*. Tech. rep. Geneva: CERN, 2021. URL: <https://cds.cern.ch/record/2784150> (cit. on p. 20).
- 1889 [77] L. Evans and P. Bryant. *LHC Machine*. JINST 3 (2008), S08001 (cit. on p. 21).
- 1890 [78] CMS Collaboration. *The CMS Experiment at the CERN LHC*. JINST 3 (2008),
1891 S08004 (cit. on p. 21).
- 1892 [79] The ALICE Collaboration. *The ALICE experiment at the CERN LHC*. JINST 3
1893 (2008), S08002 (cit. on p. 21).
- 1894 [80] The LHCb Collaboration. *The LHCb Detector at the LHC*. JINST 3 (2008), S08005
1895 (cit. on p. 21).
- 1896 [81] E. e. a. Gschwendtner. *AWAKE, The Advanced Proton Driven Plasma Wakefield*
1897 *Acceleration Experiment at CERN*. Nuclear Instruments and Methods in Physics Re-
1898 search Section A 829 (2016), pp. 76–82. arXiv: 1512.05498 [physics.acc-ph] (cit. on
1899 p. 22).

- 1900 [82] J. L. Feng, I. Galon, F. Kling, and S. Trojanowski. *ForwArd Search ExpeRiment at*
1901 *the LHC*. Phys. Rev. D 97 (3 2018), p. 035001. arXiv: 1708.09389 [hep-ph] (cit. on
1902 p. 22).
- 1903 [83] The KATRIN collaboration. *The design, construction, and commissioning of the KA-*
1904 *TRIN experiment*. Journal of Instrumentation 16.08 (2021), T08015. arXiv: 2103.
1905 04755 [physics.ins-det] (cit. on p. 22).
- 1906 [84] E. Lopienska. *The CERN accelerator complex, layout in 2022*. General Photo. 2022.
1907 URL: <https://cds.cern.ch/record/2800984> (visited on 07/08/2025) (cit. on p. 22).
- 1908 [85] High Luminosity LHC Project Organization. *The HL-LHC project*. 2025. URL: <https://hilumilhc.web.cern.ch/content/hl-lhc-project> (visited on 06/11/2025) (cit. on
1909 p. 23).
- 1910 [86] ATLAS Collaboration. *Performance of the ATLAS detector using first collision data*.
1911 JHEP 09 (2010), p. 056. arXiv: 1005.5254 [hep-ex] (cit. on p. 23).
- 1912 [87] ATLAS Collaboration. *Luminosity determination in pp collisions at $\sqrt{s} = 13 \text{ TeV}$*
1913 *using the ATLAS detector at the LHC*. Eur. Phys. J. C 83 (2023), p. 982. arXiv:
1914 2212.09379 [hep-ex] (cit. on pp. 24, 50, 69).
- 1915 [88] J. M. Butterworth, G. Dissertori, and G. P. Salam. *Hard Processes in Proton-Proton*
1916 *Collisions at the Large Hadron Collider*. Annu. Rev. Nucl. Part. Sci. 62 (2012),
1917 pp. 387–405. arXiv: 1202.0583 [hep-ex] (cit. on p. 24).
- 1918 [89] J. Campbell, J. Huston, and W. J. Stirling. *Hard interactions of quarks and gluons:*
1919 *a primer for LHC physics*. Reports on Progress in Physics 70.1 (2006), p. 89. arXiv:
1920 hep-ph/0611148 [hep-ex] (cit. on p. 24).
- 1921

- 1922 [90] ATLAS Collaboration. *Standard Model Summary Plots October 2023*. ATL-PHYS-
1923 PUB-2023-039. 2023. URL: <https://cds.cern.ch/record/2882448> (cit. on p. 25).
- 1924 [91] J. Pequenao and P. Schaffner. *How ATLAS detects particles: diagram of particle*
1925 *paths in the detector*. 2013. URL: <https://cds.cern.ch/record/1505342> (visited on
1926 07/08/2025) (cit. on p. 26).
- 1927 [92] J. Pequenao. *Computer generated image of the ATLAS inner detector*. 2008. URL:
1928 <https://cds.cern.ch/record/1095926> (visited on 07/08/2025) (cit. on p. 27).
- 1929 [93] J. Pequenao. *Computer Generated image of the ATLAS calorimeter*. 2008. URL: <https://cds.cern.ch/record/1095927> (visited on 07/08/2025) (cit. on p. 29).
- 1931 [94] ATLAS Collaboration. *Operation of the ATLAS trigger system in Run 2*. **JINST** 15
1932 (2020), P10004. arXiv: [2007.12539 \[physics.ins-det\]](https://arxiv.org/abs/2007.12539) (cit. on p. 32).
- 1933 [95] ATLAS Collaboration. *Performance of the ATLAS track reconstruction algorithms*
1934 *in dense environments in LHC Run 2*. **Eur. Phys. J. C** 77 (2017), p. 673. arXiv:
1935 [1704.07983 \[hep-ex\]](https://arxiv.org/abs/1704.07983) (cit. on p. 33).
- 1936 [96] T. Cornelissen et al. *Concepts, design and implementation of the ATLAS New Track-*
1937 *ing (NEWT)*. Tech. rep. Geneva: CERN, 2007. URL: <https://cds.cern.ch/record/1020106> (cit. on p. 33).
- 1939 [97] A. Salzburger. *Optimisation of the ATLAS Track Reconstruction Software for Run-2*.
1940 *Journal of Physics: Conference Series* 664.7 (2015), p. 072042 (cit. on p. 33).
- 1941 [98] R. Frühwirth. *Application of Kalman filtering to track and vertex fitting*. **Nucl. In-**
1942 *strum. Methods Phys. Res. A* 262.2 (1987), pp. 444–450. ISSN: 0168-9002 (cit. on
1943 p. 33).

- 1944 [99] T. Cornelissen et al. *The global χ^2 track fitter in ATLAS*. Journal of Physics: Con-
1945 ference Series 119.3 (2008), p. 032013 (cit. on p. 33).
- 1946 [100] ATLAS Collaboration. *Improved electron reconstruction in ATLAS using the Gaus-
1947 sian Sum Filter-based model for bremsstrahlung*. ATLAS-CONF-2012-047. 2012. URL:
1948 <https://cds.cern.ch/record/1449796> (cit. on p. 33).
- 1949 [101] D. Wicke. *A new algorithm for solving tracking ambiguities*. Tech. rep. Oct. 1998.
1950 URL: <https://cds.cern.ch/record/2625731> (cit. on p. 34).
- 1951 [102] ATLAS Collaboration. *Reconstruction of primary vertices at the ATLAS experiment
1952 in Run 1 proton–proton collisions at the LHC*. Eur. Phys. J. C 77 (2017), p. 332.
1953 arXiv: [1611.10235 \[physics.ins-det\]](https://arxiv.org/abs/1611.10235) (cit. on p. 34).
- 1954 [103] W. Waltenberger, R. Frühwirth, and P. Vanlaer. *Adaptive vertex fitting*. Journal of
1955 Physics G: Nuclear and Particle Physics 34.12 (2007), N343 (cit. on p. 34).
- 1956 [104] ATLAS Collaboration. *Secondary vertex finding for jet flavour identification with the
1957 ATLAS detector*. ATL-PHYS-PUB-2017-011. 2017. URL: <https://cds.cern.ch/record/2270366> (cit. on p. 34).
- 1959 [105] ATLAS Collaboration. *Performance of pile-up mitigation techniques for jets in pp
1960 collisions at $\sqrt{s} = 8 \text{ TeV}$ using the ATLAS detector*. Eur. Phys. J. C 76 (2016),
1961 p. 581. arXiv: [1510.03823 \[hep-ex\]](https://arxiv.org/abs/1510.03823) (cit. on pp. 35, 38).
- 1962 [106] ATLAS Collaboration. *Topological cell clustering in the ATLAS calorimeters and its
1963 performance in LHC Run 1*. Eur. Phys. J. C 77 (2017), p. 490. arXiv: [1603.02934](https://arxiv.org/abs/1603.02934)
1964 [hep-ex] (cit. on pp. 35, 36).

- 1965 [107] ATLAS Collaboration. *Jet reconstruction and performance using particle flow with*
1966 *the ATLAS Detector.* *Eur. Phys. J. C* **77** (2017), p. 466. arXiv: [1703.10485 \[hep-ex\]](#)
1967 (cit. on p. 37).
- 1968 [108] M. Cacciari, G. P. Salam, and G. Soyez. *The anti- k_t jet clustering algorithm.* *JHEP*
1969 **04** (2008), p. 063. arXiv: [0802.1189 \[hep-ph\]](#) (cit. on p. 37).
- 1970 [109] ATLAS Collaboration. *Jet energy scale and resolution measured in proton–proton*
1971 *collisions at $\sqrt{s} = 13\text{ TeV}$ with the ATLAS detector.* *Eur. Phys. J. C* **81** (2021),
1972 p. 689. arXiv: [2007.02645 \[hep-ex\]](#) (cit. on pp. 38, 71–73).
- 1973 [110] ATLAS Collaboration. *Jet energy scale measurements and their systematic uncertainties in proton–proton collisions at $\sqrt{s} = 13\text{ TeV}$ with the ATLAS detector.* *Phys. Rev.*
1974 **D 96** (2017), p. 072002. arXiv: [1703.09665 \[hep-ex\]](#) (cit. on pp. 38, 71).
- 1976 [111] ATLAS Collaboration. *Transforming jet flavour tagging at ATLAS.* Tech. rep. Sub-
1977 mitted to: Nature Communications. Geneva: CERN, 2025. arXiv: [2505.19689](#) (cit. on
1978 pp. 39–41).
- 1979 [112] A. Vaswani et al. *Attention Is All You Need.* 2023. arXiv: [1706.03762 \[cs.CL\]](#) (cit. on
1980 p. 39).
- 1981 [113] ATLAS Collaboration. *Measurements of b -jet tagging efficiency with the ATLAS de-*
1982 *tector using $t\bar{t}$ events at $\sqrt{s} = 13\text{ TeV}.$* *JHEP* **08** (2018), p. 089. arXiv: [1805.01845](#)
1983 [[hep-ex](#)] (cit. on pp. 41, 73).
- 1984 [114] ATLAS Collaboration. *Electron reconstruction and identification in the ATLAS ex-*
1985 *periment using the 2015 and 2016 LHC proton–proton collision data at $\sqrt{s} = 13\text{ TeV}.$*
1986 *Eur. Phys. J. C* **79** (2019), p. 639. arXiv: [1902.04655 \[physics.ins-det\]](#) (cit. on
1987 pp. 42–44).

- 1988 [115] ATLAS Collaboration. *Electron Identification with a Convolutional Neural Network*
1989 *in the ATLAS Experiment*. ATL-PHYS-PUB-2023-001. 2023. URL: <https://cds.cern.ch/record/2850666>.
- 1990
- 1991 [116] ATLAS Collaboration. *Muon reconstruction and identification efficiency in ATLAS*
1992 *using the full Run 2 pp collision data set at $\sqrt{s} = 13 \text{ TeV}$* . *Eur. Phys. J. C* **81** (2021),
1993 p. 578. arXiv: [2012.00578 \[hep-ex\]](https://arxiv.org/abs/2012.00578) (cit. on pp. 45, 46).
- 1994 [117] ATLAS Collaboration. *Muon reconstruction performance of the ATLAS detector in*
1995 *proton–proton collision data at $\sqrt{s} = 13 \text{ TeV}$* . *Eur. Phys. J. C* **76** (2016), p. 292. arXiv:
1996 [1603.05598 \[hep-ex\]](https://arxiv.org/abs/1603.05598) (cit. on p. 46).
- 1997 [118] ATLAS Collaboration. *Performance of missing transverse momentum reconstruction*
1998 *with the ATLAS detector using proton–proton collisions at $\sqrt{s} = 13 \text{ TeV}$* . *Eur. Phys.*
1999 *J. C* **78** (2018), p. 903. arXiv: [1802.08168 \[hep-ex\]](https://arxiv.org/abs/1802.08168) (cit. on pp. 47, 73).
- 2000 [119] ATLAS Collaboration. *E_T^{miss} performance in the ATLAS detector using 2015–2016*
2001 *LHC pp collisions*. ATLAS-CONF-2018-023. 2018. URL: <https://cds.cern.ch/record/2625233> (cit. on p. 48).
- 2002
- 2003 [120] J. Alwall et al. *The automated computation of tree-level and next-to-leading order*
2004 *differential cross sections, and their matching to parton shower simulations*. *JHEP* **07**
2005 (2014), p. 079. arXiv: [1405.0301 \[hep-ph\]](https://arxiv.org/abs/1405.0301) (cit. on pp. 51, 53, 54).
- 2006 [121] NNPDF Collaboration, R. D. Ball, et al. *Parton distributions for the LHC run II*.
2007 *JHEP* **04** (2015), p. 040. arXiv: [1410.8849 \[hep-ph\]](https://arxiv.org/abs/1410.8849) (cit. on pp. 51, 53, 54).
- 2008 [122] T. Sjöstrand et al. *An introduction to PYTHIA 8.2*. *Comput. Phys. Commun.* **191**
2009 (2015), p. 159. arXiv: [1410.3012 \[hep-ph\]](https://arxiv.org/abs/1410.3012) (cit. on pp. 51, 53, 54).

- 2010 [123] ATLAS Collaboration. *ATLAS Pythia 8 tunes to 7 TeV data*. ATL-PHYS-PUB-2014-
2011 021. 2014. URL: <https://cds.cern.ch/record/1966419> (cit. on pp. 53, 54).
- 2012 [124] S. Frixione, E. Laenen, P. Motylinski, and B. R. Webber. *Angular correlations of*
2013 *lepton pairs from vector boson and top quark decays in Monte Carlo simulations*.
2014 JHEP 04 (2007), p. 081. arXiv: [hep-ph/0702198](https://arxiv.org/abs/hep-ph/0702198) (cit. on p. 53).
- 2015 [125] P. Artoisenet, R. Frederix, O. Mattelaer, and R. Rietkerk. *Automatic spin-entangled*
2016 *decays of heavy resonances in Monte Carlo simulations*. JHEP 03 (2013), p. 015.
2017 arXiv: [1212.3460 \[hep-ph\]](https://arxiv.org/abs/1212.3460) (cit. on p. 53).
- 2018 [126] D. J. Lange. *The EvtGen particle decay simulation package*. Nucl. Instrum. Meth. A
2019 462 (2001), p. 152 (cit. on p. 53).
- 2020 [127] R. Frederix, D. Pagani, and M. Zaro. *Large NLO corrections in $t\bar{t}W^\pm$ and $t\bar{t}t\bar{t}$*
2021 *hadroproduction from supposedly subleading EW contributions*. JHEP 02 (2018), p. 031.
2022 arXiv: [1711.02116 \[hep-ph\]](https://arxiv.org/abs/1711.02116) (cit. on pp. 53, 75).
- 2023 [128] E. Bothmann et al. *Event generation with Sherpa 2.2*. SciPost Phys. 7.3 (2019), p. 034.
2024 arXiv: [1905.09127 \[hep-ph\]](https://arxiv.org/abs/1905.09127) (cit. on pp. 53, 54).
- 2025 [129] S. Schumann and F. Krauss. *A parton shower algorithm based on Catani–Seymour*
2026 *dipole factorisation*. JHEP 03 (2008), p. 038. arXiv: [0709.1027 \[hep-ph\]](https://arxiv.org/abs/0709.1027) (cit. on
2027 p. 53).
- 2028 [130] S. Höche, F. Krauss, M. Schönher, and F. Siegert. *A critical appraisal of NLO+PS*
2029 *matching methods*. JHEP 09 (2012), p. 049. arXiv: [1111.1220 \[hep-ph\]](https://arxiv.org/abs/1111.1220) (cit. on p. 53).
- 2030 [131] S. Höche, F. Krauss, M. Schönher, and F. Siegert. *QCD matrix elements + parton*
2031 *showers. The NLO case*. JHEP 04 (2013), p. 027. arXiv: [1207.5030 \[hep-ph\]](https://arxiv.org/abs/1207.5030) (cit. on
2032 p. 53).

- 2033 [132] S. Catani, F. Krauss, B. R. Webber, and R. Kuhn. *QCD Matrix Elements + Parton*
 2034 *Showers*. JHEP 11 (2001), p. 063. arXiv: [hep-ph/0109231](#) (cit. on p. 53).
- 2035 [133] S. Höche, F. Krauss, S. Schumann, and F. Siegert. *QCD matrix elements and truncated*
 2036 *showers*. JHEP 05 (2009), p. 053. arXiv: [0903.1219 \[hep-ph\]](#) (cit. on p. 53).
- 2037 [134] F. Caccioli, P. Maierhöfer, and S. Pozzorini. *Scattering Amplitudes with Open Loops*.
 2038 Phys. Rev. Lett. 108 (2012), p. 111601. arXiv: [1111.5206 \[hep-ph\]](#) (cit. on p. 53).
- 2039 [135] A. Denner, S. Dittmaier, and L. Hofer. *COLLIER: A fortran-based complex one-loop*
 2040 *library in extended regularizations*. Comput. Phys. Commun. 212 (2017), pp. 220–238.
 2041 arXiv: [1604.06792 \[hep-ph\]](#) (cit. on p. 53).
- 2042 [136] F. Buccioni et al. *OpenLoops 2*. Eur. Phys. J. C 79.10 (2019), p. 866. arXiv: [1907.13071](#)
 2043 [[hep-ph](#)] (cit. on p. 53).
- 2044 [137] ATLAS Collaboration. *ATLAS data quality operations and performance for 2015–*
 2045 *2018 data-taking*. JINST 15 (2020), P04003. arXiv: [1911.04632 \[physics.ins-det\]](#)
 2046 (cit. on p. 55).
- 2047 [138] ATLAS Collaboration. *Analysis of $t\bar{t}H$ and $t\bar{t}W$ production in multilepton final states*
 2048 *with the ATLAS detector*. ATLAS-CONF-2019-045. 2019. URL: <https://cds.cern.ch/record/2693930> (cit. on pp. 61, 64, 77).
- 2049
 2050 [139] ATLAS Collaboration. *Measurement of the total and differential cross-sections of $t\bar{t}W$*
 2051 *production in pp collisions at $\sqrt{s} = 13 \text{ TeV}$ with the ATLAS detector*. JHEP 05 (2024),
 2052 p. 131. arXiv: [2401.05299 \[hep-ex\]](#) (cit. on p. 61).
- 2053 [140] ATLAS Collaboration. *Search for new phenomena in events with same-charge leptons*
 2054 *and b -jets in pp collisions at $\sqrt{s} = 13 \text{ TeV}$ with the ATLAS detector*. JHEP 12 (2018),
 2055 p. 039. arXiv: [1807.11883 \[hep-ex\]](#) (cit. on p. 65).

- 2056 [141] ATLAS Collaboration. *Search for R-parity-violating supersymmetry in a final state*
2057 *containing leptons and many jets with the ATLAS experiment using $\sqrt{s} = 13\text{ TeV}$*
2058 *proton–proton collision data.* *Eur. Phys. J. C* **81** (2021), p. 1023. arXiv: [2106.09609](https://arxiv.org/abs/2106.09609)
2059 [[hep-ex](#)] (cit. on p. 67).
- 2060 [142] E. Gerwick, T. Plehn, S. Schumann, and P. Schichtel. *Scaling Patterns for QCD Jets.*
2061 *JHEP* **10** (2012), p. 162. arXiv: [1208.3676](https://arxiv.org/abs/1208.3676) [[hep-ph](#)] (cit. on p. 67).
- 2062 [143] G. Avoni et al. *The new LUCID-2 detector for luminosity measurement and moni-*
2063 *toring in ATLAS.* *JINST* **13.07** (2018), P07017 (cit. on p. 69).
- 2064 [144] ATLAS Collaboration. *Tagging and suppression of pileup jets.* ATL-PHYS-PUB-2014-
2065 001. 2014. URL: <https://cds.cern.ch/record/1643929> (cit. on pp. 71, 73).
- 2066 [145] ATLAS Collaboration. *Measurements of inclusive and differential fiducial cross-sections*
2067 *of $t\bar{t}$ production with additional heavy-flavour jets in proton–proton collisions at $\sqrt{s} =$*
2068 *13 TeV with the ATLAS detector.* *JHEP* **04** (2019), p. 046. arXiv: [1811.12113](https://arxiv.org/abs/1811.12113) [[hep-ex](#)]
2069 (cit. on p. 75).
- 2070 [146] D. de Florian et al. *Handbook of LHC Higgs Cross Sections: 4. Deciphering the Nature*
2071 *of the Higgs Sector.* CERN Yellow Rep. Monogr. **2** (2017), pp. 1–869. arXiv: [1610.07922](https://arxiv.org/abs/1610.07922) [[hep-ph](#)] (cit. on p. 75).
- 2073 [147] ATLAS Collaboration. *Measurement of the production cross-section of a single top*
2074 *quark in association with a Z boson in proton–proton collisions at 13 TeV with the*
2075 *ATLAS detector.* ATLAS-CONF-2017-052. 2017. URL: <https://cds.cern.ch/record/2273868> (cit. on p. 75).

- 2077 [148] F. Demartin, B. Maier, F. Maltoni, K. Mawatari, and M. Zaro. *tWH associated*
2078 *production at the LHC*. EPJC 77.1 (2017). arXiv: 1607.05862 [hep-ph]. URL: <https://doi.org/10.1140/epjc/s10052-017-4601-7> (cit. on p. 75).
- 2079
2080 [149] ATLAS Collaboration. *Measurement of $W^\pm Z$ production cross sections and gauge*
2081 *boson polarisation in pp collisions at $\sqrt{s} = 13$ TeV with the ATLAS detector*. Eur.
2082 Phys. J. C 79 (2019), p. 535. arXiv: 1902.05759 [hep-ex] (cit. on p. 75).
- 2083 [150] G. Cowan, K. Cranmer, E. Gross, and O. Vitells. *Asymptotic formulae for likelihood-*
2084 *based tests of new physics*. The European Physical Journal C 71.2 (Feb. 2011). ISSN:
2085 1434-6052. arXiv: 1007.1727 [physics.data-an]. URL: <http://dx.doi.org/10.1140/epjc/s10052-011-1554-0> (cit. on p. 79).
- 2086
2087 [151] J. Neyman and E. S. Pearson. *IX. On the problem of the most efficient tests of*
2088 *statistical hypotheses*. Philosophical Transactions of the Royal Society of London.
2089 Series A, Containing Papers of a Mathematical or Physical Character 231.694-706
2090 (1933), pp. 289–337 (cit. on p. 79).
- 2091 [152] S. S. Wilks. *The large-sample distribution of the likelihood ratio for testing composite*
2092 *hypotheses*. Annals of Mathematical Statistics 9.1 (1938), pp. 60–62 (cit. on p. 80).
- 2093 [153] T. Junk. *Confidence level computation for combining searches with small statistics*.
2094 Nuclear Instruments and Methods in Physics Research Section A: Accelerators, Spec-
2095 *rometers, Detectors and Associated Equipment* 434.23 (Sept. 1999), 435443. ISSN:
2096 0168-9002. arXiv: hep-ex/9902006 [hep-ex] (cit. on p. 81).
- 2097 [154] A. L. Read. *Modified frequentist analysis of search results: The CLs method*. Tech.
2098 rep. CERN-OPEN-2000-205. Presented at Workshop on Confidence Limits, Geneva,
2099 Switzerland. CERN, 2000. URL: <https://cds.cern.ch/record/451614> (cit. on p. 81).